Study of Particle Motion In Flows Characteristic To Low-NO_x Pulverised Fuel Burners

by

Enock Masanja

Keywords: Particle ropes, Two-phase, Low-NO_x, PIV, LDA

This thesis is submitted to the
Chemical Engineering Department of Edinburgh University
in fulfillment of the requirements
for the degree of Doctor of Philosophy

Reasearch work done under the supervision of
Dr. Donald H. Glass and Prof. Clive A. Greated

Chemical Engineering Department , Edinburgh University,
Edinburgh, Scotland

1995

ABSTRACT

Study of Particle Motion In Flows Characteristic To Low-NO_x Pulverised Fuel Burners

by

Enock Masanja,

Research Supervisors: Dr. Donald H. Glass and

Prof. Clive A. Greated

There is no dispute that combustion by-products like sulphur dioxide, SO_2 and nitrogen oxides, NO_x, can cause environmental damage.

New, tougher legislation on gas emission has started to push fundamental research work (like this project) on understanding particle/fluid dynamics in combustion and related systems on the fore front. The knowledge gained will not only offer immediate help in the control and abatement of gas emission, but also the data obtained will complement the available empirical (industrial) knowledge of roping behaviour which will be valuable in developing new numerical models and/or verifying existing ones.

A test facility delivering up to 40 m/s in a 4 inch glass test section was designed, fabricated, assembled and tested. This includes swirl generators for generating swirl of 0.2 to 1.35 theoretical swirl numbers. The facility also includes a particle feed section, cyclone separator for recovering the particles and a dual pulsed Nd:YaG laser, related optics and other equipment for use in future Particle Image Velocimetry (PIV) research.

LDA and Pitot-static measurements verified that the test section was capable of delivering the planned/design velocity measurement range of 0-40 m/s. PIV experiments were done for particle jet density of 95 kg/m_{-3} to 198 kg/m_{-3} and the results obtained on particle jet dispersion were in good agreement with previous work showing that the center line velocity showed less fluctuation and that jets that are less dense disperse more than the more dense ones.

Acknowledgements

I am indebted to the following:

1. The University of Dar Es Salaam, my employer for grating me study leave.
2. The Swiss Development Agency, SDC, for the generous scholarship, and The German Academic Exchange Service for administering part of this scholarship.
3. The Department of Chemical and Process Engineering, and the Faculty of Engineering for logistical support, particularly in arranging for study leave extension and travel arrangements for my family.
4. My supervisors, Dr. Donald H. Glass and Dr. Clive A. Greated for support and guidance.
5. Dr. William J. Easson initially as part of the supervisory team for support and guidance.
6. The Chemical Engineering Workshop staff for fabricating and assembling the rig and for many other chores.
7. Ms Denise McCluskey, for assisting me to learn LDA and PIV alignment.
8. Lastly and not the least, my wife, Helene: for everything, and my daughters, Martha and Elizabeth, who gave me the resources to replenish my strength.

Dedication

To memories of my beloved mother....

Table of Contents

List of Tables

List of Figures

List of Symbols

A	Flow (cross) section area.
C	Friction factor.
C_D	Drag coefficient.
$C_{1\varepsilon}, C_{2\varepsilon}$	Empirical constants in the $k-\varepsilon$ model.
d, D	Diameter.
D_h	Hydraulic diameter.
F_r	Froude number.
F_j	Interaction forces e.g. between two phases.
f	Frequency.
f_s	Sound frequency.
G_x	Swirl vane linear momentum.
G_w	Swirl vane angular momentum.
g	Gravitational acceleration.
h	Column of manometer liquid.
h_{f1}	Friction loss for flow though a swirl vanes at 0° angle.
h_{f2}	Friction loss for flow though a swirl vanes at α° angle.
i	represents a group of particles of diameter d_i $(i = 1 \ldots n)$.
k	Kinetic energy of the turbulent motion per unit mass.
K	Universal constant (Kármán constant) of turbulent wall effects.
$\overline{k}$	Mean kinetic energy of the turbulent motion per unit mass.
l	Length.
l_m	Prandtl mixing length.
m	Particle-to-air mass flux ratio, ratio of the refractive indences of the scatterer and the surrounding medium.
$\dot{m}$	Mass flow rate.
p	Pressure, fluctuating static pressure.
$\overline{P}$	Mean static pressure.
Q	Volumetric flow rate.
Q_D	Design volumetric flow rate.
r_e	Radius of exit pipe.
R	Radius of annulus.
R_h	Radius of hub holding swirl vanes.
Re	Reynolds number.
r_t	Radius of circle to which the inlet centre is tangential.
S	Theoretical swirl number.
St	Stokes' number.
t^*	Particle relaxation time.
t	Time.
u	Fluctuating velocity.
$\overline{U}$	Mean velocity.

U_i, u	Instantaneous velocity component in x direction.
U_j, v	Fluctuating velocity in y (radial) direction.
$U_{average}$	Average velocity in flow area.
U_{max}	Maximum velocity in flow area.
u_t	Friction velocity.
u_∞	Free stream velocity.
w	Fluctuating velocity in z direction.
x	Axial direction.
y^+	Dimensionless distance from the wall.
y	Inter-node distance towards the wall.
y_p	Distance to the wall from the adjacent node.
α	Particle volumetric concentration, swirl vane angle.
β	Volumetric expansion coefficient.
δ	Shear-layer thickness.
ε	Isotropic turbulence dissipation rate of the fluctuating velocity correlation $\overline{u_i u_j}$.
ρ	Density.
ρ_i	Density of component i.
$\overline{\rho}$	Mean density
λ	Molecular diffusivity of scalar quantity.
Γ	Turbulent diffusivity of heat or mass.
S_ϕ	Volumetric source term.
σ_t	Turbulent Prandtl or Schmidt number (Prandtl for heat transfer, Schmidt for mass transfer).
$\sigma_{k,\varepsilon}$	Constants in the $k-\varepsilon$ model.
μ_t	Turbulent eddy viscosity.
ϕ	Instantaneous or mean scalar quantity e.g. Temperature or specie concentration.
ϕ_i	Volume factor (fraction) i = a for gas and p for particles.
φ	Fluctuating scalar quantity.
τ	Stress.
τ_w	Wall shear stress.
η_{ij}	Coefficient of impaction of particle i and j (unity for head on).
ε	Kinetic energy dissipation rate, absolute pipe roughness.
ν	Kinematic (molecular) viscosity.
ρ	Density
β	Cyclone scaling factor.
ψ	Cyclone pressure drop factor.
μ	Fluid viscosity.
λ_0	Wave length.

Subscripts

p	Particle
f	Fluid
a	Air
r	Relative
i	i^{th} direction, i^{th} component
s	Solid.
x	Axial direction.
ω	Angular direction.

Chapter 1

Introduction

1.1 Background

Combustion by-products like sulphur dioxide, SO_2 and nitrogen oxides, NO_x can cause environmental damage such as a contribution to the causes of acid rain [81]. Although the extent of damage to the environment caused by NO_x is still a topic of research and debate, the fact that it does cause damage is not in dispute. The damage done by Nitrogen oxides is more difficult to asses than that caused by SO_2 because nitrogen oxides in the atmosphere are a natural part of the nitrogen cycle. The term *nitrogen oxides* is used to describe all nitrogen oxide species, but in combustion processes only NO and NO_2 are usually measured. Normally less than 5% of the NO_x emitted from boilers is in the form of NO_2 [103], but most of the NO is subsequently converted to NO_2 in the plume of the chimney. In fact it is conventional to quote the total burden of NO_x in terms of the equivalent NO_2.

Research work on the control and abatement of gas emission, like this project, is on the increase because of new, tougher legislation on gas emission. For example the European Commission [102, page 30], agreed to reduce sulphur dioxide

levels from large combustion plants by 20% relative to their 1980 level by 1993, by 40% by 1998 and by 60% by 2003. They also agreed to reduce NO_x levels from the same source: NO_x has to be reduced by 15% relative to its 1980 level by 1993 and by 30% by 1998 . In the UK, in 1980, power stations produced 0.85 m tonnes of NO_x equivalent as NO_2, compared with 1.79 m tonnes from all sources [103, page 33].

There are three recognized methods of controlling NO_x: Burner control, injection of chemicals in the boiler and Selective Catalytic Reduction, (SCR), where the flue gas is passed over a catalyst on which the NO_x is selectively reduced to molecular nitrogen. The cheapest method by far is burner control, which, apart from the initial capital cost, has no additional running costs. Injection of chemicals into the boiler and SCR both have running costs as well as capital costs. It is reckoned that burner control can give a 50% NO_x reduction in a purpose built plant and 70% might be attainable. Manufacturers of boiler injection systems and SCR claim reductions of up to 90% [103, page 35]. In any system, NO_x abatemenet would start with burner control, and if tighter controls were required, boiler injection or SCR would be added. The reduced levels produced by burner control would save on the running costs of the other systems.

The formation of nitrogen oxides is through three basic routes [81], see also figure 1.1.

i) Thermal: from the oxidation of atmospheric nitrogen, this accounts for about 20% of NO_x from coal fired boilers.

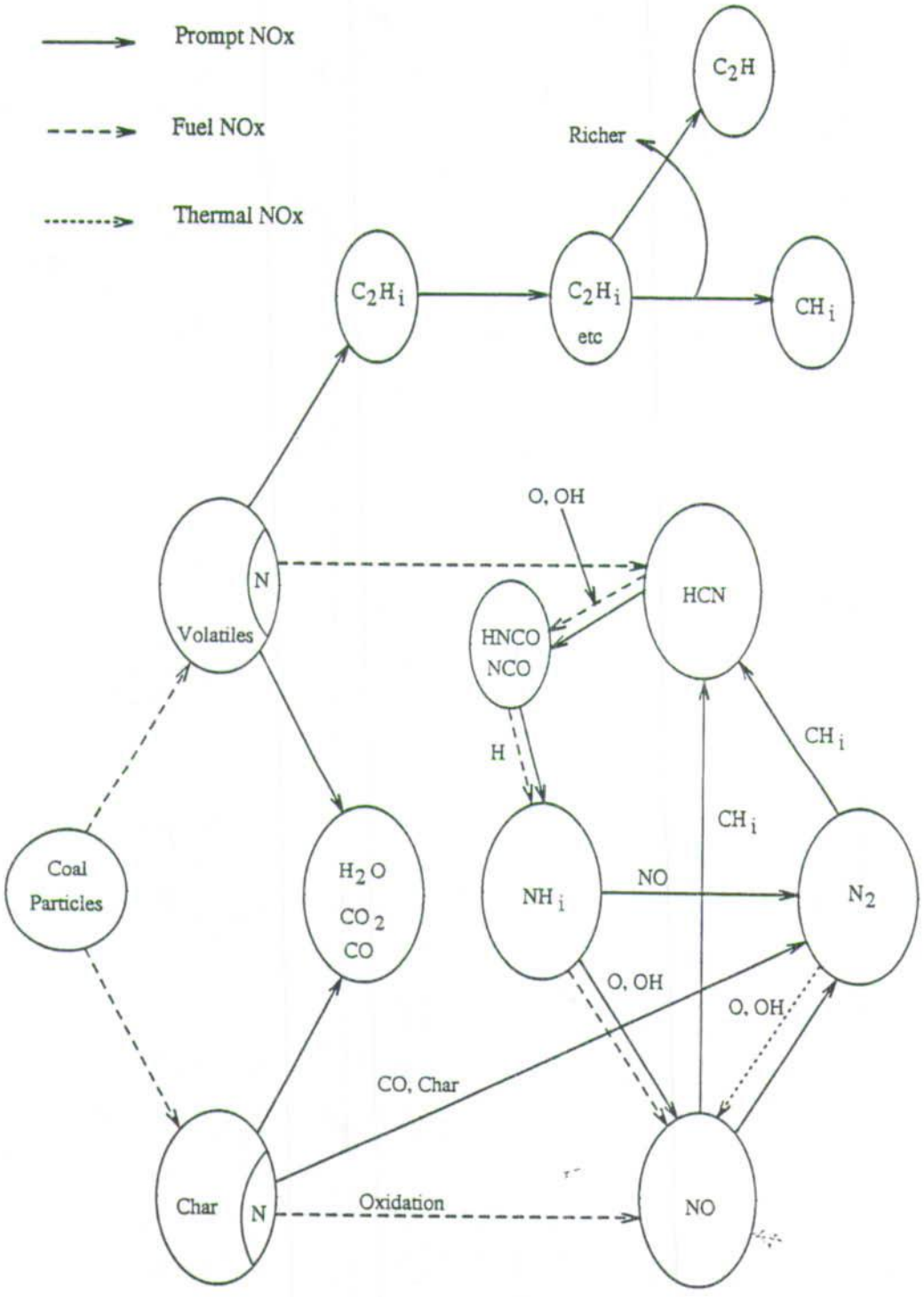

Figure 1.1: Chemical Pathways

$$N_2 + O \rightleftharpoons NO + N$$
$$N + O_2 \rightleftharpoons NO + O$$
$$N + OH \rightleftharpoons NO + H$$

Careful control of combustion conditions, particularly flame temperature, can limit emission through this route.

ii) Fuel NO_x: from nitrogen in the fuel. This is the major NO_x production route in coal fired boilers.

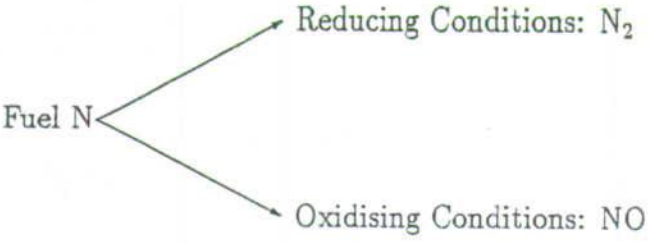

If reducing conditions are maintained in the flame regions, part of the nitrogen in the fuel can be reduced to molecular nitrogen.

iii) Prompt NO_x: from reactions between nitrogen and partially oxidized hydrocarbon fragments in the flame. Again reducing conditions can help reduce part of these species into molecular nitrogen and water vapour.

These chemical pathways are shown in figure 1.1.

It is evident that by maintaining reducing conditions and the right flame temperature in the burner, the level of NO_x emission can be reduced.

1.2 Pulverised Coal Burners

In conventional pulverised coal burners, the primary stream is divided up and its direction of flow changed several times before reaching the burner. By the time it reaches the burner, the entrained fuel is generally concentrated into 4-6 ropes.

A particle rope is a phenomenon in pneumatic transport pipes whereby a uniform dust-air mixture at the inlet of a pipe bend (normally vertical to horizontal) segregates into two regimes at the outlet: the first regime, termed a rope, is a high density ribbon of particles and the second, is mainly air.

Depending on their radial position at the point of injection into the secondary stream, the ropes either disperse immediately and burn, providing energy for the processes in the flame or persist well into the flame region and gasify, leading to relatively cool regions in the furnace. To promote efficient fuel burn-out, recirculation of the hot gases within the flame (e.g. by a swirling secondary air stream) is desirable so as to rapidly mix the oxygen and the fuel species. The resulting flame is short and intense and promotes NO_x production.

In all burner designs it is required to have as thorough mixing between the air and the fuel as possible. There are many designs and makes of Low NO_x burners, All the burners however are basically similar in that they all are all dual register burners - with a central fuel injection system with two annular registers (rings) injecting secondary and tertiary air around the fuel/air system (primary air). Figure 1.2 shows the basic arrangement of a Low-NO_x concentric firing system.

The fuel/air mixture has to be swirled to keep it fluid for injecting. Normally, at the exit, straighteners are employed to reduce the mixing with the secondary air

and enhance sub-stoichiometric combustion. For similar reasons, tertiary air tends to be directed away from the flame so that it comes into play at the far end of the flame where the char is being consumed.

Burners can be wall mounted (figure 1.3) or corner mounted (figure 1.4). The disadvantages of a wall mounted burner is that the middle part of the burner tend to have higher combustion temperatures than the upper and lower part.

Higher combustion temperatures mean more NO_x formation. Corner mounted burners are normally mounted on the four corners of the boiler and are then fired tangentially to a central fuel rich zone. In this arrangement, the central flame sees cool walls on all sides keeping the combustion temperatures down. The secondary air, is injected at an offset angle to the main firing angle, this circulates outside the central fuel-rich zone thus protecting the boiler walls from corrosion in a reducing atmosphere. Figure 1.5 show isotherms of both conventional and Low-NO_x burners.

Other variations of Low-NO_x wall mounted burners are shown in figures 1.6, 1.7 and 1.8.

In Low-NO_x burners, it is desirable to delay the arrival of oxygen until the gaseous nitrogen species derived from the fuel are reduced to molecular Nitrogen. Thereafter, rapid mixing of the remaining air with fuel is desirable in order to achieve fuel burn-out without having an excessive flame length. The overall performance of the Low-NO_x burner is critically dependent on the swirl levels and eddy structures of the secondary air stream.

Current Low-NO_x burner testing within the Central Electricity Generating Board, CEGB (now Power Gen and National Power) and elsewhere [81], [59],

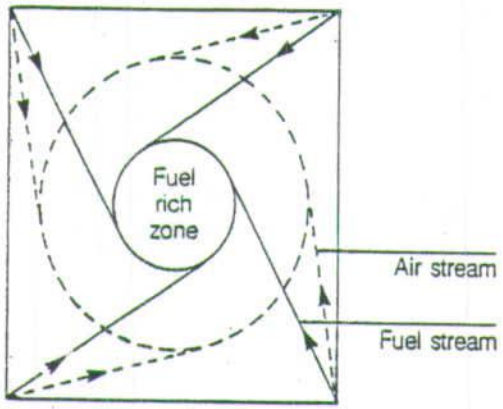

Figure 1.2: Basic Arrangements for a Low-NO_x Concentric Firing System (Head View of Wall fired Burner shown in figure 1.3

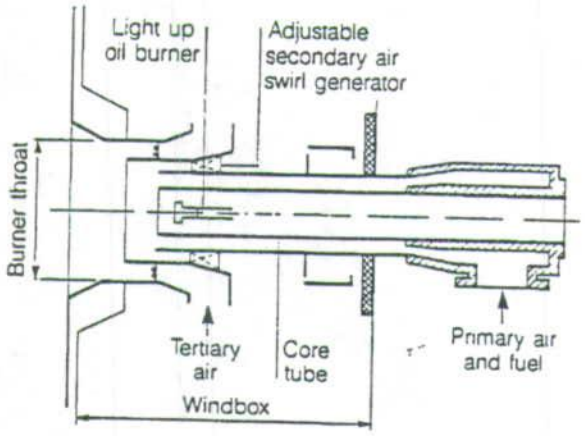

Figure 1.3: basic Layout of a Wall Mounted Dual Register Low-NO_x Burner

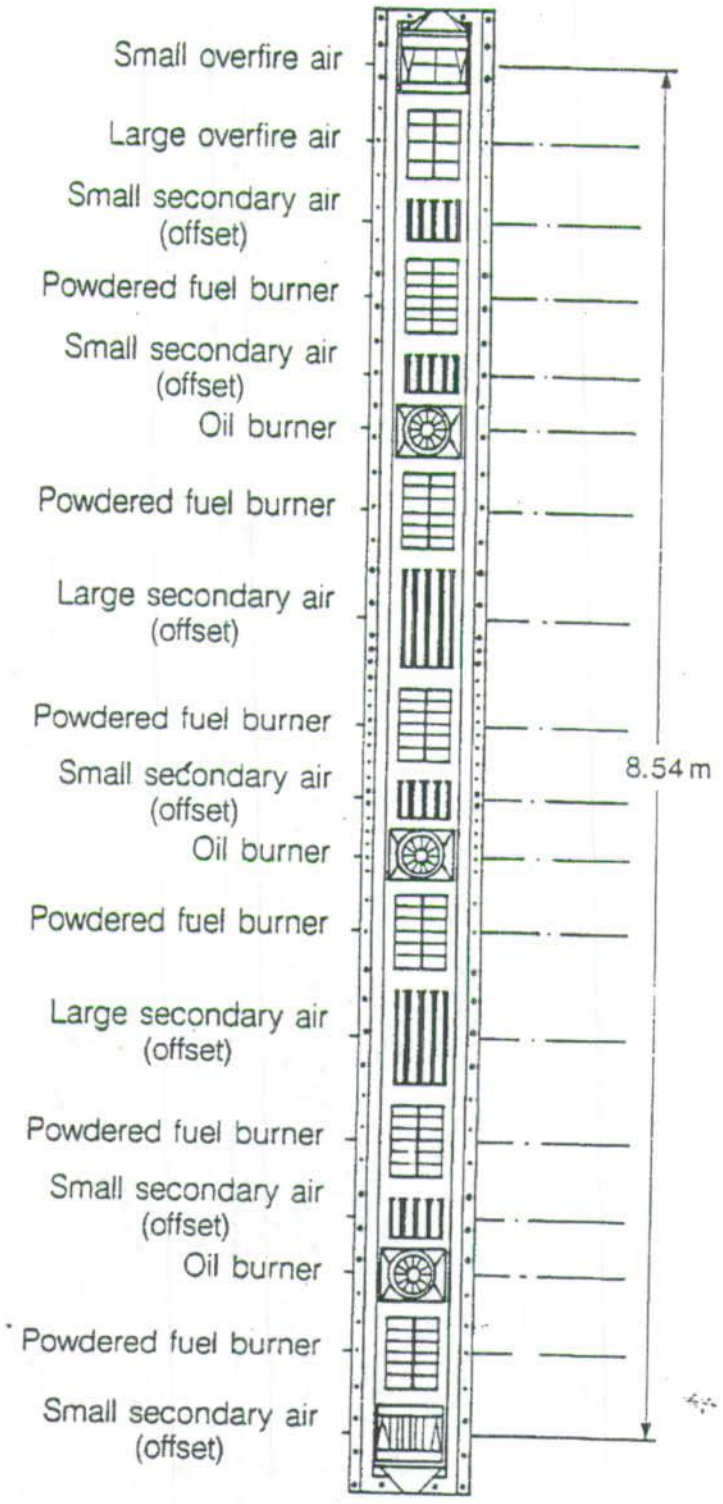

Figure 1.4: Low-NO_x Corner Mounted Burner

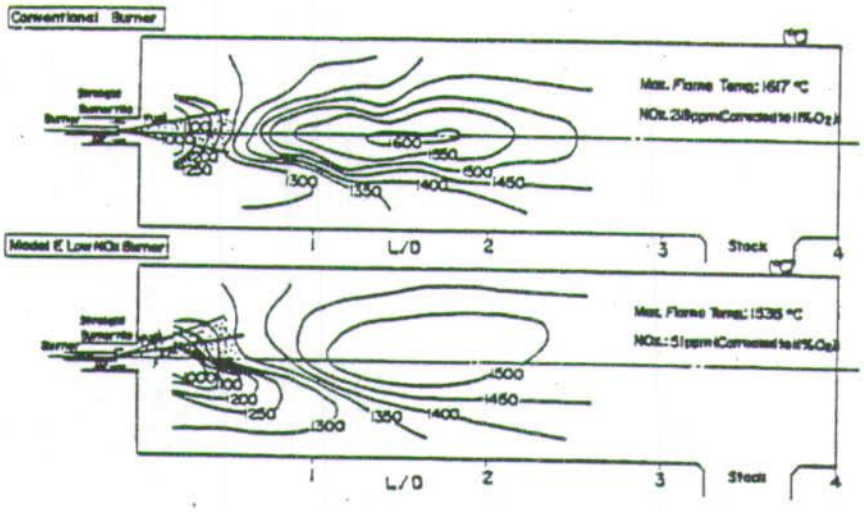

Figure 1.5: Isotherms in a Combustion Furnace

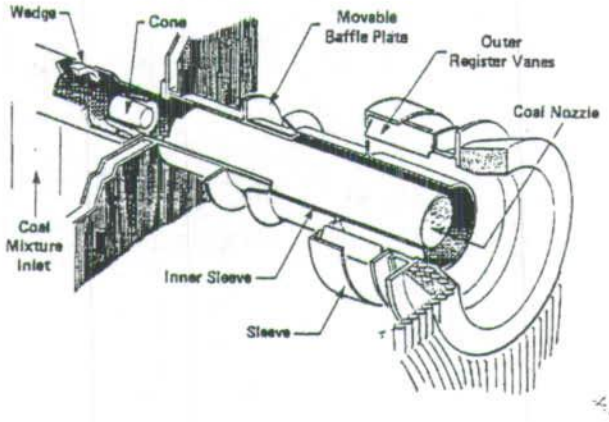

Figure 1.6: Low-NO_x Wall Mounted Burner Without a Coal Spreader

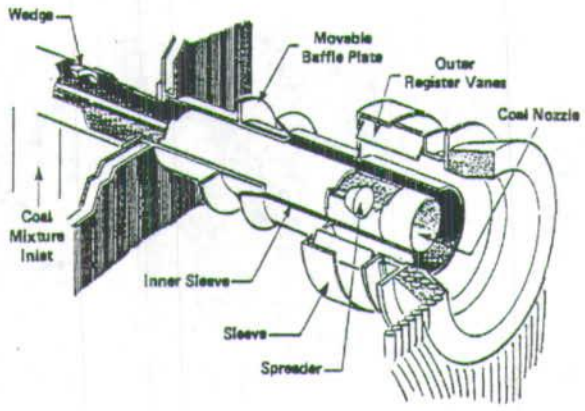

Figure 1.7: Low-NO_x Wall Mounted Burner With a Coal Spreader

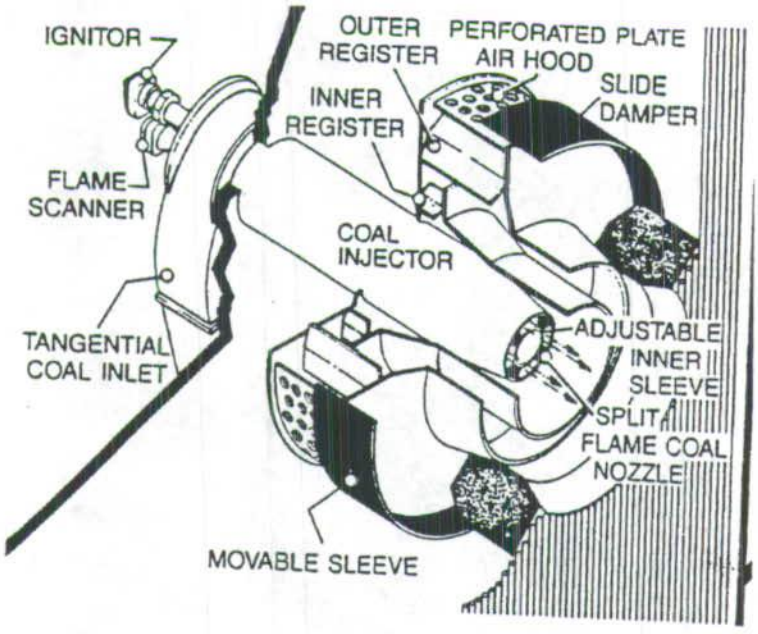

Figure 1.8: Low-NO_x Wall Mounted Burner With Flow Control

[24],[66] and [36] have shown that the mixing layer between the fuel rich (central) core of the flame and the surrounding secondary air stream is the main NO_x production zone. The mixing in this shear layer ultimately determines the amount of NO_x produced.

Understanding flow characteristics in the pulverised fuel burner could give additional scope for improving the growing number of Low-NO_x burner designs which in principle enhance production of molecular nitrogen while maintaining sufficient boiler efficiency.

This fundamental investigation will explore conditions relevant to the design and operation of a range of equipment of industrial interest. Ranges of velocity, particle sizes, and particle number density will be used to provide an understanding of the fluid mechanics of particle "ropes" and the physical reasons for their persistence and eventual breakup. The study will help to obtain data that will complement available empirical (industrial) knowledge of roping behaviour. The data will be valuable in developing new numerical models and/or verifying existing ones.

1.3 Research Objectives

It is important to state here that combustion is a complex process. As pointed out above, the production of NO_x depend among other things on the flame temperature, availability of the fuel species and the mixing of the fuel species with the air. A simplified approach was adopted to study this process by just studying the mixing, stability and dispersion of the particle jet/rope. The project objectives thus were to employ the Particle Image Velocimetry (PIV)

technique to study the basic physical parameters which affect the stability and dispersion characteristics of particle "ropes" by measuring particle velocities and trajectories. Laser Doppler Anemometry (LDA) was to be used to augment the PIV measurement technique in cases where the Doppler signal might not be attenuated (low particle density). LDA was used particularly in making initial studies/characterisation of the flow fields in the test section.

LDA velocity measuring technique relies on the formation of a set of fringes caused by the interference of two overlapping coherent beams. In transmission mode, a particle crossing these fringes will block off much of the light in the bright fringes and only a little light in a dark fringe. The light transmitted by a particle crossing a set of fringes will will fluctuate at the rate at which the particle crosses the fringes, modulating at a frequency equal to the ratio of velocity to particle diameter (U/d).

PIV is a velocity measuring technique which can "instantaneously" record velocity over a whole flow field. The technique relies on photographing small particles contained in and faithfully following the flow under investigation. The velocity information on the film can be recovered by ascertaining the separation of the particle images. This can be done by either observing the film directly using a microscope or, more commonly, by interrogating each point on the film using a low power laser beam (optical interrogation) or by digitising the whole doubly exposed image and storing the digital image in the computer memory for subsequent analysis.

Both LDA and PIV techniques are well documented and are still undergoing further development and refinements. They have been used in diverse research/experimental work e.g. in particle characterization [47], in breaking

waves [14], in acoustic streaming [15], in fluid velocity measurements [109], [65], [87] and [46], in measurement of surface displacement and tilt [8] etc. See also [16], [30], [87], [35], [125] and [62]. Their success relies on the suitable properties of the laser light. Both these techniques depend on the availability of a powerful source of coherent light to locate and track the particles.

Laser, acronym for Light Amplification by Stimulated Emission of Radiation, is a light source which works by taking the light from one atom to stimulate the emission of more light from other atoms. Amplification is provided by an active medium, which can be a fluid, solid, or by semiconductors. Laser is commonly thought of as giving a bright, highly coherent, highly monochromatic light. Some typical laser light sources are shown in appendix A, see also [113].

The advantages of both LDA and PIV include offering very high accuracy without the need for system calibration and having fast response and high spatial resolution. Their being non-intrusive make them attractive for use in corrosive and toxic environments. The need for a transparent medium, optical access and use of scattering particles and the fact that signal processing equipment is expensive can inhibit their use.

In the next chapter, Turbulence Theory is revisited. Chapter 3 deals with flow simulation using a commercial package called FLUENT. Chapter 4 details the design of the experimental rig, while chapter 5 covers the testing of experimental rig and LDA experiments.

Although the original ambition of the project was to make Particle Image Velocimetry, (PIV) measurements of the particle rope, it transpired that in this initial stage of the project most of the time was spent in designing and construction of the rig and the timing could not allow for the PIV studies. To

compliment the preliminary LDA experiments and the simulation work done, it was decided to carry out some PIV measurement of jet dispersion in a small square wind tunnel (simulation work was done using a square section). This experimental work is covered in chapter 6. Conclusions, critique and recommendations are in the last chapter, chapter 7.

Chapter 2

Turbulence Theory Revisited

2.1 General

All shear flows become turbulent at a high enough Reynolds number, indeed most flows of practical relevance are almost always turbulent, i.e. the fluid motion is highly random, unsteady and three dimensional.

Turbulent motion and the heat and mass transfer phenomena associated with it are extremely complex and difficult to describe analytically. In only a minority of fluid dynamical situations can one determine the flow as an exact solution of the equations of motion. The necessary mathematical methods often do not exist. Even when an exact solution can be obtained, it may not be unique and so may not correspond to what actually occurs. Numerical methods are available, but require massive computer time and storage capacity. Hence, much of fluid dynamics concerns the development of both experimental and theoretical procedures for elucidating flows that can not be rigorously calculated [118].

Recent literature on the subject is voluminous, unfortunately not all of it is useful, or even correct [117].

This is a summary, aimed at discriminating the theory for those approaches that have sound qualitative and quantitative refinement but still retain the simplicity to be of practical engineering relevance in solving/predicting turbulent flow transport quantities.

2.2 Turbulence: Phenomena and Nature

When tangential stresses are applied to a fluid having internal friction, various kinds of secondary motions can develop: regular ones, usually imposed by the shape of the boundaries, can be readily accounted for in terms of pressure gradients. Irregular ones (creating eddying and rotational motion), usually prevailing at high Reynolds number, can be accounted for by a simple explanation.

Turbulence is "a state of continuous instability", each time a flow changes as a result of an instability, one's ability to predict the details of the motion is reduced. When successive instabilities have reduced the level of predictability so much that it is appropriate to describe a flow statistically, rather than in every detail, then one says that the flow is turbulent. Random features of the flow then become dominant, but, still, turbulent flow is not completely random. For details see also [117],[74], [3], [108], [51], [39], [40], [106] and [118].

2.2.1 Diffusiveness of Turbulence

Turbulent flow features (e.g. frictional effects, mean velocity distributions, rate of spreading, etc.) have little similarity with those found in laminar flow

because the diffusiveness of turbulence far exceeds molecular diffusion and has more intimate connection with the mean flow.

In Turbulence, energy is fed into the turbulence primarily through the larger eddies, from there smaller eddies are generated, and then still smaller ones. The process continues until the length scale is small enough for viscous action to be important and dissipation to occur. The process is called an energy cascade.

The number of these cascade energy exchange stages increases with the Reynolds number. Energy dissipation, though a viscous process, is independent of the magnitude of the viscosity but is determined by the rate of supply of energy to the cascade by the large scale eddies and is independent of the dynamics of the small eddies in which the dissipation actually occurs [118].

An increase in Reynolds number to a still higher value can conveniently be visualized as a change to a fluid of lower viscosity, if everything else is held constant. This only extends the cascade at the small eddy end: still smaller eddies must be generated before dissipation can occur. Since the energy associated with these small eddies is small, this extension has negligible effect on the total energy of the turbulence [74], [48] and [118].

The mean flow always has a preferred direction imposed by the large-scale turbulent motion. At high Reynolds number, the large scale and small scale motions are sufficiently apart in the spectrum (direction of sensitivity lost) and small scale dissipative motions, like the large scale ones, also become isotropic [74]. The turbulent velocities which contain the bulk of the turbulent energy, tend to maintain a constant ratio to the mean local velocity (termed as form preservation) and this is an important feature of turbulent flow.

Large eddies are determined by the boundary conditions of the flow, they have low frequency fluctuations and their size is of the same order of magnitude as the flow domain. Their size at any position downstream is predetermined by their initial size and what happened upstream. The smallest eddies, which are associated with the high frequency fluctuations, are determined mainly by the viscous forces. The width of the spectrum and thus the difference between the largest and the smallest eddies increases with the Reynolds number. The large scale turbulent motion is, however, mainly responsible for the transport of momentum and heat and contributes to the turbulence correlations ($\overline{u_i u_j}$) and $\overline{u_i \varphi}$ see equations (2.6) and (2.7). These correlations are the ones that have to be simulated in turbulent models [106].

2.3 Turbulent Motion Equations

The basis of the equations is mass, momentum, thermal energy and species quantity conservation. A statistical approach is normally used to separate mean and fluctuating quantities ($i = 1, 2, 3$ for x, y, and z direction respectively):

$$\frac{\partial}{\partial x_i}(\overline{U}_i + u_i) = 0 \tag{2.1}$$

which, on averaging, for incompressible flow (ρ = constant):

$$\frac{\partial \overline{U}_i}{\partial x_i} = 0 \tag{2.2}$$

subtracting equation 2.2 from 2.1 gives:

$$\frac{\partial u_i}{\partial x_i} = 0 \tag{2.3}$$

Thus the mean and fluctuating parts of the velocity field individually satisfy the usual form of the continuity equation.

Applying a similar division to the Navier-Stokes equations for an incompressible fluid (ρ = constant) gives for:

momentum:

$$\frac{\partial(\overline{U}_i + u_i)}{\partial t} + (\overline{U}_j + u_j)\frac{\partial(\overline{U}_i + u_i)}{\partial x_j} = -\frac{1}{\rho}\frac{\partial(\overline{P} + p)}{\partial x_i} + \nu\frac{\partial^2(\overline{U}_i + u_i)}{\partial x_j^2} + g_i\rho \tag{2.4}$$

averaging out:

$$\frac{\partial \overline{U}_i}{\partial t} + \overline{U}_j\frac{\partial \overline{U}_i}{\partial x_j} + \overline{u_j\frac{\partial u_i}{\partial x_j}} = -\frac{1}{\rho}\frac{\partial \overline{P}}{\partial x_i} + \nu\frac{\partial^2 \overline{U}_i}{\partial x_j^2} + g_i\rho \tag{2.5}$$

with the aid of the continuity equation (2.2), for steady mean flow ($\frac{\partial \overline{U}_i}{\partial t} = 0$), the above equation can be re-written as:

$$\overline{U}_j\frac{\partial \overline{U}_i}{\partial x_j} = -\frac{1}{\rho}\frac{\partial \overline{P}}{\partial x_i} + \nu\frac{\partial^2 \overline{U}_i}{\partial x_j^2} - \frac{\partial}{\partial x_j}\overline{(u_i u_j)} \tag{2.6}$$

Temperature/species concentration:

$$\frac{\partial \overline{\phi}}{\partial t} + \overline{U}_i \frac{\partial \overline{\phi}}{\partial x_j} = \frac{\partial}{\partial x_i}(\lambda \frac{\partial \overline{\phi}}{\partial x_j} - \overline{u_i \varphi}) + S_\phi \rho \tag{2.7}$$

where ϕ is a scalar quantity (heat or concentration). S_ϕ is a volumetric source term, expressing, for example, heat generation due to chemical or biological reactions, λ is the molecular diffusivity. Similarly for steady mean flow:

$$\overline{U}_i \frac{\partial \overline{\phi}}{\partial x_j} = \frac{\partial}{\partial x_i}(\lambda \frac{\partial \overline{\phi}}{\partial x_j} - \overline{u_i \varphi}) + g_i \rho \tag{2.8}$$

Thus the difference from the laminar flow is the term $\frac{\partial}{\partial x_j}(\overline{u_i u_j})$ in equation (2.6) and the term $\overline{u_i \varphi}$ in equation (2.7). The first term $\overline{U}_j \frac{\partial \overline{U}_i}{\partial x_j}$ in equation (2.6) represents the actions of the velocity fluctuations on the mean flow arising from the non-linearity of the Navier-Stokes equations, and is frequently large compared with the viscous term, with the result that, the mean velocity distribution is very different from the corresponding laminar flow.

Some literature [118] reports that, in some experimental work, the term $\partial(\overline{u_i^2})/\partial x_j^2$ has experimentally been found not to be so small, and it is not uncommon to find such terms being retained in some equations. Note that the last two terms of equation (2.6) can be written as:

$$\frac{1}{\rho}\frac{\partial}{\partial x_j}(\mu \frac{\partial \overline{U_i}}{\partial x_j} - \rho \overline{uv}) \tag{2.9}$$

primarily to help show that the velocity fluctuations produce a stress on the mean flow. A gradient of this produces a net acceleration of the fluid in the same way as a gradient of the viscous stress. The quantity $\mu\frac{\partial\overline{U}_i}{\partial x_j}$ is the shear stress, while $(-\rho\overline{u_1u_2})$ or more generally $\rho\overline{u_iu_j}$ is called the Reynolds' stress.

The Reynolds' stress arises from the correlation of two components of velocity fluctuations at the same point. A non-zero implies the two are not independent of one another. e.g. if $\overline{u_1u_2}$ is negative, then at moments at which u_1 is positive, u_2 is more likely to be negative than positive; conversely when u_1 is negative. This analogy has led to the definition of, in analogy to the shear stress, a quantity μ_t, such that:

$$-\overline{u_iu_j} = \mu_t\frac{\partial\overline{U}_i}{\partial x_j} \tag{2.10}$$

μ_t, the eddy viscosity, is a representation of the action of the turbulence on the mean flow and not a property of the fluid. Sometimes, for simplicity, μ_t is treated as constant rather than as a correlation for $\overline{u_iu_j}$.

The division of a turbulent motion into (interacting) motions of various length scales is useful because the different scales (so called eddies of different sizes) play rather different roles in the dynamics of the motion.

In isotropic turbulence (homogeneous turbulence in which the statistical properties do not vary with position and have no preferred direction, e.g. in motion downstream of grids), the energy production term, $\overline{u_iu_j}\frac{\partial\overline{U}_i}{\partial x_j}$, is zero, this implies that the motion must decay through viscous dissipation. In theoretical work, the turbulence is supposed to be generated at an initial instant and then

decay as time proceeds.

The governing equations of the fluid, e.g. equations (2.3), (2.6) and (2.8) are non-linear differential equations. They also do not form a closed set as they contain unknown correlations between fluctuating velocities $\overline{u_i u_j}$ and between velocity and scalar quantities, $\overline{u_i \varphi}$, introduced by the averaging process. The term $\rho\overline{u_i u_j}$ is the transport of x_i momentum due to turbulent motion in the x_j direction and $\rho\overline{u_i \varphi}$ is the transport of x_i scalar due to turbulent motion in the x_j direction (and vice versa). Specification of any problem must thus be accompanied with the necessary boundary conditions, e.g. at a rigid wall $u = v = w = 0$ at $y = 0$ for all x and z.

Viscous stresses in the $x-$, $y-$ and z direction can be extracted in the Cartesian coordinates:

$$\mu(\frac{\partial u}{\partial y} + \frac{\partial v}{\partial x})_{y=0} \; ; \; 2\mu(\frac{\partial v}{\partial y})_{y=0} \; ; \; \mu(\frac{\partial w}{\partial y} + \frac{\partial v}{\partial z})_{y=0} \tag{2.11}$$

since from the continuity equations:

$$\frac{\partial v}{\partial y} = -\frac{\partial u}{\partial x} - \frac{\partial w}{\partial z} \tag{2.12}$$

and also, $u = v = w = 0$ at $y = 0$ for all x and z, this implies that the viscous shear stress at the wall is

$$\mu(\frac{\partial u}{\partial y})_{y=0} \; ; \; 0 \; ; \; \mu(\frac{\partial w}{\partial y})_{y=0} \tag{2.13}$$

Note that $\mu\frac{\partial u}{\partial y}$, and $\mu\frac{\partial w}{\partial y}$ are tangential stresses, $\frac{\partial v}{\partial x} = 0$ is the normal stress, zero normal stress implies that there is no viscous force, but there is pressure per unit area in the normal (y) direction.

Equations (2.6) to (2.7) can be solved if $\overline{u_i u_j}$ and $\overline{u_i \varphi}$ can be determined in some way. Turbulence models are used to approximate these correlations and are covered in section 2.5.

2.4 Turbulent Motion Near the wall

The presence of the wall, effectively, forces the fluid "to see" the wall as generating drag that slows the fluid. The fact that both the fluctuating and mean flows drop to zero at the wall implies that, at the wall, the Reynolds' stress $\overline{u_i u_j} = 0$. Thus the only stress exerted directly on the wall is the viscous one. Away from the wall, on the other hand, the turbulence generates a Reynolds' stress, large compared with the viscous stress. The total stress, τ, is:

$$\tau_{ij} = \mu\frac{\partial \overline{U}_i}{\partial x_j} - \rho\overline{u_i u_j} \tag{2.14}$$

where τ_{ij} is the shear stress in i direction in a plane normal to the direction j.

Rapid variation of τ_{ij} with x_j (y), would produce very large mean acceleration that can not possibly be matched by the mean flow distribution. Near the wall, $\overline{u_i u_j}$ is small and so there is little energy production: far from it, $\frac{\partial \overline{U}_i}{\partial x_j}$ is small with the same consequence. The rate of energy production $\overline{u_i u_j}\frac{\partial \overline{U}_i}{\partial x_j}$ has a large peak close to the wall. Mathematically:

$$-\overline{u_i u_j}\frac{\partial \overline{U}_i}{\partial x_j} = -\frac{1}{\rho}(\tau_{ij} - \mu\frac{\partial \overline{U}_i}{\partial x_j})\overline{U}_i \partial x_j \tag{2.15}$$

If τ_{ij} is constant and $\mu\frac{\partial \overline{U}_i}{\partial x_j} = \tau_{ij}/2$, energy dissipation is largest in the vicinity of the changeover from predominantly viscous stress, ('wall-region'), to predominantly turbulent stress. The conditions in the wall region can be specified as $U = f(u_t, y, \nu)$, u_t is a velocity scale defined as $u_t = \sqrt{\frac{\tau_w}{\rho}}$, and depends on the whole flow. Applying dimensional analysis, shows that $u/u_t = f(y, u_t, \nu)$. As viscosity is only important very close to the wall, and less important with increasing y, then, the mean velocity gradient can be said to be: $\frac{\partial \overline{U}_i}{\partial x_j} = f(u_t, x_j)$. This however is only true for the velocity gradient, and not for velocity, as the velocity, $\overline{U}_i$ is separated from its origin by a region in which ν is important.

This led to the division of the turbulent boundary layer into inner and outer regions. Flow in the "wall region" has a characteristic velocity scale provided by the value of τ_{ij}.

Viscosity is important only very close to the wall, as you move away from the wall (increasing $y, i.e. x_j$), viscosity ceases to play a significant role long before parameters $\overline{U}_i = f(u_t, y, \mu)$ start to have influence. Thus, one can say that the mean velocity gradient depends only on u_t and y, i.e. $\frac{\partial \overline{U}_i}{\partial y} = f(u_t, y)$, but not for all $\overline{U}_i$ because it is separated from its origin by a region in which ν is important.

Applying dimensionless analysis to:

$$\frac{\partial \overline{U}_i}{\partial y} = f(u_t, y) \tag{2.16}$$

gives:

$$\frac{\partial \overline{U}_i}{\partial y} = u_t / Ky \tag{2.17}$$

K is a universal constant (Kármán constant), experimentally found to be about 0.41 [118], [106] and [95].

Integrating equation 2.17 gives:

$$\frac{\overline{U}_i}{u_t} + \frac{1}{K}[ln(\frac{yu_t}{\nu}) + A] \tag{2.18}$$

A is another constant ≈ 5.2 [95] (but is strong function of the roughness Reynolds number, $\overline{U}_{wall}/u_t$ etc.). $\overline{U}_{wall}$ is fluid velocity in the vicinity of the wall.

Equation (2.18) is commonly known as the logarithmic wall law equation. It is known to depart from this distribution for $yu_t/\mu > 30$. It is valid in the "wall-region" which typically can occupy about one-tenth of the boundary layer thickness.

2.5 Turbulence Models

The exact equations (2.2) to (2.7) are non linear and do not form a closed set and turbulence models have to be used to approximate the unknown correlations between fluctuating velocity $\overline{u_i u_j}$ and between velocity and scalar $\overline{u_i \varphi}$. Turbulence models are used for this purpose, some of which are are covered below.

2.5.1 Basic Concepts

Among many approaches used to model the turbulent or Reynolds' stress, $(\rho\overline{u_i u_j})$ the most significant ones rely on the eddy-viscosity and the eddy-diffusivity concepts.

2.5.1.1 Eddy-Viscosity (Boussinesq's) Concept

The turbulent or Reynolds' stress, $\overline{u_i u_j}$ can be modeled by assuming that the turbulent stresses are proportional to the mean-velocity gradients in analogy to the viscous stress in the laminar flows. This can generally be put as:

$$-\overline{u_i u_j} = \mu_t\left(\frac{\partial U_i}{\partial x_j} + \frac{\partial U_j}{\partial x_i}\right) - \frac{2}{3}\delta_{ij} \tag{2.19}$$

The turbulent or eddy viscosity, μ_t, (not a fluid property) depends strongly on the state of turbulence. δ_{ij}, is added to make the expression (2.19) applicable also to normal stresses (i = j).

The first part of equation 2.19 involving the velocity $\overline{U_1^2} = -2\mu_t \frac{\partial U_1}{\partial x_1}$, $\overline{U_2^2} = -2\mu_t \frac{\partial U_2}{\partial x_2}$, $\overline{U_3^3} = -2\mu_t \frac{\partial U_3}{\partial x_3}$, whose sum, is zero, i.e. $\sum \overline{u_i^2} = 0$ (because of the continuity equation). Since the normal stresses, by definition are positive quantities, their sum is twice the kinetic energy of the fluctuating motion $k = \frac{1}{2}\sum \overline{u_i^2}$, the second part, ensures that the sum of the normal stresses is equal to $2k$.

The analogy though not strictly correct, is used mainly because μ_t can be determined to a good approximation in many flow situations ($\mu_t \sim vl$) where shear stress is the turbulent stress of prime importance such as in two-dimensional thin shear layers (boundary-layer type of flow).

The Eddy-viscosity concept sometimes fails in wall jets and axisymmetric wall shear layers as there exist regions where the stress, τ, and the velocity gradient $\frac{\partial \overline{U}_i}{\partial x_j}$ may have opposite directions such as flow in an annulus or channels with different wall roughness on either side. But since $\mu_t \sim$ *mixing length*, vl and $vl > 0$, a negative μ_t though a possibility mathematically from equation (2.19) has no physical meaning.

2.5.1.2 Eddy-Diffusivity Concept

In direct analogy to turbulent momentum transport, turbulent heat or mass transport is often assumed to be related to the gradient of the transported quantities in which case a turbulent diffusivity can be defined such that:

$$-\overline{u_i \varphi} = \Gamma \frac{\partial \overline{\phi}}{\partial x_i} \tag{2.20}$$

Where $\Gamma = \frac{\mu_t}{\sigma_t}$ is the turbulent diffusivity of heat or mass (like the eddy viscosity, is not a fluid property but depends on turbulence), σ_t = turbulent Prandtl or Schmidt number. (Prandtl for heat transfer, Schmidt for mass transfer).

2.5.2 Classification Of Turbulence Models

2.5.2.1 Zero-Equation Model

This is a class of simple models. They all employ the eddy viscosity concept (but do not use any transport equations for turbulence quantities). The eddy viscosity is specified either directly from experiments, or by trial and error, or through empirical formulae or by relating it to the mean-velocity distribution.

The most common models are the constant eddy viscosity/diffusivity model, the Prandtl Mixing-length model and Prandtl Free shear hypothesis.

In Prandtl Mixing-Length hypothesis, the turbulent viscosity is assumed to be proportional to the local mean fluctuating velocity gradient and to a single unknown parameter, the mixing-length, l_m; i.e. $v = l_m \mid \frac{\partial \overline{u}}{\partial y} \mid$. Assuming the proportionality constant is unity: $\mu_t = \mid \frac{\partial \overline{u}}{\partial y} \mid l_m^2$ [1], see [3], [108] and [106]. The concept is useful for simple flows especially in free shear layer flows where l_m can be assumed constant across the layer and proportional to the local layer width δ (δ is defined as a distance from the symmetry axis giving a 1% velocity variation).

---

[1] From $\overline{uv} = \mu_t \frac{\partial \overline{U}}{\partial y}$, taking $\tilde{u} = l \frac{\partial \overline{u}}{\partial y}$, and assuming that when $\tilde{u}$ is large, $\tilde{v}$ is also large, one can define, $\tilde{v} = \beta \tilde{u}$. Then, $\overline{uv} = l^2 \beta (\frac{\partial \overline{u}}{\partial y})^2$, and so, $\mu_t = l^2 \beta \frac{\partial \overline{u}}{\partial y}$, and if $\beta \simeq 1$, $\mu_t = l^2 \frac{\partial \overline{u}}{\partial y}$.

The model is unsuitable when processes of convective or diffusive transport of turbulence are important e.g. in rapidly developing flows, in heat transfer across plumes with zero velocity gradients, recirculating flows and generally of little use in complex flows because of great difficulties in specifying the mixing length, l_m (see also [69] and [105]).

The Prandtl Free shear hypothesis is based on the assumption that the eddy-viscosity, μ_t is constant over the layer cross section, and that the length scale, l, is proportional to the layer width, δ and velocity scale v (equal to the maximum velocity difference $\mid U_{max} - U_{min} \mid$). Thus $\mu_t = c\delta \mid U_{max} - U_{min} \mid$. The model works well for predicting the velocity profile in mixing layers, jets and wakes, especially when considering its developed state. Transition velocity profiles are not however, predicted well.

2.5.2.2 One-Equation Model

In this class of models, the turbulent transport quantities are accounted for by solving the differential transport equations. Common models include those based on the eddy-viscosity concept and those based on the kinetic energy.

2.5.2.2.1 Models Using The Eddy-Viscosity Concept

These characterize velocity fluctuations by one physically meaningful scale, $\sqrt{k}$, $k = \frac{1}{2}(\overline{u_1^2} + \overline{u_2^2} + \overline{u_3^2})$ is the kinetic energy of the turbulent motion per unit mass. As k is contained mainly in large scale fluctuations, it becomes a direct measure of the intensity of the turbulence fluctuations in the three directions and serves as velocity scale for the large scale motion. When this scale is used in

the eddy-viscosity concept ($\mu_t \propto vl$):

$$\mu_t = c'_\mu \sqrt{k} l \tag{2.21}$$

Where c'_μ is an empirical constant. Equation (2.21) is known as the Kolmogorov-Prandtl expression. The rate of change of k is balanced by the convective transport due to the mean motion, the diffusion transport due to velocity and pressure fluctuations, the production of k by the interaction of the Reynolds' stresses and the mean-velocity gradients and the dissipation of k by viscous action into heat. In buoyant flows, there is also production or destruction of k due to buoyant forces. The production term represents the transfer of kinetic energy from the mean to turbulent motion, buoyant term represent the exchange between the turbulent kinetic energy and potential energy. The distribution of k is determined by solving a transport equation for this quantity from the corresponding Navier-Stokes equation. With above assumptions, the model equation becomes:

$$\underbrace{\frac{\partial \overline{k}}{\partial t}}_{rate} + \underbrace{\overline{U}_i \frac{\partial \overline{k}}{\partial x_i}}_{convective} = \underbrace{\frac{\partial}{\partial x_i}\overline{[u_i(\frac{u_j^2}{2} + \frac{P}{\rho})]}}_{diffusive} - \underbrace{\overline{u_i u_j}\frac{\partial \overline{U}_i}{\partial x_j}}_{production} - \underbrace{\beta g_i \overline{u_i \varphi}}_{buoyancy} - \underbrace{\nu \frac{\partial \overline{U_i}}{\partial x_j}\frac{\partial \overline{U_i}}{\partial x_j}}_{dissipation} \tag{2.22}$$

Different transport mechanisms are shown underneath the equations.

2.5.2.2.2 k-equation Model

The exact k-equation, equation (2.22) contains an additional unknown correlation in the diffusion and dissipation terms. To obtain a closed set of equations, model assumptions are required. In analogy to the diffusion expression ($\mu_t \propto vl$) for the quantity ϕ, the diffusion flux of k is often assumed to be proportional to the gradient of k; i.e. $\overline{u_i(\frac{u_j^2}{2} + \frac{P}{\rho})} \propto \frac{\partial k}{\partial x_i}$; thus $\overline{u_i(\frac{u_j^2}{2} + \frac{P}{\rho})} = \frac{\mu_t}{\sigma_k}\frac{\partial k}{\partial x_i}$; The viscous dissipation rate per unit mass, ε, is governed by large scale eddies (characterized by k and l) motion even though the dissipation takes place through smaller eddies. It is usually modeled by $\varepsilon = C_D\frac{k^{\frac{3}{2}}}{l}$ (C_D and σ_k are empirical constants). The model is restricted to high Reynolds number and is not applicable in the viscous sub-layer. Empirical constants are functions of turbulent Reynolds number, $Re_t = \frac{vk\rho}{\mu}$. To date there are many extensions and revisions of the model.

2.5.2.3 Two-Equation Models

In turbulent flows, the eddies' size depends on their initial size and what happened upstream. Dissipation destroys the small scale eddies, effectively increasing the average eddy sizes. Vortex stretching on the other hand, tends to reduce eddy sizes. The balance of these processes can be expressed (modeled) in a transport equation for the length scale l, which can be used to calculate the distribution of l. Most models use the eddy-viscosity concept and the Kolmogorov-Prandtl expression or a variation thereof (e.g. Kolmogorov: $\varepsilon \propto \frac{k^{\frac{3}{2}}}{l}$, Spalding: $\varepsilon \propto \frac{k}{l^2}$; etc). The $k-\varepsilon$ and the turbulent stress/flux models are the most common and realistic models in this group. The $k-\varepsilon$ model in particular is very popular and well tested.

Unlike all the other models, the Reynolds' stress/flux-equation model employs various velocity scales in the transport equations for the individual stresses $\overline{u_i u_j}$ and $\overline{u_i \varphi}$ and not a single velocity scale as related by either the eddy-viscosity, Kolmogorov-Prandtl expression or any of their variants. This is more appropriate for complex flows.

2.5.2.3.1 The Generalised Standard $k-\varepsilon$ Model

At high Reynolds number, where local isotropy prevails, the rate of dissipation, ε, is equal to the product of kinematic (molecular) viscosity and the fluctuating vorticity, $(\overline{\frac{\partial u_i}{\partial x_j}})^2$. An exact transport equation can be derived from the Navier-Stokes equation for the fluctuating velocity and thus the dissipation, but the resulting equation is too complex and of little practical relevance. Often the ε equation is modeled together with the k-equation and the Kolmogorov-Prandtl expression to give the so called $k-\varepsilon$ turbulence model. The equations used are:

$$\mu_t = c_\mu \frac{k^2}{\varepsilon}, \quad \Gamma = \frac{\mu_t}{\sigma_k} \tag{2.23}$$

$$\underbrace{\frac{\partial k}{\partial t}}_{Rate} + \underbrace{U_i \frac{\partial k}{\partial x_i}}_{Convection} = \frac{\partial}{\partial x_i}\left(\frac{\mu_t}{\sigma_k}\frac{\partial k}{\partial x_i}\right) + \underbrace{\mu_t\left(\frac{\partial U_i}{\partial x_j} + \frac{\partial U_j}{\partial x_i}\right)\frac{\partial U_i}{\partial x_j}}_{Production} + \underbrace{\beta g_i \frac{\mu_t}{\sigma_t}\frac{\partial \phi}{\partial x_i}}_{Buoyancy/destruction} - \varepsilon \tag{2.24}$$

$$\underbrace{\frac{\partial \varepsilon}{\partial t}}_{rate} + \underbrace{U_i \frac{\partial \varepsilon}{\partial x_i}}_{Convection} = \underbrace{\frac{\partial}{\partial x_i}\left(\frac{\mu_t}{\sigma_\varepsilon}\frac{\partial \varepsilon}{\partial x_i}\right)}_{diffusion} + \underbrace{C_{1\varepsilon}\frac{\varepsilon}{k}\left[\mu_t\left(\frac{\partial U_i}{\partial x_j} + \frac{\partial U_j}{\partial x_i}\right)\frac{\partial U_i}{\partial x_j} + \beta g_i \frac{\mu_t}{\sigma_t}\frac{\partial \phi}{\partial x_i}\right] - C_{2\varepsilon}\frac{\varepsilon^2}{k}}_{Generation - Destruction} \tag{2.25}$$

where σ_ε, $c_{1\varepsilon}$, and $c_{2\varepsilon}$ are empirical constants. The different transport mechanisms are shown underneath the equations see also [115] and [106].

2.5.3 Experimental Model: The Modified $k - \varepsilon$ Model

Flow simulation is described in detail in chapter three. The simulation model is based on a modified $k - \varepsilon$ model. This uses different constant values from those used in the standard model to increase its accuracy in predicting wall turbulent shear and the wall limiting behaviour. Although these constants used are valid throughout the fully turbulent, the semi-laminar (transition) and laminar flow ranges, the model's accuracy is still poor in situations where there are adverse pressure gradients [115], [90] and [118]. Flow simulation is covered in detail in chapter 3.

In the experiment, there was scope for varying both the primary and secondary air flows and injecting varying particle loading densities in the case of two-phase studies.

2.6 Two-Phase Flows

The dispersion of particles by turbulent shear flow is an intrinsic part of many technological processes e.g. dispersion of liquid droplets in gas combustion and the mixing of coal particles by the input jets of coal fired power plants, cyclone separators, as well as in rocket exhausts containing ash or unburnt metal powders [69] and [104]. In many of these processes, the dispersion of the particles is a controlling factor in the efficiency and the stability of the process [104]. Despite considerable progress in analytical and experimental studies, the design of particle transport systems largely relies on empirical correlations due to the complex mechanisms involved in gas-particle, particle-particle and particle-pipe wall interactions.

In practice there are enormous and difficult fundamental problems such as selecting feasible theory among a large collection of examples. The traditional method for predicting the dispersion of discrete particles in turbulent flow is the so-called tracking method which uses statistical simulation where trajectories of the particles are computed with the aid of the equations of motion [2], [77] and [97]. Equations of motion used are generally oversimplified; in a lot of cases, Newton's law is expressed with the Stokes' law drag force alone [71] and [97]. Furthermore, this drag force is usually written as a function of the difference between the mean fluid and mean particle velocities meaning that the basic equations used to describe the phenomena are purely deterministic and not stochastic as turbulence is. See also [92], [7], [61], [18], [85] and [86].

2.6.1 Physical Model for Gas-Particle Flows

Interaction between the particles and the fluid is based on their size, relative velocity and the difference in densities. The mean relative velocity between the gas and the particles is mainly a function of the size and material density of the particles. This interaction can be correlated by a particle Reynolds number, Re_p.

$$Re_p = \frac{(U_f - U_p)\rho_f d}{\mu_f} = U_r d\frac{(\rho_p - \rho_f)}{\mu_f} \tag{2.26}$$

and the particle relaxation time t"

$$t" = \frac{d^2\rho_p}{18\mu_f\rho_f} \tag{2.27}$$

where μ_f is the fluid kinematic viscosity. The relaxation time, $t"$, is the time it takes a particle to accelerate from rest to within 63% of the fluid velocity and is correct only for Stokes' regime, $Re_p < 1$ [26], [18], [104], [70] and [72].

The modeling of gas-particle interaction is done by regarding the conveying gas-phase as two interactive fluids (two-fluid equation equation model) which exchange momentum, energy and mass with each other. Depending on the physical models about the interactive exchanges of momentum, energy, pressure gradient and the constitutive relation between stress and strain in the particle phase, there have appeared in literature several different derivations of the "two-fluid" equations.

In all these derivations the main assumptions are that the relative velocity

between the two-phases is negligible (mixing-length model used). Such assumptions are valid only for small Stokes' numbers [2]. If Stokes' number is not small and if the mean velocity of the conveying fluid is slow, the particles are not able to respond quickly to changes in the gas flow. In such cases, the effect of the relative velocity becomes significant.

In addition, it is normally assumed that the turbulent kinetic energy of the conveying fluid is generated by both the primary fluid and the fluctuating solid particles, but that it is dissipated by the primary fluid only. Recently it was shown analytically that the turbulent kinetic energy is dissipated by the relative motion between the two phases as well as by the primary fluid itself [69].

Most earlier conventional theoretical treatment based on the flow-field classification of single-phase flows divides the flow into two fixed transverse regions: the turbulent, diffusion controlled core and the fluid controlled quasi-laminar region [72].

In the turbulent diffusion controlled core region, the particle motion is assumed to be controlled entirely by turbulent fluid oscillations and the particles are assumed to be transported in the same way as scalar quantities by the turbulent diffusion of the fluid. In the mean fluid controlled quasi-laminar region, the particle motion is assumed to be controlled entirely by the mean fluid motion through the drag interaction.

Results of calculations using this scheme on particulate wall deposition have been found to differ from measurements by as much as four orders of magnitude

---

[2]Stokes number is defined as $St = mg\rho(1 - \frac{\rho}{\rho_f})R^3/\mu^2$ where m = mass of particles, R = tube diameter, ρ, ρ_f density of particle and fluid respectively [124, page F-319]

[72]. There are several weakness in this approach, the main ones are:

i) In the turbulent core, particles are assumed to be transported by turbulent diffusion of the fluid, secondly,

ii) In the quasi-laminar region, particle transport is assumed to be controlled entirely by the viscous drag.

iii) The location of the divide between the two transverse regions is assumed to be fixed and is to be determined from the flow field classification of the corresponding single phase flow, combining the turbulent core and the buffer zone to form the turbulent core for suspension flow and identifying the viscous sublayer as the quasi-laminar region for the suspension flow.

iv) There is a lack of rational explanation of the turbulent particle diffusion mechanism which is assumed to exist.

v) The unjustified use of known flow properties of corresponding single-phase flow in the study of particle transport in turbulent two-phase suspension flows.

In practice, particles being transported in a turbulent flow, in general will not be evenly distributed in the transverse direction and thus a local transverse particle concentration gradient usually exists. The fluctuating motion of the fluid will then be affected by this uneven distribution of particles. The fluid will find it more difficult to pass through in the direction of increasing concentration than in the direction of decreasing particle concentration. A larger drag will have to be overcome in the direction of increasing concentration [71]. Thus the main shortcoming of the theories lies in the assumption of an artificial boundary

which separates the two artificial transverse regions; the turbulent core and the quasi-laminar sublayer; they deal with these two regions as two separate entities- usually two unconnected sets of governing equations, one each for the two regions, having no physical or mathematical ties with each other, therefore these theories can not produce a smooth transition of flow properties across the flow field in the transverse direction [72], which is particularly important when studying dispersion characteristics.

2.6.1.1 One-D Solid-Gas Flow Model.

The capability of analytically predicting the flow characteristics of a gas-solid mixture is important for design and development of many industrial processes and components for energy-conversion systems. Several analytical models have been developed that involve a one dimensional model of flow behaviour through a duct, nozzle or venturi [26].

The early approaches were to assume dynamic and thermal equilibrium between the solid phase and the fluid phase, which corresponds to a single phase, homogeneous fluid with modified properties. Particle-particle interaction was not modeled.

The basic assumptions are: see also [18] and [106]:

- Density of the particles is much greater than that of the fluid $\rho_p \gg \rho_f$,
- Particle-particle interactions neglected
- The effect of the particles on the flow is neglected

- Virtual mass force, pressure gradient forces and Basset forces[3] all neglected
- Other force fields including gravity are not included
- all particles are rigid spheres of diameter d_p and density ρ_p
- The two-phase flow is dilute and the effect of particles and particle-particle interaction can be neglected. This is true for low particle volumetric concentration (volume fraction tending to zero [2]). The particle volumetric concentration, α, in the suspension can be computed from the particle to air mass flux ratio, m,:

$$\alpha = \frac{1}{\frac{s}{m}\frac{U_p}{U_a} + 1} \tag{2.28}$$

where α is the particle volumetric concentration and $s = \frac{\rho_p}{\rho_f}$; particle-to-air density ratio and m is the particle-to-air mass flux ratio (see also [70]). The particle size can be made dimensionless by the introduction of the Froude number, F_r:

$$F_r = \frac{U_0}{(d_p g)^{0.5}} \tag{2.29}$$

U_0 is the time mean fluid velocity.

This model is similar to that in [26] developed for variable area, but has been modified to be used for non varying areas. The model is thus bound to be sensitive to pressure drop and particle size.

---

[3]Basset forces account for the effect of the deviation in the flow pattern from steady state (increase the instantaneous flow resistance), their effect can be substantial in cases where particles are accelerated at high rate by a strong external force [51, page 463].

The governing equations are:

Continuity: solids:

$$\dot{m}_{pi} = \phi_i \rho_p U_{pi} A \tag{2.30}$$

where $i = 1 \ldots n$, represents a group of particles of diameter d_i, $\dot{m}$ is mass flow rate, ϕ is the volume fraction, subscript p refer to particles.

$$\dot{m}_p = \sum_i \dot{m}_p = \rho_p \sum_i \phi_i U_{pi} A \tag{2.31}$$

Continuity: gas:

$$\dot{m}_a = \rho_a \phi_a U_a A \tag{2.32}$$

Note that $\phi_a = 1 - \sum_i \phi_i = 1 - \phi_p$

Gas-Particle Momentum:

$$\rho_a U_a \phi_a \frac{dU_a}{dx} + \rho_p \sum_i \phi U_{pi} \frac{dU_{pi}}{dx} = -\frac{dp}{dx} - \frac{4\tau_w}{D_h} - [\phi_a \rho_a + \rho_p \phi_p] g \tag{2.33}$$

p is the fluid static pressure, D_h is the hydraulic diameter. Reorganise to

eliminate the fluid velocity gradient gives:

$$[1 - \phi_a \frac{U_a^2}{RT}]\frac{dp}{dx} = \phi_a \rho_a U_a^2[(1 + \frac{\phi_p}{\phi_a})\frac{1}{A}\frac{dA}{dx} + \frac{1}{\phi_a}\sum_i \phi_i \frac{1}{U_{pi}}\frac{dU_{pi}}{dx}] - \rho_p \sum_i \phi_i U_{pi}\frac{dU_{pi}}{dx} - \frac{4\tau_w}{D_h} - (\phi_a \rho_a - \phi_p \rho_p)g$$

where R is the gas constant and T is temperature. For $\frac{dp}{dx} = 0$ (true for most turbulent jets [117], [2], [69] and [104]) and $\frac{dA}{dx} = 0$ (i.e. axisymmetric $D_h = D$) then:

$$\rho_a U_a^2 \sum_i \frac{1}{\phi_{pi}}\frac{dU_{pi}}{dx} = \rho_p \sum_i \phi_i U_{pi}\frac{dU_{pi}}{dx} + \frac{4\tau_w}{D} + (\phi_a \rho_a + \phi_p \rho_p)g \qquad (2.34)$$

The force acting on a particle i due to collision by a cloud of particles j in addition to fluid drag is:

$$U_{pi}\frac{dU_{pi}}{dx} = F_i(U_a - U_p) + \sum_j F_{ij}(U_{pj} - U_{pi}) - g \qquad (2.35)$$

where x is the direction of motion and g is the gravitational acceleration and where:

$$F_i = \frac{Drag\ force\ due\ to\ fluid}{m_{pi}(U_a - U_{pi})} \qquad (2.36)$$

and

$$F_{ij} = \frac{Drag\ force\ due\ to\ collision\ by\ i\ particles}{m_{pi}|U_{pj} - U_{pi}|} \tag{2.37}$$

F is interpreted as the time constant for momentum transfer due to drag force, for spherical particles:

$$F_i = \frac{3}{4} C_{D_i} (\frac{\rho_a}{\rho_p}) \frac{| U_a - U_p |}{d_i} \tag{2.38}$$

and

$$F_{ij} = \frac{\frac{3}{2}\eta_{ij}(d_i + d_j)^2 \mid U_{pj} - U_{pi} \mid \phi_j}{d_i^3[1 + (m_{pj}/m_{pi})]} \tag{2.39}$$

where η_{ij} is the coefficient of impaction of particle i and j (unity for head on).

It is important to note that whenever relative motion exists between a particle and a surrounding fluid, the fluid will exert a drag upon the particle. The drag force on the particle is given by:

$$F_d = \frac{C A_p \rho U^2 g}{2} \tag{2.40}$$

where C is the drag coefficient and A_p is the particle projected area in the direction of motion. Except in turbulence and similar extraneous effects, it makes no difference whether the fluid moves past the particle or the particle moves through the fluid.

The drag force between the solid particles and gas is a function of Reynolds number, $R_p = \rho_a d_p \frac{|U_a - U_p|}{\mu_a}$.

Where $C_D = 0.44$ for $R_p >= 1000$; or $C_D = \frac{24}{R_p}(1 + 0.15R_p^{0.687})\ for\ R_p < 100$, the average density $\overline{\rho} = \sum_i \phi_p \rho_p + \phi_a \rho_a$.

The effect of particle-wall interaction on the skin friction factor is small and may be neglected if volume fraction of solids is negligible $< 1\%$. However to be more accurate and account for the presence of solids in the gas, the classical Fanning factor formula for friction factor for turbulent gas flow is replaced by an equivalent friction factor for the solid-gas mixture (see also [26]) as:

$$C_{f_{solid-gas}}/c_{f_{gas}} = (1 + x)^{0.3} \tag{2.41}$$

where x = solid to gas mass loading (valid for up x = 0.5), C_i is the fanning factor. See [26])

2.7 Results of Previous Two-Phase Flow Studies

For two-phase flow of sufficient diluteness and small particle Reynolds numbers, the Stokes' drag law, which is based on an unbounded laminar stream passing over a single spherical particle, has generally been regarded as an acceptable approximation for laminar as well as turbulent two-phase suspension flow [70].

In two-phase flows, it has been found that, in the core region, the gas leads the particles while it lags behind the particles near the wall. This is due to the fact

that the fluid does not slip at the wall where particles do. Consequently, the air mean velocity profile is flatter in the core of the pipe and steeper near the wall. This effect is augmented by increasing the mass loading ratio or decreasing the particle size [105]. The mean relative velocity between the gas and the particles is mainly a function of the size and material density of the particles, and the location of vanishing relative velocity moves away from the wall by decreasing the mass loading ratio.

Significant reduction of the fluid turbulent shear stress occurs due to the dissipating effects of the particles. This is accompanied by a decrease in the turbulent kinetic energy. Particulate matter suspended in the boundary layer interacts with the dominant structures, and this interaction may be quite complex. For the same mean-flow Reynolds number, a more powerful blower is needed for pumping a gas-solid suspension in a vertical pipe than is required for gas alone. Treating the suspension as a fluid alone is thus inaccurate [105]. It is normally assumed that the turbulent kinetic energy is dissipated by the fluctuations of the particle phase as well as by the primary conveying fluid.

Particles with a low Re_p tend to suppress turbulence of the carrier fluid; for example, particles with $Re_p < 100$ would suppress the turbulence and have similar effects to an increase in viscosity. Large particles (1000μm) can cause an increase in the measured values of turbulent intensities and Reynolds' stress. Small particles (120μm) bring about a decrease in the measured intensities and Reynolds' stress. The above effects are enhanced as the particle loading is increased. Smaller (88μm) glass particles do not bring about any significant modulation of turbulence, which might be interpreted as signifying negligible gravitational effects [3].

Particle dispersion depends strongly on Aerodynamic response time, $t^* = \frac{\rho_p d_p^2}{18\mu}$ (the time required for a spherical particle to be accelerated to 63% of the fluid velocity from rest) and is valid in Stokes' drag law range only. For larger t^* (higher Stokes number), there is less particle dispersion. At intermediate t^* values, particles might be dispersed faster than the fluid and actually fly outside the fluid mixing region of the jet.

The predicted modification of the law-of-the wall by the particles suggest that the use of single phase law-of-the-wall for two phase flow is an inaccurate representation of the real situation for volumetric loading ratios > 0.0005.

In event of swirl, there is a strong separation of particles from swirling flows, while in non-swirling flows, the jet spread is only slight [26], [79] and [97].

2.8 Comments On Model Selection and Literature

The "Two-fluid" model see [69] offer a more realistic approach, this model has been left out only because it is not possible, with the current experimental set-up to measure the particle and gas velocity simultaneously. This limitation might apply to the testing of the 'One-D Solid-Gas' flow model as well.

The literature on Turbulence Theory and Turbulence Models, as pointed out earlier is large and still expanding. Of the literature cited, [102], [103], [11] and [29] coverage on Turbulence theory are recommended while [5], [102], [11] and [29] are recommended for their coverage of Turbulence models.

Chapter 3

Fluid Flow Simulation Using *FLUENT*

FLUENT, version 3.02, a proprietary commercial computational dynamics package from Creare Incorporated of Hanover, New Hampshire, USA was used.

FLUENT, like most fluid dynamics computations packages solves the Navier-Stokes equations on "grid-based" geometry. The accuracy of any *FLUENT* simulation will thus, depend upon the choice of this computational grid. It is important to note that flow features on the scale of the grid spacing or finer, can not be predicted.

Finer grid spacing (short distance between nodes and large number of cells) demands more computational time and storage memory, they however offer better accuracy (e.g. of shear stress and that of heat transfer predictions) at the wall; course grids, on the other hand, can give rise to numerical errors. The high accuracy of finer grids, though desired, must always be compromised to match the computational resources available. The simulation work done was in 2D setup and the package was run on SUN 3 workstation, a 50 x 50 grid was the maximum grid size possible.

3.1 Turbulence Modeling

FLUENT flow modelling is based on the solutions of the Navier-Stokes equations: the differential mass and momentum conservation equations and the differential transport equation for the kinetic energy of the fluctuating motion k, and its dissipation rate, ε. These written in tensor notation (see chapter 2) are:

Mass conservation:

$$\frac{\partial}{\partial t}(\rho) + \frac{\partial}{\partial x_i}(\rho U_i) = 0 \tag{3.1}$$

Momentum conservation:

$$\underbrace{\frac{\partial}{\partial t}(\rho U_j)\frac{\partial}{\partial x_i}(\rho U_i U_j)}_{convection} = \underbrace{\frac{\partial}{\partial x_i}(\mu[\frac{\partial U_i}{\partial x_j} + \frac{\partial U_j}{\partial x_i}])}_{diffusion} - \underbrace{\frac{\partial p}{\partial x_j}}_{pressure} + \underbrace{\rho g_j + \overbrace{F_j}^{Interaction}}_{body\ forces} \tag{3.2}$$

The mass and momentum equations given above describe the mean or time-averaged flow when applied to a finite number of discrete control volumes (grid cells). Turbulence effects can be included either by decomposing the velocities into separate terms for the mean and fluctuating components (Reynolds' decomposition) and adopting a sensible model for the resulting Reynolds' stresses or by substituting an "effective" viscosity in the existing equations consisting of the molecular viscosity augmented with its turbulent counterpart, μ_f (effective viscosity hypothesis).

The effective viscosity hypothesis is employed by *FLUENT* because of its simplicity compared to the Reynolds' stress modelling. The distribution of the turbulent viscosity is provided by the parameters of the turbulence model used. In the k-ε model used, the kinetic energy of the fluctuating motion, k and its

dissipation rate ε.

Kinetic energy, k:

$$\frac{\partial}{\partial t}(\rho k) + \frac{\partial}{\partial x_i}(\rho U_i k) = \frac{\partial}{\partial x_i}[\mu \frac{\partial k}{\sigma_k \partial x_i}] + \mu_t(\frac{\partial U_j}{\partial x_i} + \frac{\partial U_i}{\partial x_j})\frac{\partial U_j}{\partial x_i} \tag{3.3}$$

and Dissipation rate, ε:

$$\frac{\partial}{\partial t}(\rho \varepsilon) + \frac{\partial}{\partial x_i}(\rho U_i \varepsilon) = \frac{\partial}{\partial x_i}[\mu \frac{\partial \epsilon}{\sigma_\varepsilon \partial x_i}] + C_1 \frac{\varepsilon}{k}\mu_t(\frac{\partial U_j}{\partial x_i} + \frac{\partial U_i}{\partial x_j})\frac{\partial U_j}{\partial x_i} - C_2 \rho \frac{\varepsilon^2}{k} \tag{3.4}$$

where

$$\mu_t = \rho C_\mu \frac{k^2}{\varepsilon} \tag{3.5}$$

The k-ε model parameters used in *FLUENT* are:

$$C_1 = 1.44,\ C_2 = 1.92,\ C_\mu = 0.09,\ \sigma_k = 1.0\ and\ \sigma_\varepsilon = 1.3$$

These constants were used as recommended in literature and *FLUENT* package suppliers as being valid for the $k - \varepsilon$ model.

The differential equations above are non linear and elliptic [107] in nature [1]. Boundary conditions must be specified at all boundaries of the domain being considered [118] and [93]. See also chapter 2. In figure 3.1 boundary conditions

[1] A partial differential equation $au_{xx} + 2bu_{xy} + cu_{yy} - f(x, y, u, p, q) = 0$; $(p = u_x; q = u_y)$ where a, b, c are given functions of the independent variables x and y; and f is a given function of the five indicated variables. The magnitude of the discriminant $b^2 - ac$ at any point or throughout the given domain determines the classification of the differential equation and is:

hyperbolic if $b^2 - ac > 0$
parabolic if $b^2 - ac = 0$
elliptic if $b^2 - ac < 0$

for two dimensional axisymmetric flow are shown.

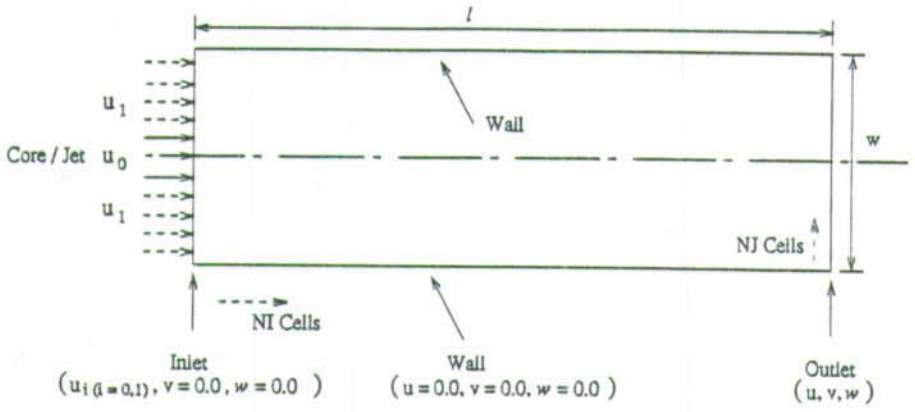

Figure 3.1: Sketch of Simulation Flow Section

Since for highly swirling flows the effective viscosity may be strongly directional, the k-ε model may be inadequate, in such cases the Algebraic Stress Model, ASM could be initiated, this solves algebraic approximations of the differential transport equations for the Reynolds' Stress, this is thus more general and fundamental. For all flows where the swirl number was less than 1.0, the k-ε model was used as recommended. Although *FLUENT* recommends use of the ASM, comparative study of turbulence models [80] in predicting turbulent pipe flow suggest that ASM does not predict the mean fluctuating velocity, $\overline{u^2}$ and the turbulent kinetic energy, k very well, especially near the wall region. It has been suggested that this is because the wall effect term is not adequately represented because there is no modification of the k diffusion term to account for the effect of the wall proximity as in the case in the $k-\varepsilon$ models.

FLUENT deals with the near the wall region by matching the features with finite-difference equations and cutting the link between the boundary and near wall nodes by setting appropriate coefficients to zero.

The set of simultaneous algebraic equations 3.1 - 3.4 are solved by a semi-implicit iterative scheme [93] and [68] which starts from arbitrary initial conditions (except at the boundaries) and converge to the correct solution (satisfying the governing equations) after performing a number of iterations. The iteration steps are:

1. The u, v (and w where applicable) and momentum equations are each solved in turn using guessed pressure.

2. Where velocities do not satisfy the mass continuity equation locally, a "Poisson-type" [2] equation [37] is derived from the continuity equation and the linearised momentum equation. This gives a pressure correlation equation which is then solved to obtain the necessary corrections to the pressure field. This in turn is used to make adjustments to the corresponding velocity components.

3. The k-ε equations are solved using the updated velocity field to obtain the distribution of the effective viscosity.

4. Any auxiliary equations (e.g. enthalpy, species, radiation, turbulence properties, etc.) are solved using previously updated values of the other variables.

5. Where inter-phase coupling is to be included, the source terms of the appropriate gas flow equations are augmented.

The above iteration steps are carried out until the error mentioned in (2) above has decreases to the specified convergence level.

---

[2] $f(x + y) + f(x - y) = 2(f(x)f(y)$

3.2 Convergence, Residual and Numerical Stability

At each iteration, *FLUENT* reports a residual for each equation that has been solved, this provides a measure of the degree to which each equation is satisfied throughout the flow field. The residuals reported are a summation of the imbalances in the equation for all cells in the domain for each conservation equation. A well converged solution gives normalized residual of the order of 10^{-3} (10^{-6} for enthalpy). If the residuals have decreased to this level and are monotonically decreasing, and the flow field looks unchanged from the solution 50 iterations earlier, then the solution is considered to have converged.

All simulation runs were done according to *FLUENT* recommendations [55], these are:

i) Inlet and outlet cells should be defined by a minimum of two or three cells. Where large gradients are expected as in shear layer or mixing zones, the grid should be fine enough to minimize the change in the flow variables from node to node. Separated regions should include at least 5 or 6 cells across the separation. In general any flow passage should not be represented by fewer than 3 or 4 cells.

ii) Spacing between wall and the adjacent grid line can impact the accuracy of the computed shear stress and heat transfer coefficients particularly in laminar flow. The recommended grid spacing $y_p\sqrt{\frac{u_\infty}{\nu_x}} \leq 2$. For turbulent flows, the log-law is used in the turbulent boundary layer and the distance recommended is $50 < y^+ < 100$ where $y^+ = \rho y \frac{u_t}{\mu}$, u_t is a friction velocity defined as $u_t = \sqrt{\tau \frac{u}{\rho}}$.

iii) Avoid aspect ratio greater than 5:1 except where gradients in one direction

are very small relative to those in the second direction (e.g. in fully developed pipe flow). Excessive aspect ratio can lead to convergence difficulties and/or the propagation of numerical errors.

Uniform grids were used for two reasons: they are easy to generate and secondly to avoid possible undesired grid distribution. The use of uniformly distributed grids however results in having some cell boundary not located precisely at a desired location. The use of non uniform grids on the other hand allows reducing the grid spacing in regions where high gradients are expected and increasing the spacing where the flow is relatively uniform. The correct rate of change of grid spacing should be minimised to between 20% and 30%.

Furthermore, all simulations were done using rectangular coordinates for two reasons: Firstly previous users of *FLUENT* in the department reported less than satisfactory results where simulations were done in polar coordinates, and secondly because most of the PIV experiments were planned to be done in a square glass section.

3.3 Simulation Results

All simulations were done in a 2D format. Many simulation runs were made but only two sets are reported here. The first set is a simulation of a 10 mm jet diameter into stagnant air region. The velocity of this jet was varied between 5 and 40 m/s. The thickness/width of the stagnant air region was also varied from 30 mm to 100 mm. See figures 3.3 to 3.9.

In the second set, mixing of two jets of different velocities was simulated.

Simulation runs for velocity ratios (annular/core) of between 0.67 and 1.5 were done. See figures 3.11 to 3.14. To help inspect the velocity vectors in the whole flow section, a zoom plot of the region outside the core is also included. This was obtained by increasing the vector scaling three fold. In all vector plots, the same relative vector scaling is used, i.e. the maximum vector length is based on the value of u_0.

3.3.1 Air Jet into Stagnant Air

In the first group of this set, a 10 mm diameter jet issuing at 20 m/s into a stagnant air region whose width was varied between 150 mm to 50 mm (figures 3.3 to 3.5). In the second group of the set, the effect of changing the velocity of the issuing jet was investigated (figures 3.6 to 3.9). A sketch of the inlet conditions is shown in figure 3.2.

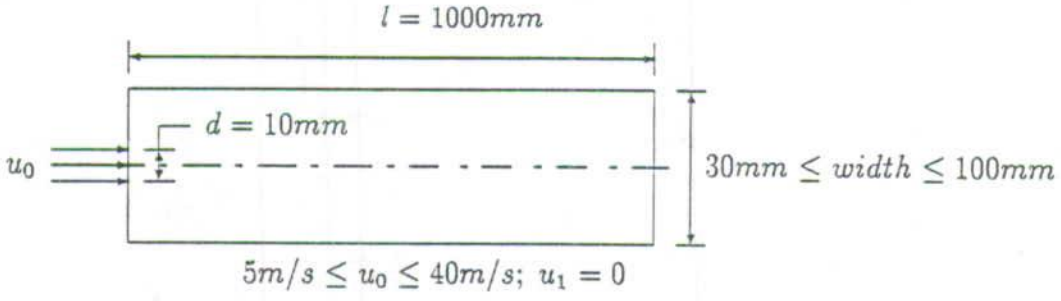

Figure 3.2: Inlet Conditions For Jet Into Stagnant Air region

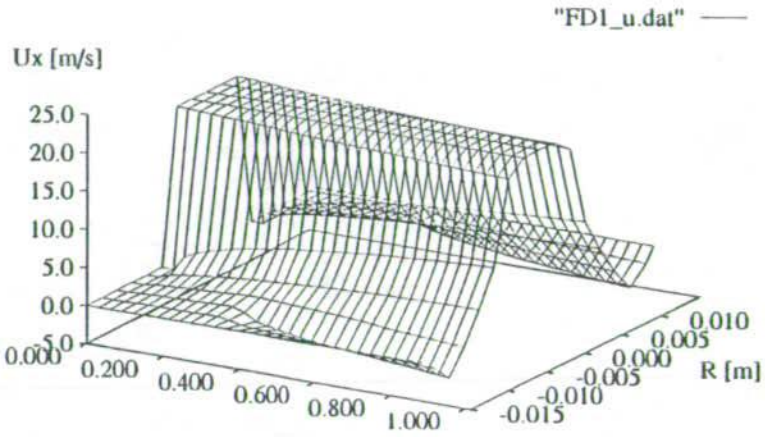

(a) Axial Velocity

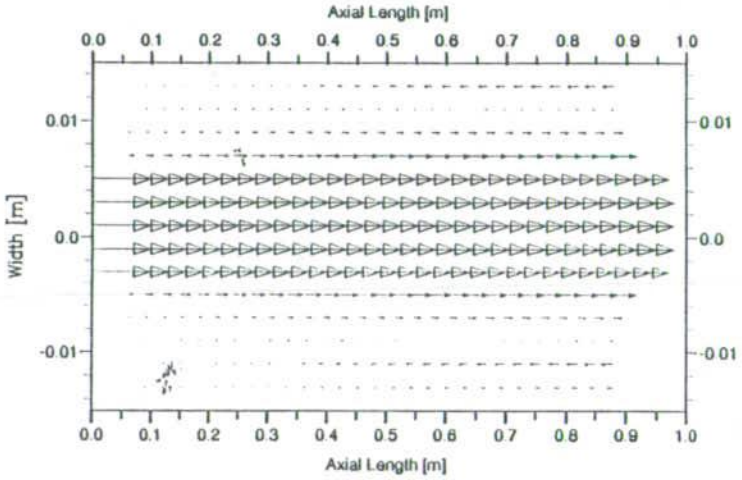

(b) Velocity Vectors

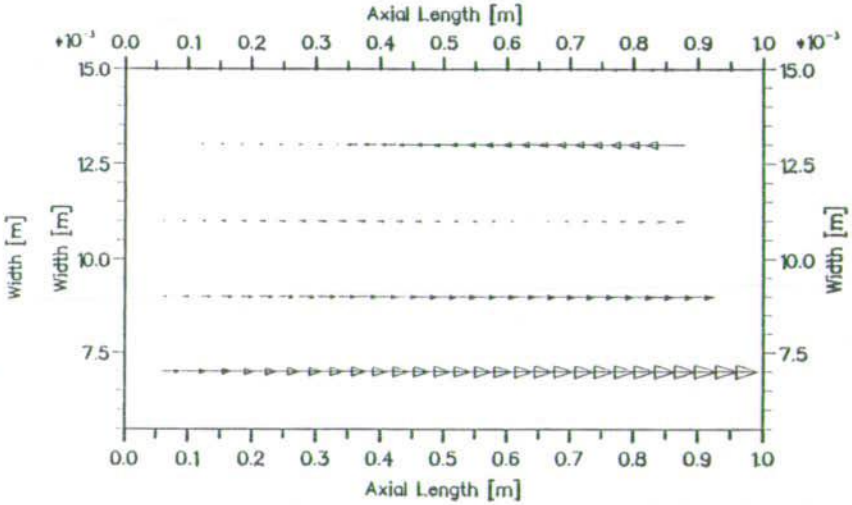

(c) Zoom Outside Core

Figure 3.3: 20 m/s Jet into 30 mm Diameter Stagnant Air Region

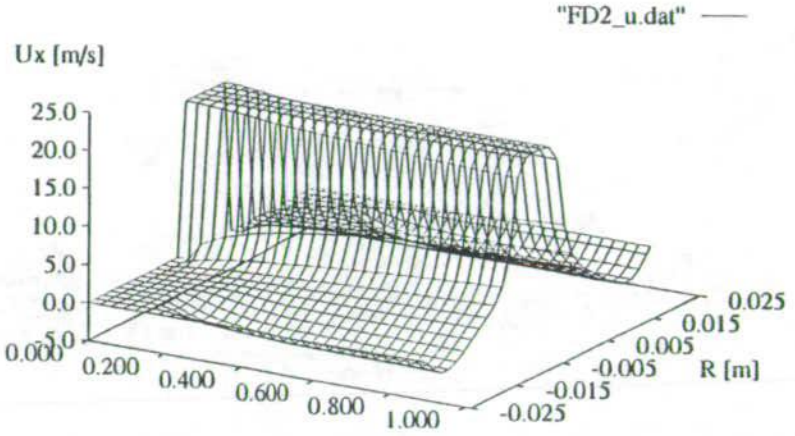

(a) Axial Velocity

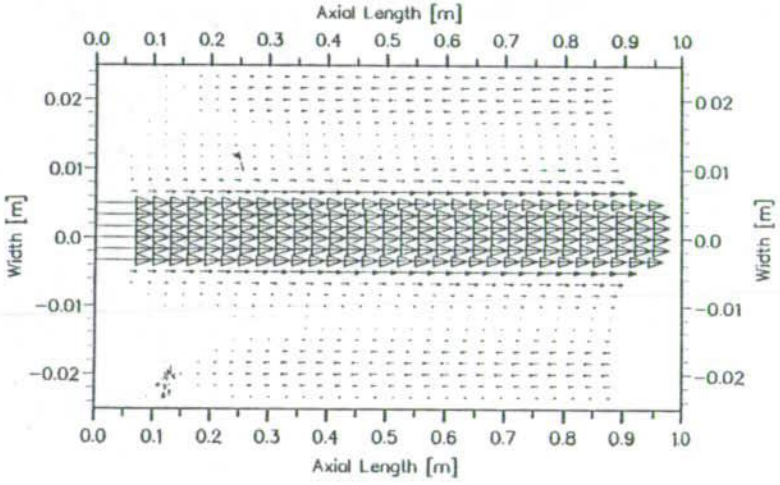

(b) Velocity Vectors

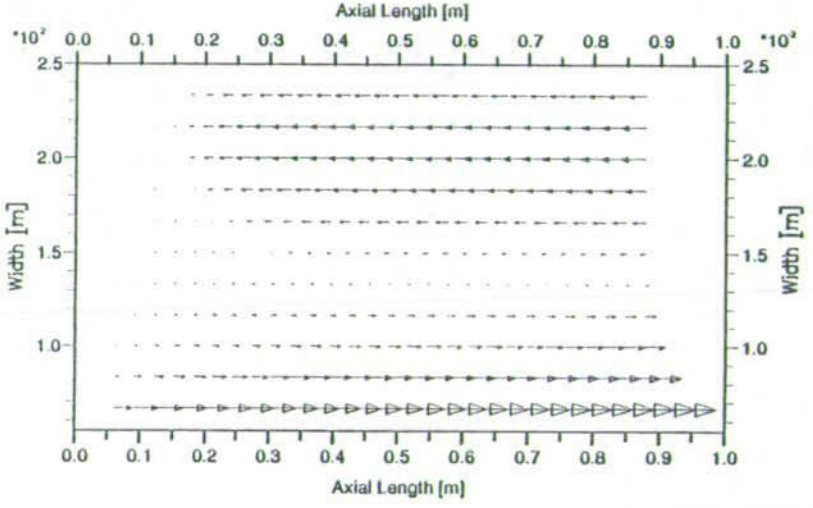

(c) Zoom Outside Core

Figure 3.4: 20 m/s Jet into 50 mm Diameter Stagnant Air Region

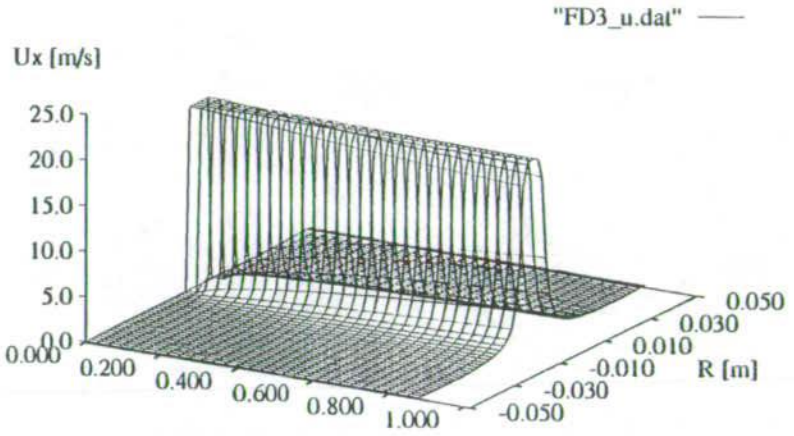

(a) Axial Velocity

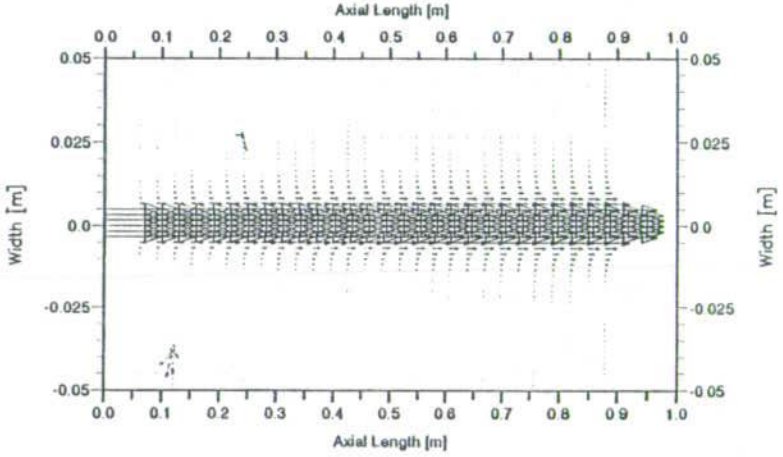

(b) Velocity Vectors

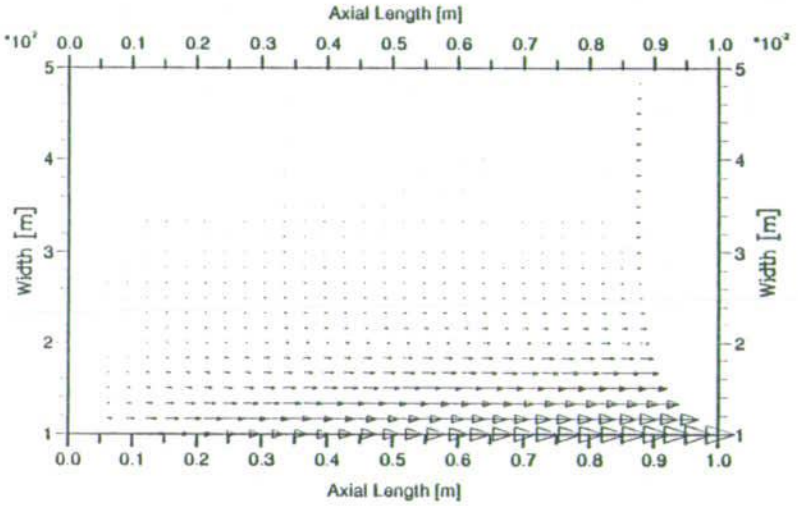

(c) Zoom Outside Core

Figure 3.5: 20 m/s Jet into 100 mm Diameter Stagnant Air Region

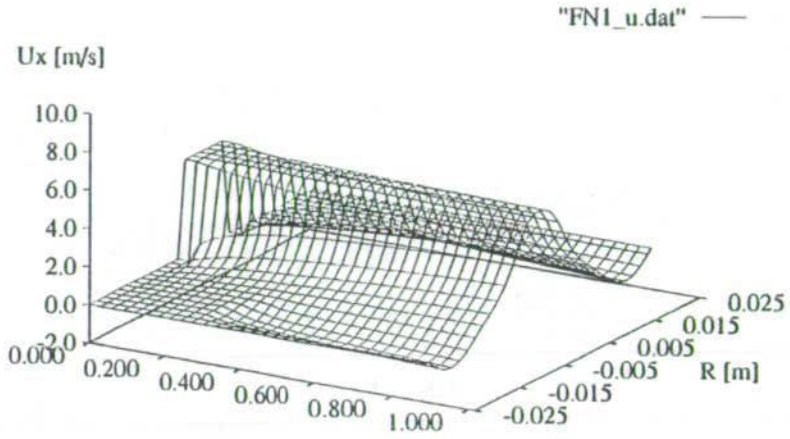

(a) Axial Velocity

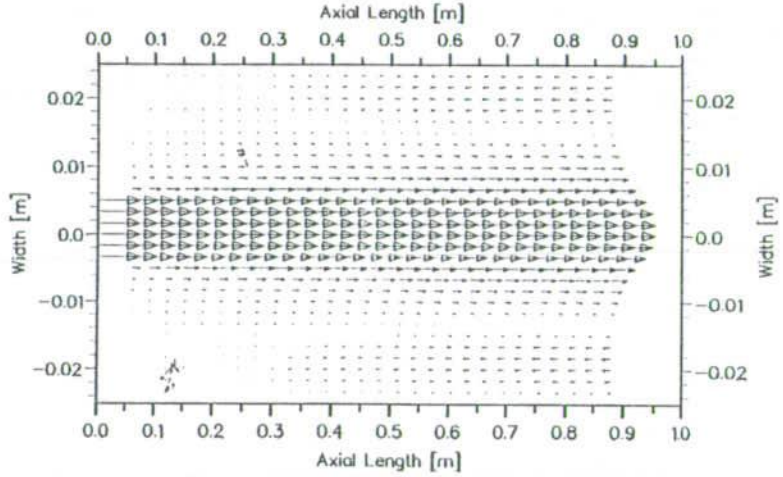

(b) Velocity Vectors

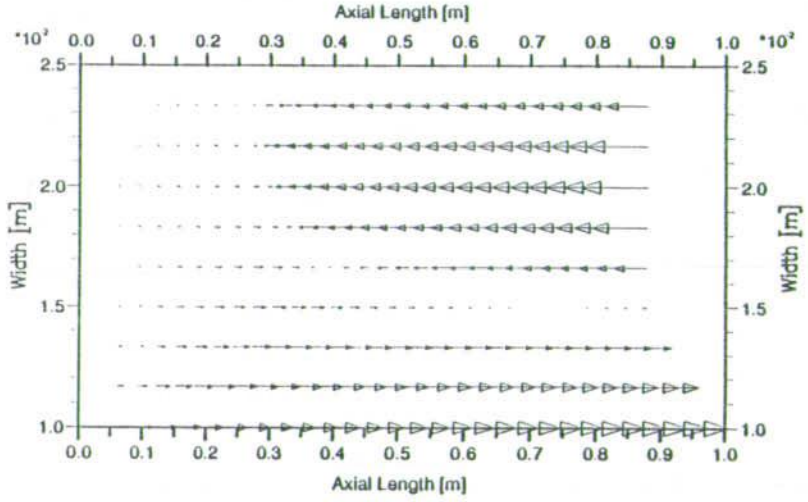

(c) Zoom Outside Core

Figure 3.6: 5 m/s Jet into 50 mm Diameter Stagnant Air Region

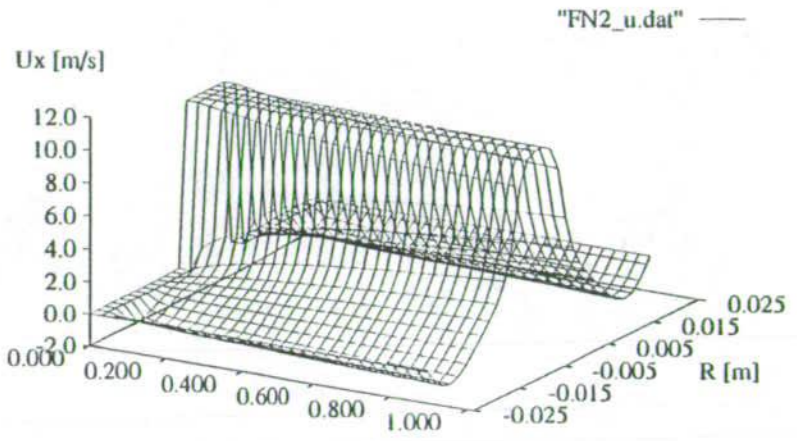

(a) Axial Velocity

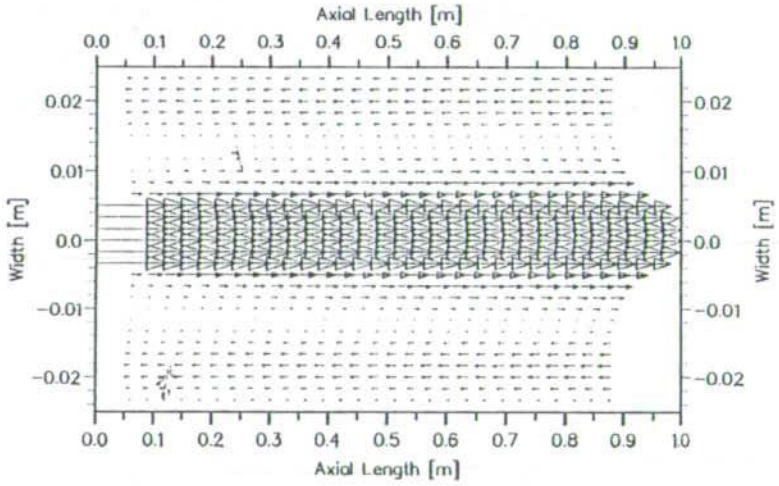

(b) Velocity Vectors

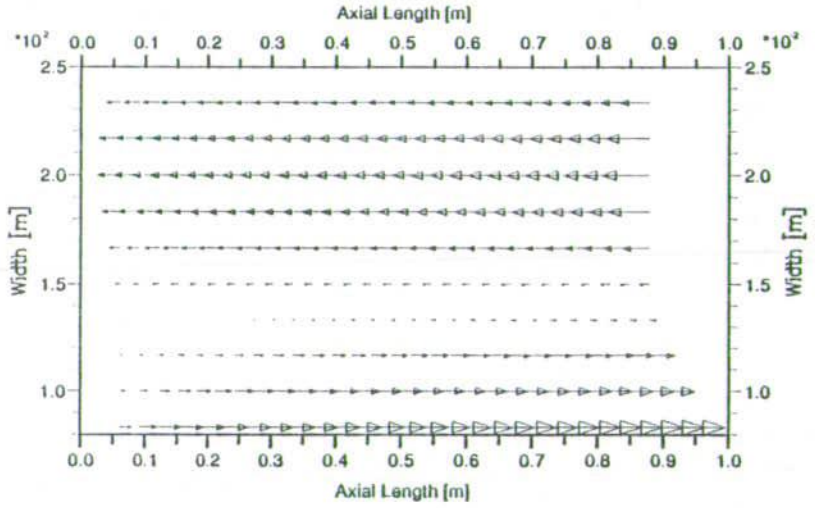

(c) Zoom Outside Core

Figure 3.7: 20 m/s Jet into 50 mm Diameter Stagnant Air Region

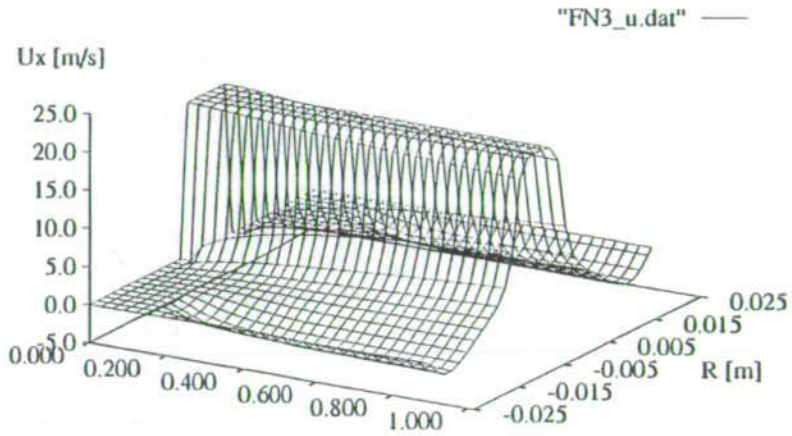

(a) Axial Velocity

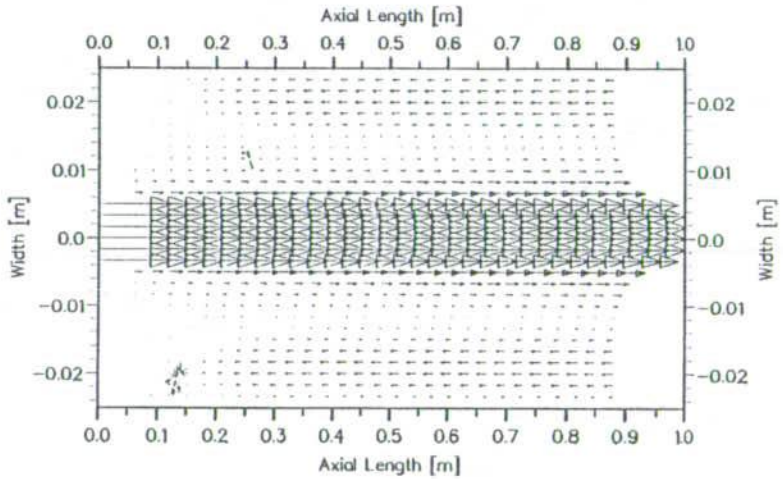

(b) Velocity Vectors

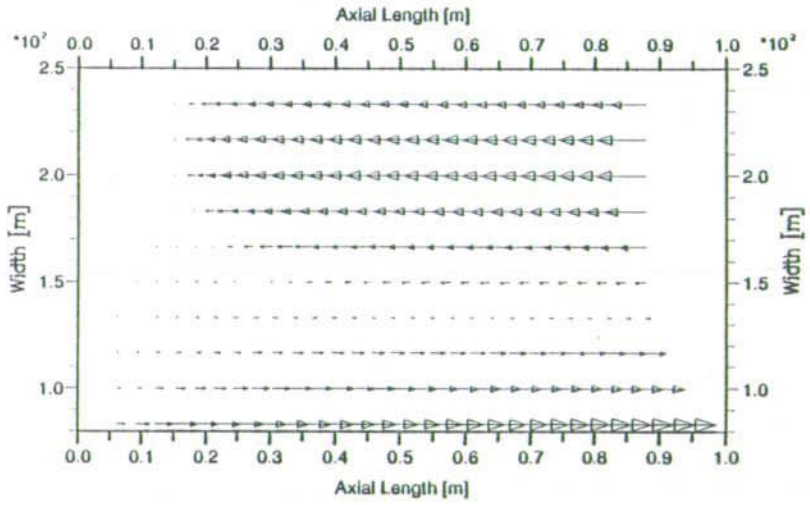

(c) Zoom Outside Core

Figure 3.8: 26.6 m/s Jet into 50 mm Diameter Stagnant Air Region

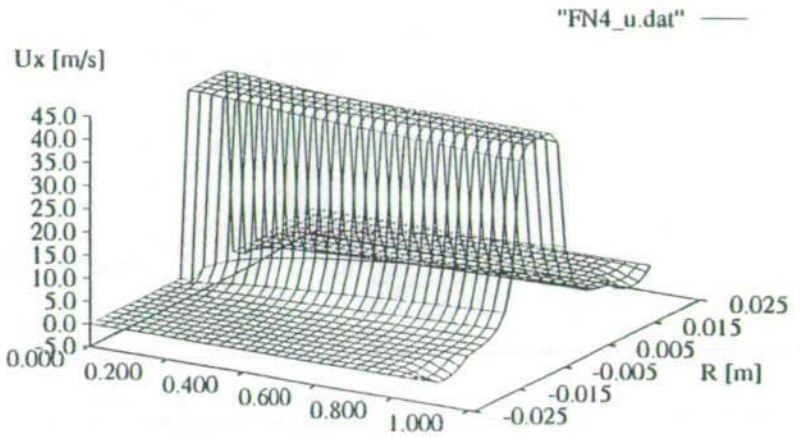

(a) Axial Velocity

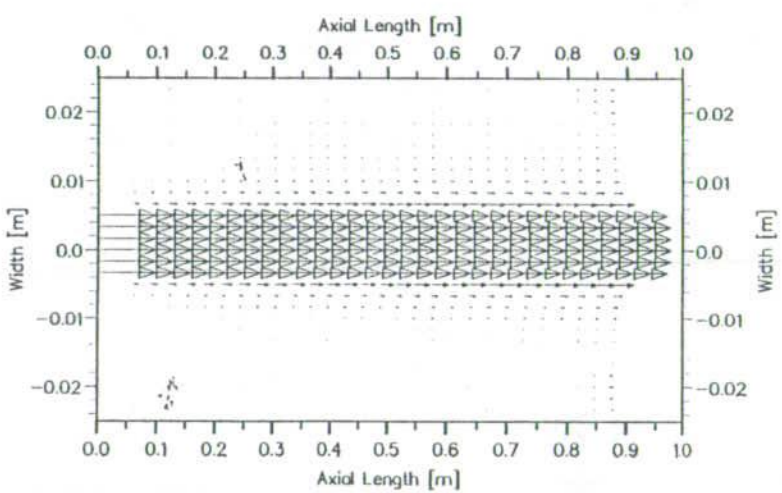

(b) Velocity Vectors

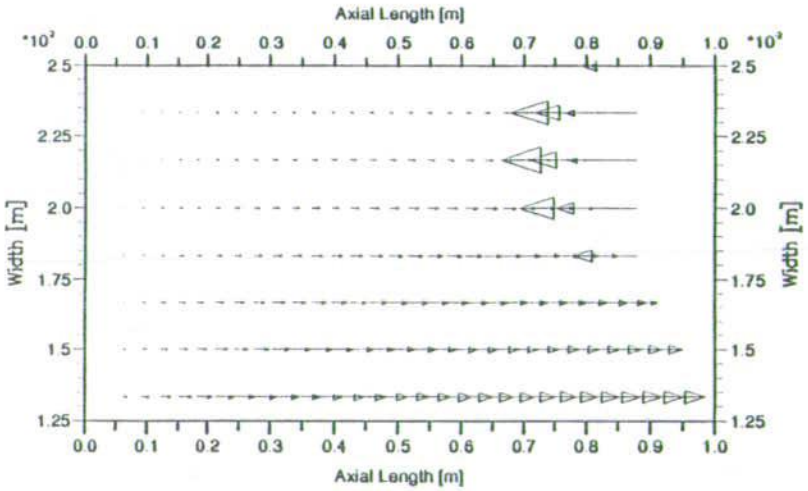

(c) Zoom Outside Core

Figure 3.9: 40 m/s Jet into 50 mm Diameter Stagnant Air Region

3.3.2 Mixing

In simulating mixing of to co-axial jets, a 10 mm diameter core jet issuing at 20 m/s was mixed with annular flow of between 13 m/s and 30 m/s giving the velocity ratio (core/annular) of 0.67 to 1.5. The geometry/inlet condition for this simulation is shown in figure 3.10.

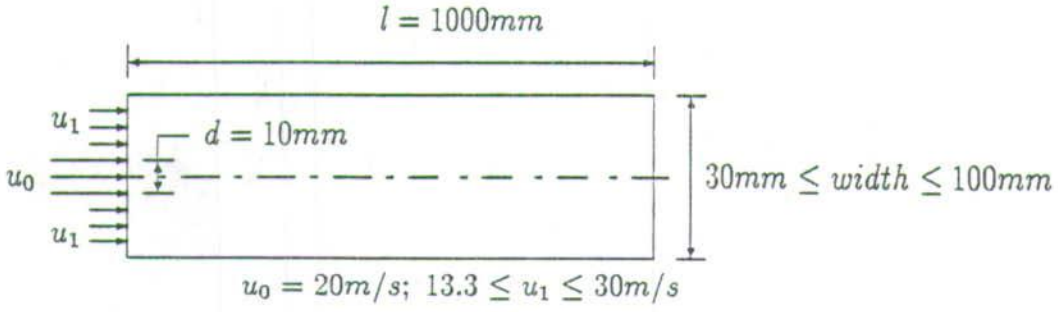

Figure 3.10: Inlet Conditions For Two Jet Mixing

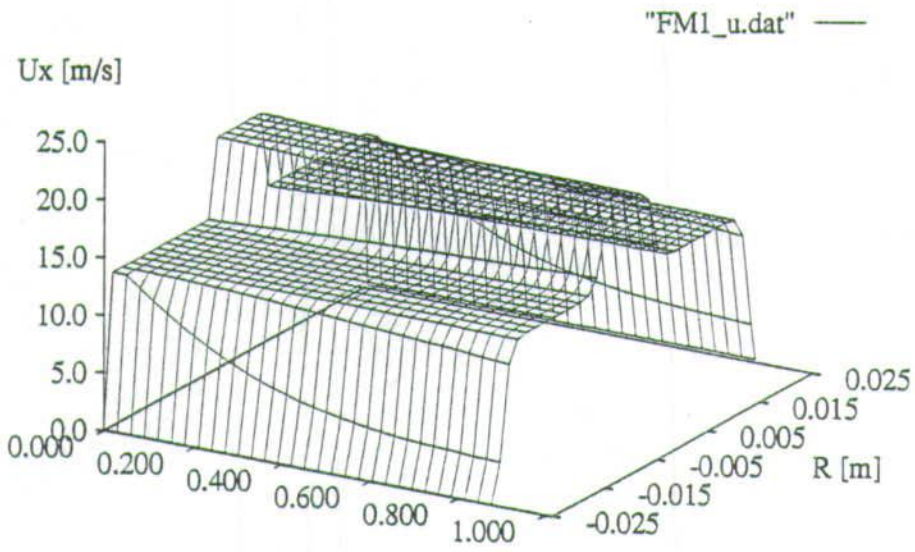

(a) Axial Velocity

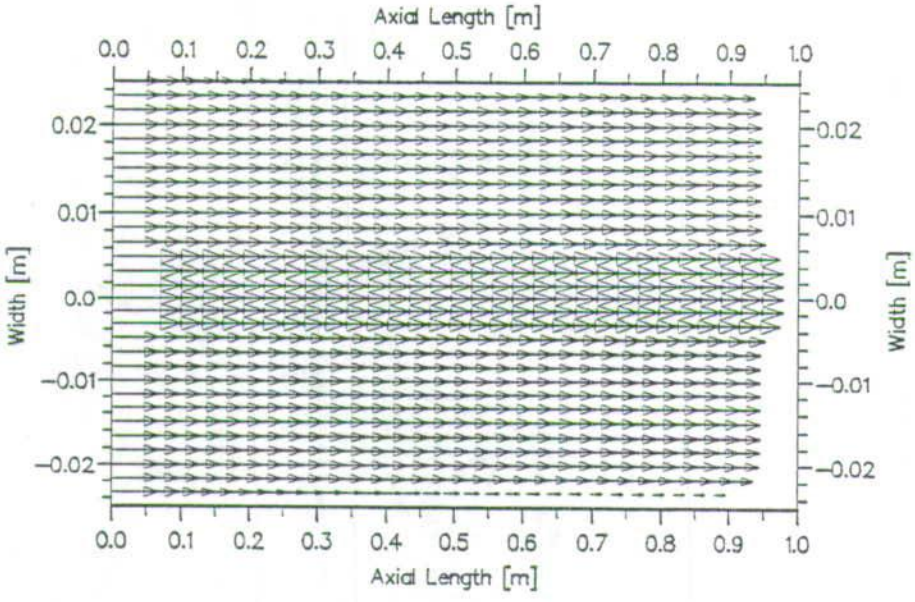

(b) Velocity Vectors

Figure 3.11: Velocity ratio, $\frac{u_1}{u_0} = 0.67$ ($u_0 = 20m/s$; $u_1 = 13.3m/s$)

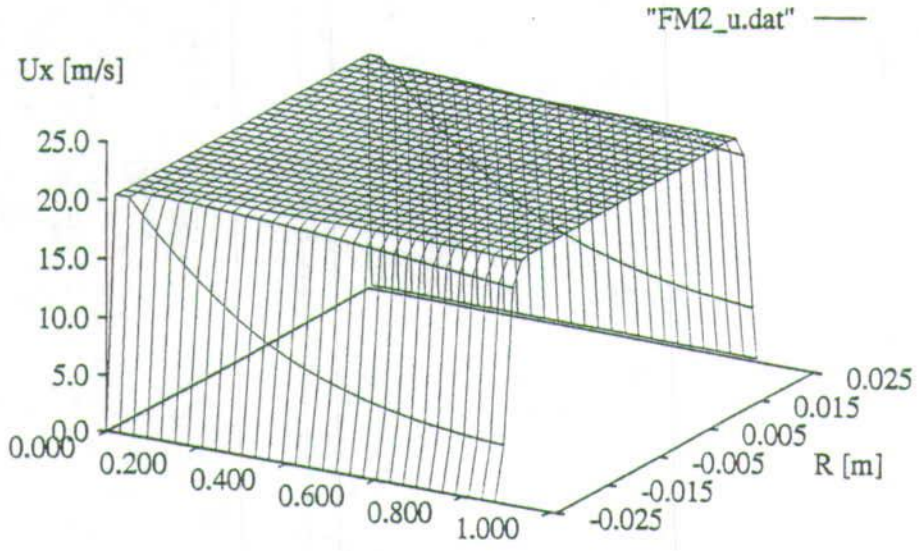

(a) Axial Velocity

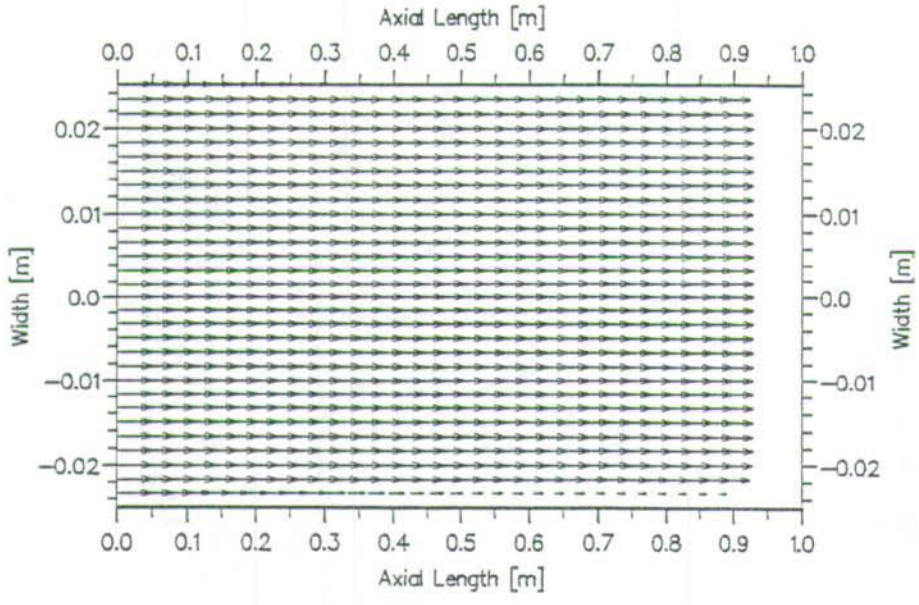

(b) Velocity Vectors

Figure 3.12: Velocity ratio, $\frac{u_1}{u_0} = 1.0$ ($u_0 = 20m/s$; $u_1 = 20m/s$)

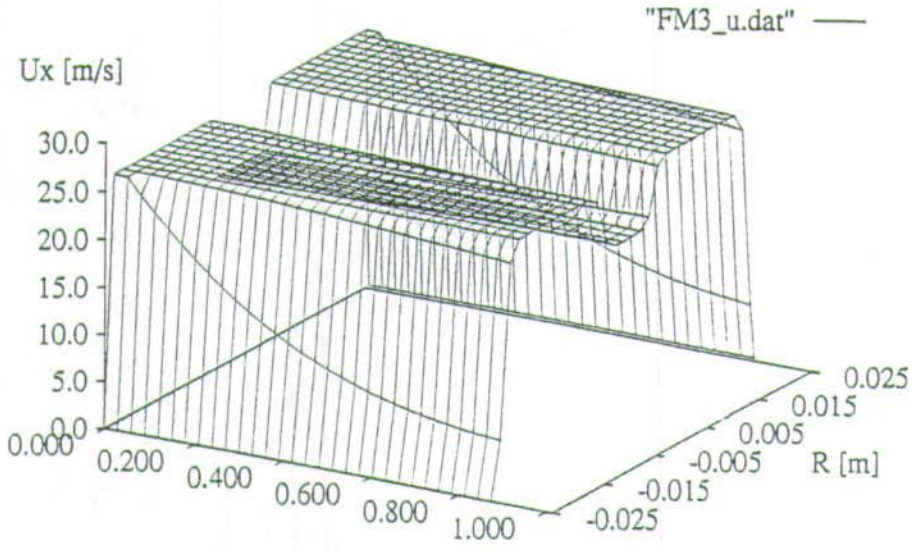

(a) Axial Velocity

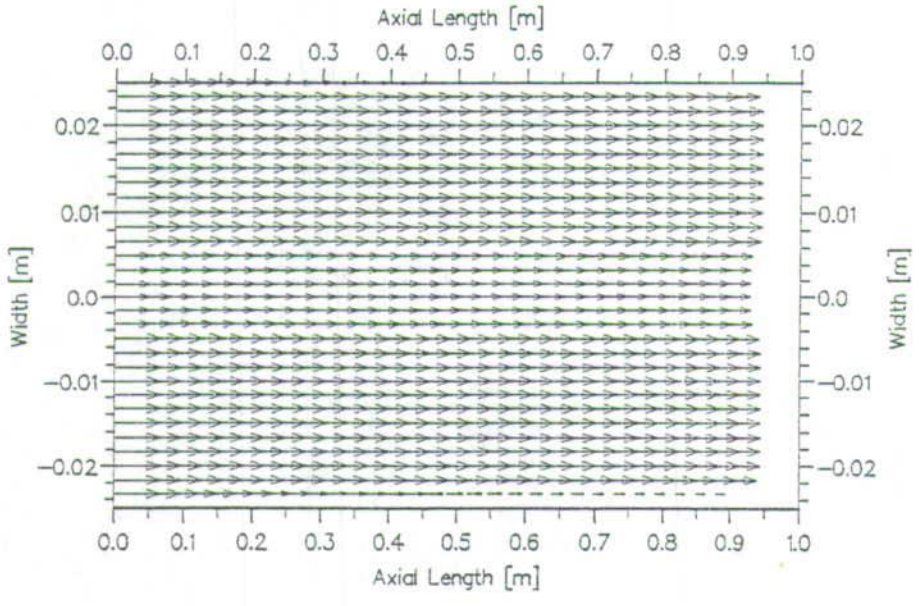

(b) Velocity Vectors

Figure 3.13: Velocity ratio, $\frac{u_1}{u_0} = 1.3$ ($u_0 = 20m/s$; $u_1 = 26.6m/s$)

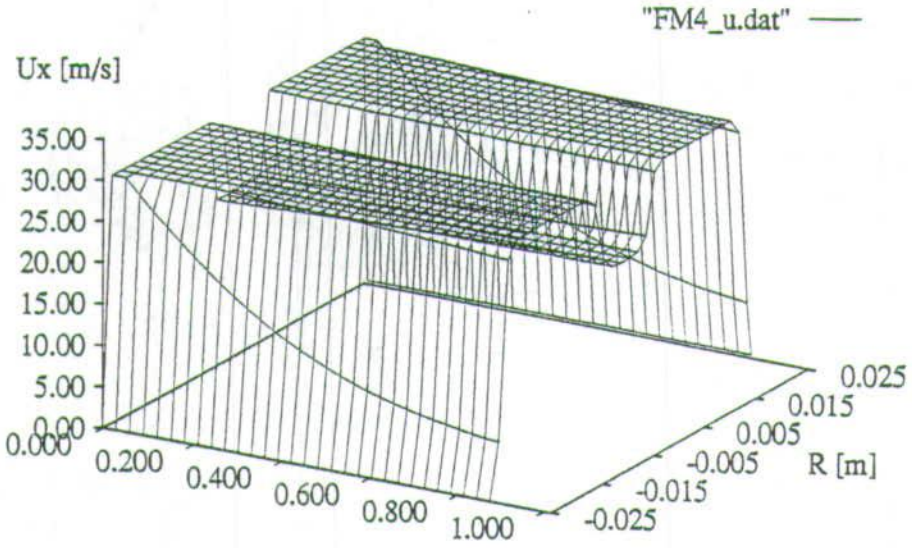

(a) Axial Velocity

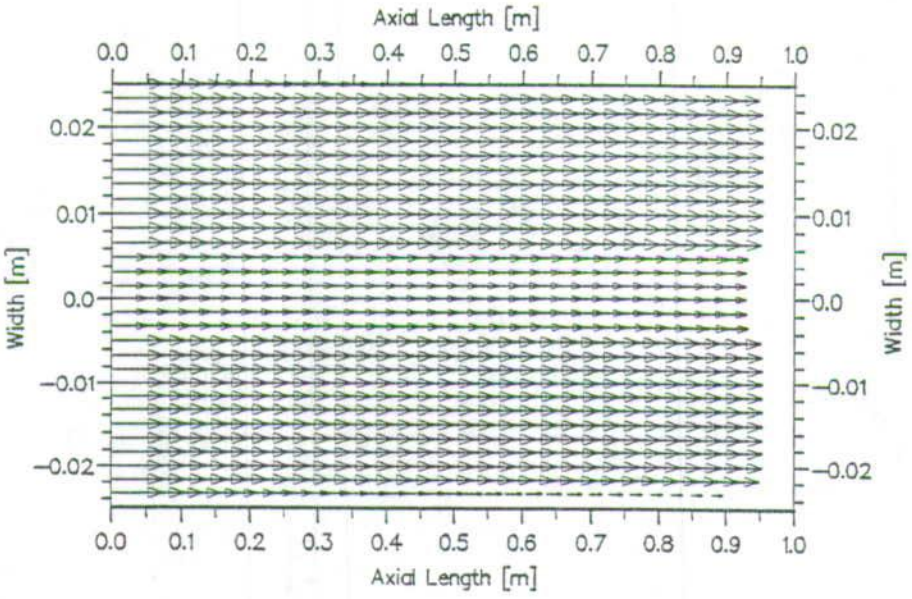

(b) Velocity Vectors

Figure 3.14: Velocity ratio, $\frac{u_1}{u_0} = 1.5$ ($u_0 = 20m/s$; $u_1 = 30m/s$)

3.4 Simulation of Particle Injection

FLUENT provide features for simulating particle injection/tracking under the following assumptions:

- The gas phase is not influenced by the particle phase.
- Particle trajectories calculated based on the initial gas phase solution (in accordance with the above assumption).
- Particle volume not taken into account in the solution of the continuous phase equations. i.e. the volume of the computational cell is not adjusted for the presence of particles.
- No particle-particle interaction forces, i.e. each particle is independent (except which may influence the continuous phase e.g. in high particle volume loading), and that particles do not collide.
- Particles injection volumes restricted to less than 10%

Although this particle injection/tracking simulating features were tried, only few simulation runs are presented here because the features seemed to be too limited in scope.

Indeed some of the assumptions above, [67] and [41] report experimental results on the reduction or increase of the turbulence intensity caused by the presence of a dispersed phase in a fluid [119], [67] and [41]. A good analytical consideration can be found in [51]. All conclude that small particles reduce the turbulence intensity of the flow, while larger particles increase it.

There are several possible mechanisms, which are not independent of each other, that can contribute to the turbulence modification in dispersed two-phase systems:

1. Dissipation of turbulent kinetic energy by the particles.
2. Increase of the apparent viscosity due to the presence of particles.
3. Shedding of vortices or the presence of wakes behind the particles.
4. Fluid moving with the particle as added fluid mass to the particle.
5. Enhancement of the velocity gradients between two rigid particles.
6. Deformation of the dispersed phase.

Of these mechanisms, (6) is not applicable to particulate flows and the contributions of (5) and (2) are negligible in dilute particle dispersions. But predominant mechanisms for the enhancement and production of turbulence are:

- the dissipation of power from an eddy for an acceleration of a particle (turbulence reduction)
- the flow velocity disturbance due to the wake of the particle or the vortices shed, which is taken as predominant mechanism for turbulence enhancement.

These facts, make the particle injection/tracking simulating feature weak.

Two sets of Particle injection simulation reported here. In the first set, the inlet fluid velocity and that of the particle jet was fixed at 20 m/s, and particle

loading varied from 0.05 to 0.2 (figures 3.15 to 3.17). In the second set, the particle loading was fixed at 0.1, and the injection velocity varied from 5m/s to 30m/s (figures 3.18 to 3.20). Particle loading is the mass ratio of particles to air.

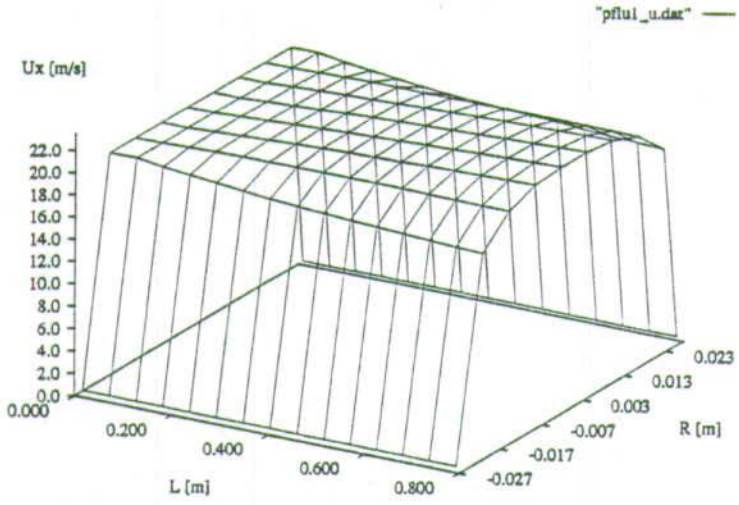

(a) Axial Velocity

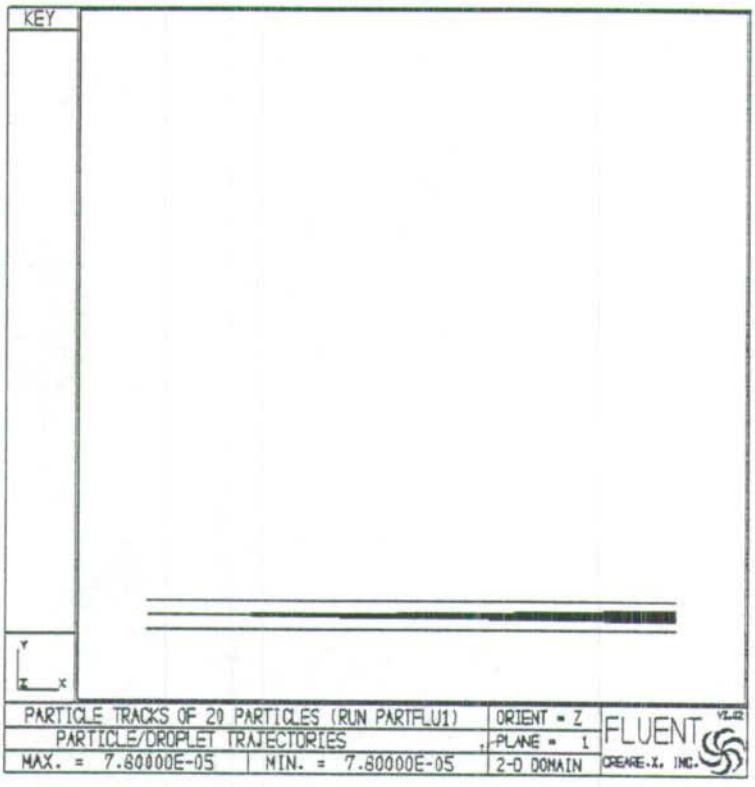

(b) Particle Tracks

Figure 3.15: Fluid & Particle Inlet Velocity = 20 m/s (Particle : Air Mass Ratio = 0.05)

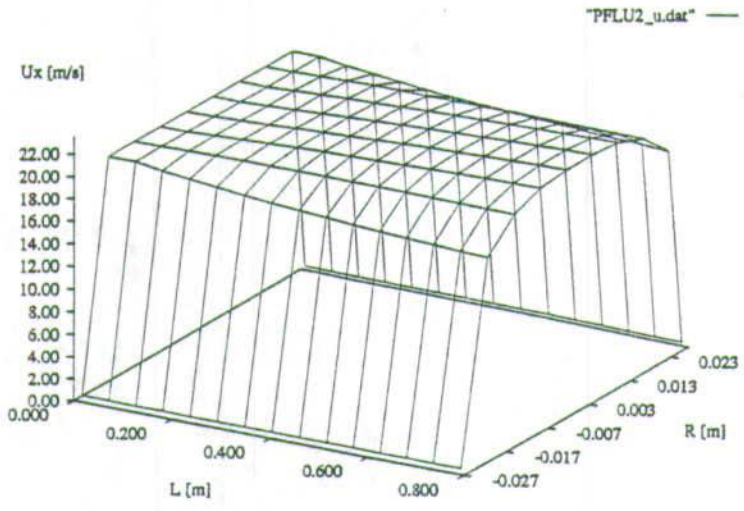

(a) Axial Velocity

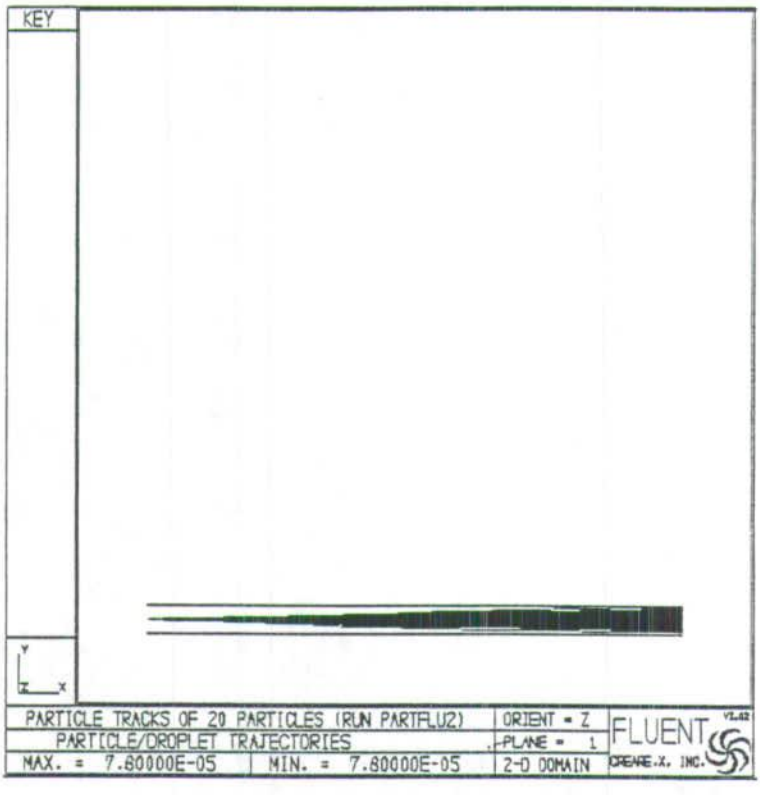

(b) Particle Tracks

Figure 3.16: Fluid & Particle Inlet Velocity = 20 m/s (Particle : Air Mass Ratio = 0.1)

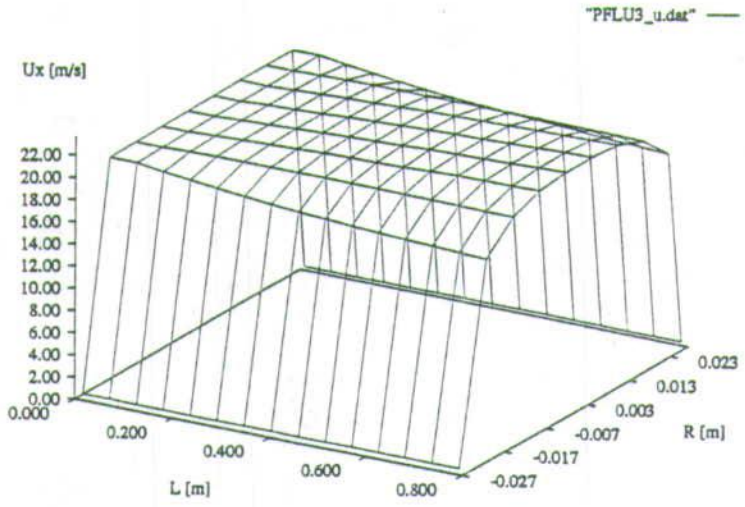

(a) Axial Velocity

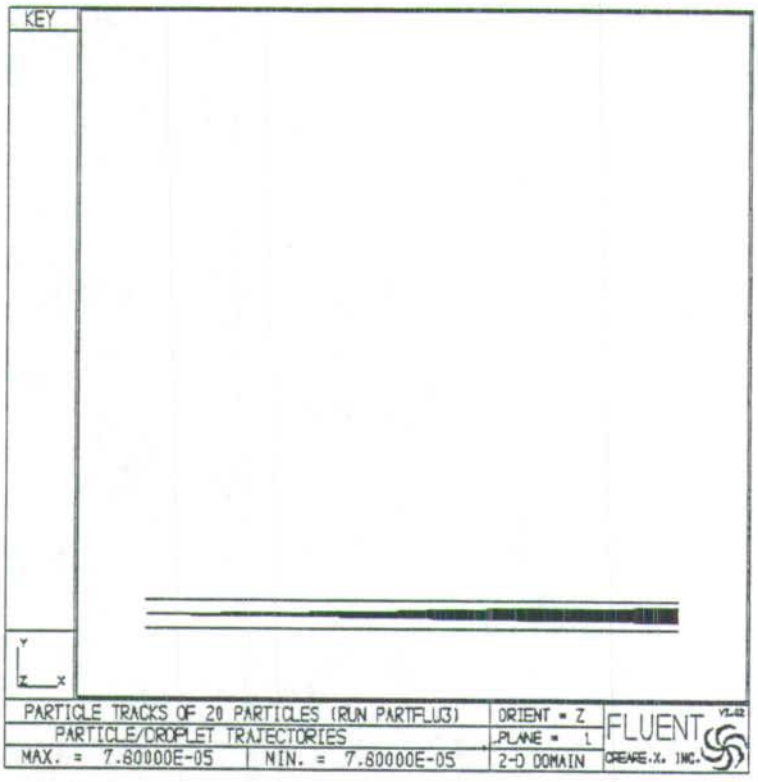

(b) Particle Tracks

Figure 3.17: Fluid & Particle Inlet Velocity = 20 m/s (Particle : Air Mass Ratio = 0.2)

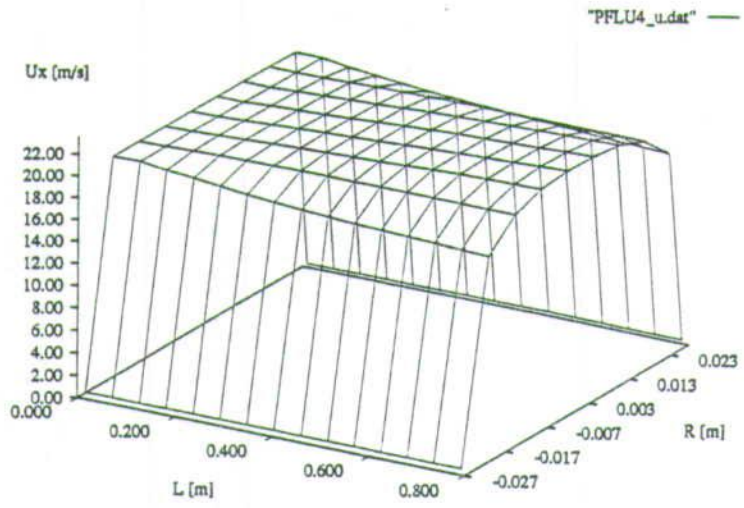

(a) Axial Velocity

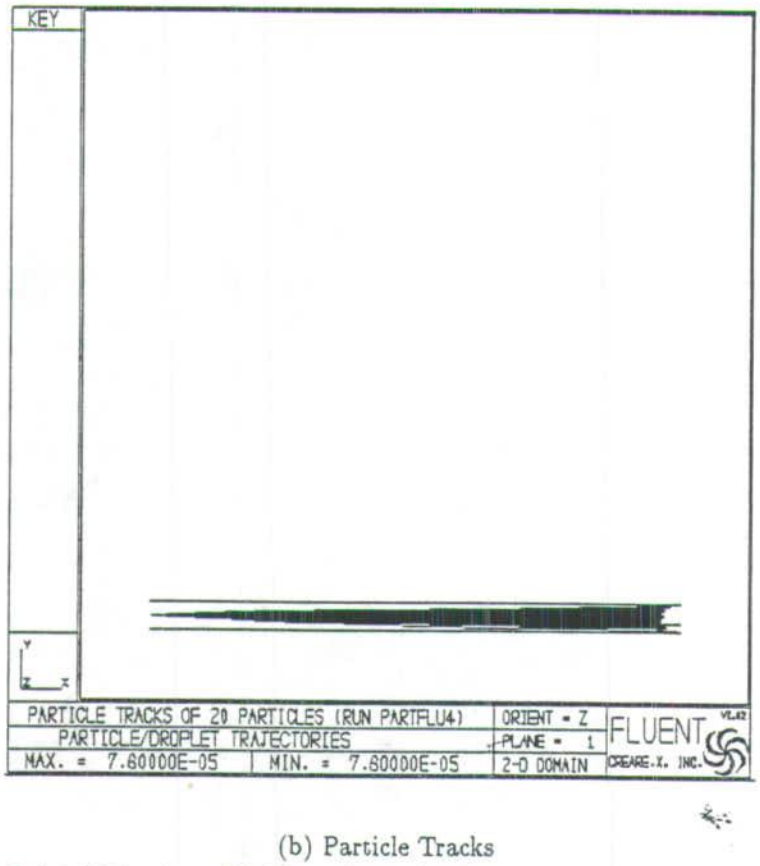

(b) Particle Tracks

Figure 3.18: Inlet Velocity: Fluid = 20 m/s; Particle = 10 m/s (Particle : Air Mass Ratio = 0.1)

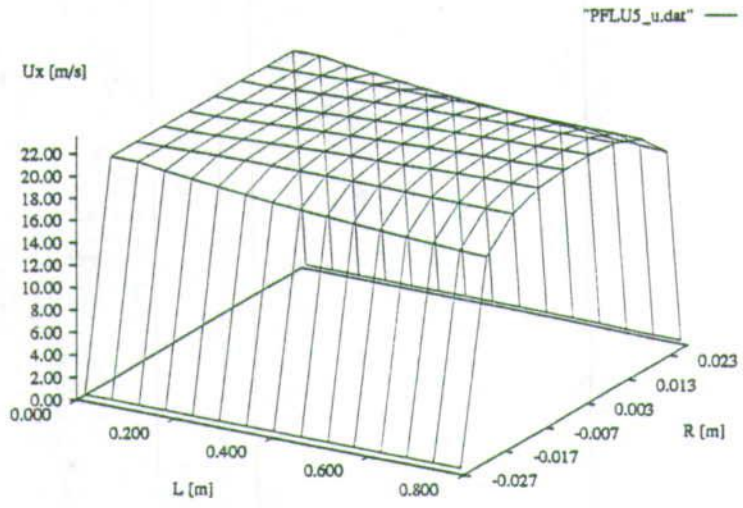

(a) Axial Velocity

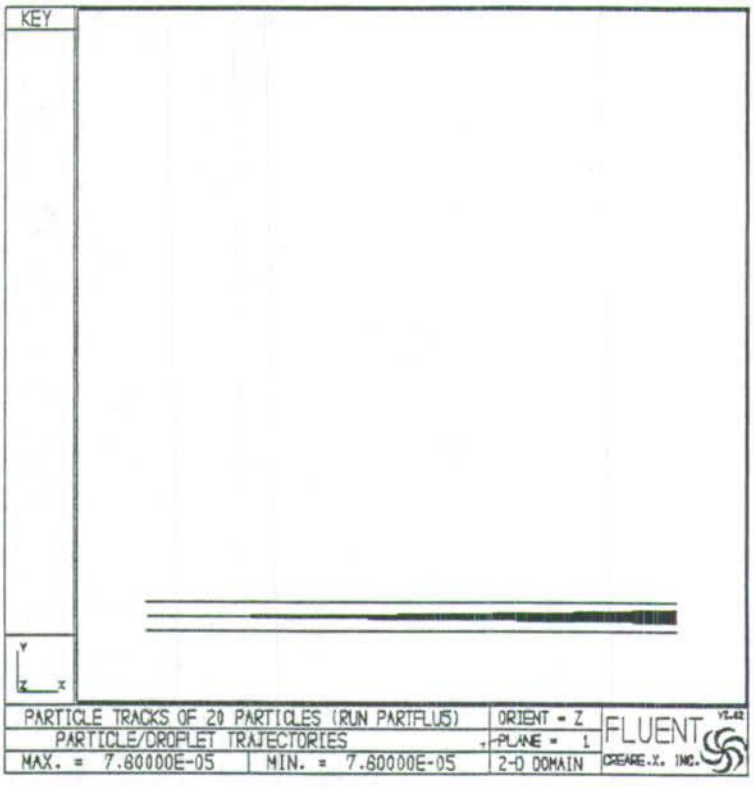

(b) Particle Tracks

Figure 3.19: Inlet Velocity: Fluid = 20 m/s; Particle = 30 m/s (Particle : Air Mass Ratio = 0.1)

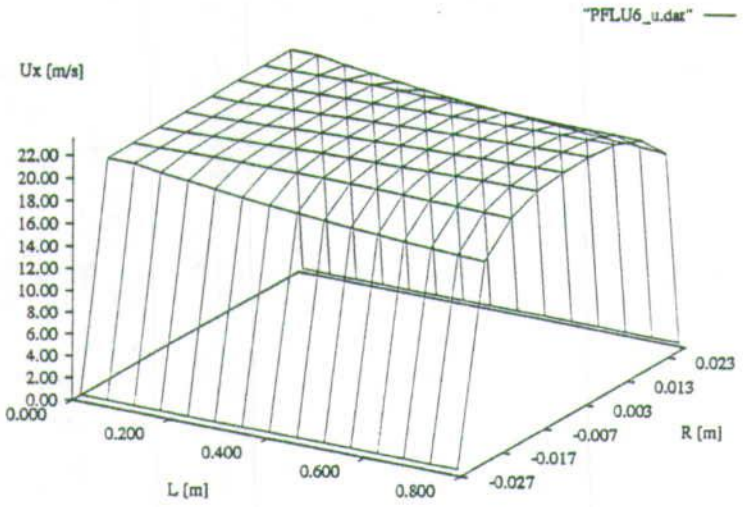

(a) Axial Velocity

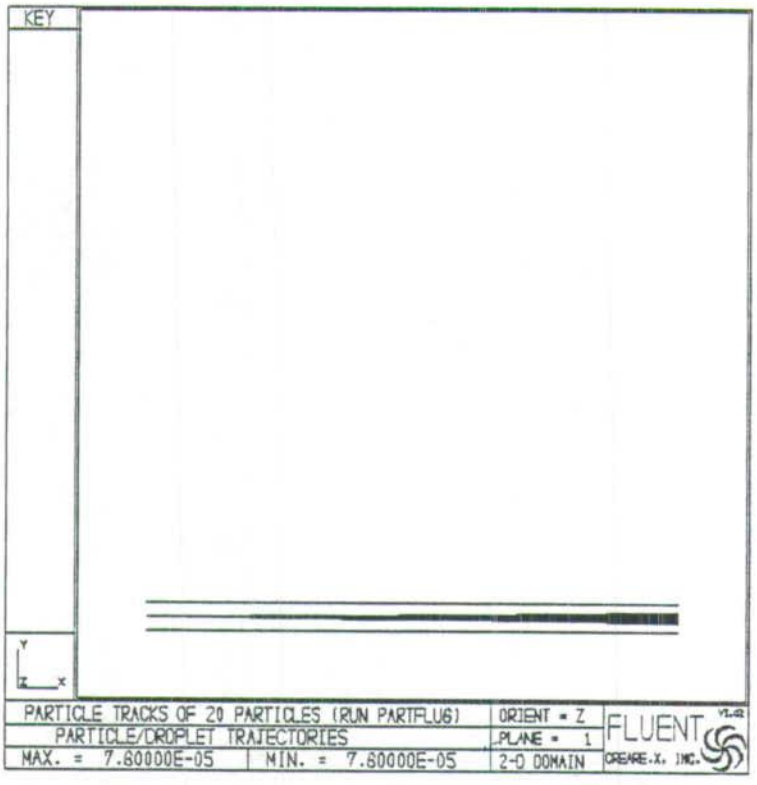

(b) Particle Tracks

Figure 3.20: Inlet Velocity: Fluid = 20 m/s; Particle = 5 m/s (Particle : Air Mass Ratio = 0.1)

3.5 Comments on Simulation Results

3.5.1 Comments on Air Jet into Stagnant Air Simulation Results

The single phase simulation results, are considered to be in good agreement with theory. In cases of jets issuing into a stagnant air region, there is evidence, as expected, of development of rverse flow . This can be explained by the fact that the turbulent mixing layer seems to be thickened simply because non-turbulent fluid particles are forced by clusters of discrete vortices or large eddies to have their normal (towards the wall) velocity.

The presence of the containing outer annulus (wall) ensured that any enhanced mixing would reflect also in substantial pressure variations. It is evident that, enhanced radial mixing is created as a result of the instability, which itself is present because of the outwardly decreasing momentum of the fluid. Thus, the development of reverse flow is more pronounced in narrow flow section than is in wider one see figures 3.3 to 3.5. It is important to note that this whole process is strongly interactive.

3.5.2 Comments on Mixing Simulation Results

In the mixing cases, it seems the faster of the two streams seems to transfer momentum to the slower via turbulent mixing. Any diffusion of the faster stream, however, introduces an adverse pressure gradient that tends to separate the slower stream. This *competition* between turbulent momentum transfer, It is

believed that this imposes pressure gradients, which in turn would contribute to the momentum reduction. The whole feature of momentum reduction is further complicated by the addition/development of reverse flow.

The transfer of momentum to the slower stream via turbulent mixing, and the diffusion of the faster stream, is thus more apparent in the case of a jet flowing into a stagnant region than in the mixing case. Thus, a faster jet would start to spread, develop swirling or reverse flow further down stream than slower jets. It is probably for this fact, that there are seems to be no apparent development of any reverse flow in the mixing case, figures 3.6 to 3.9, also figures 3.11 to 3.14.

3.5.3 Comments on Particle Injection Simulation Results

In all the particle injection simulation runs, one general trend is observed, of particles escaping, i.e.. go though the pipe exit. This is what would be expected. The particle dispersion, shown by plotting tracks of 20 particles, however, does not give a consistent picture. For a given jet velocity, the higher the air-particle loading, of the jet, the less the jet disperses, see also [84], comparison of figures 3.15, 3.16 and 3.17, shows that the jet at 0.1 (figure 3.16) loading spreads more than that of 0.05 loading (figure 3.15), although that of 0.2 loading (figure 3.17) does not spread more than that of 0.1 loading, it still shows significant more spread than that of 0.05 loading.

The second set of results do not give a consistent picture either. For a given relative velocity ratio between the jet and the background airflow, the higher the background airflow velocity, the more the jet disperses, see also [84]. One

would have expected the 5 m/s jet with 20 m/s background velocity (figure 3.16) to spread significantly more than jet of 10 m/s, 20 m/s and 30 m/s with same background air velocity figures 3.18, 3.19 and 3.20 respectively. The axial velocity surface plots still appear to be similar in all six plots. Results of all particle injection simulation runs, figures 3.15 to 3.20 thus do not seem to give any good general pattern.

There are other general explanations as to why FLUENT simulation results differ from reported in literature, these include:

- Square flow geometry was used in all the simulation runs, results based on this square geometry would definitely differ from those based on circular geometry.

- The inlet velocity distribution was set to be of equal magnitude. In reality, the velocity distribution form can be approximated to that of a parabola with a maximum velocity at the center of the pipe and zero velocity at the boundaries (pipe wall). This unrealistic velocity distribution might have considerable effect on the simulation results as it sets up a non realistic flow pattern at the inlet. Although it is possible in FLUENT to define a parabolic developed flow distribution at the inlet, this definition however demands a large number of grid cells. To account for the limits of number of cells described on page 3.2 and to maintain the same aspect ratio would have required a use of number of cells that required a large computer memory that the workstation in use at the time could not provide. Thus the uniform velocity distribution at inlet was used as a consequence of computer memory limitations only.

- The fluid, for simplicity reasons only, was considered to be incompressible,

and as such, the increase of velocity as a result of pressure loss along the flow section was not accounted for in this simulation, and must thus also be contributing to the divergence of this simulation results from those reported in the literature.

Chapter 4

Experimental Rig Design

The experimental rig employs a positive displacement fan driven by a 30 kW motor to deliver both primary and secondary air to a 4 inch glass test/measuring section. In this rig design, the same fan is used to provide the primary air (whose velocity is being measured), and also to pick-up the particles from the particle feed hopper and deliver them in the test section. Other pieces of equipment used on the rig included a gas cyclone for recovering particles, the laser equipment and the related optics, the seeding system and particle injection system. Figure 4.4 shows the rig layout. Most parts of this equipment were designed and fabricated in the departmental workshop, while others had to be specified and ordered from outside suppliers. This chapter discusses the design of the swirl generator, the flow straightener, general ducting and the gas cyclone. The design of the gas cyclone which is based on standard design procedures is reported in appendix B.

4.1 Swirl Generator

Guide vanes will be used to generate the wide range of swirl levels required. For an axial guide vane, if the vanes are thin and of constant chord angle, and if the axial velocity distribution in the pipe is uniform, then, the theoretical swirl numbers can be approximated by the following procedures [82], see also [1] and [12]:

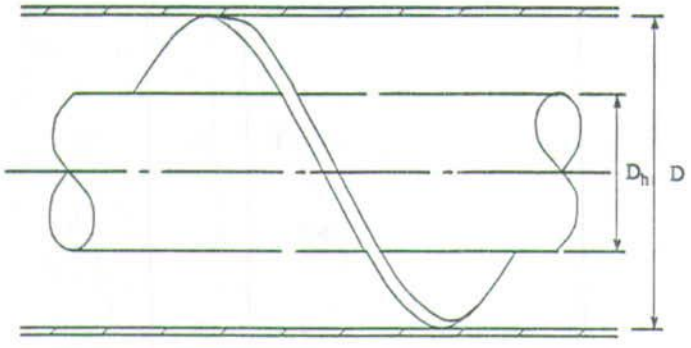

Figure 4.1: Sketch Of Swirl Vane

The linear momentum, G_x:

$$G_x = \int_{R_h}^{R} u\rho u\pi r dr + \int_{R_h}^{R} P2\pi\rho r dr \approx u_0^2\pi(R^2 - R_h^2) \tag{4.1}$$

The angular momentum, G_ω:

$$G_\omega = \int_{R_h}^{R} (u_\omega r)u\rho\pi r dr + \int_{R_h}^{R} P2\pi\rho r dr \approx \frac{2}{3}\pi\rho u_0^2 tan\alpha(R^3 - R_h^3) \tag{4.2}$$

Note that in both cases, the static pressure, $\int_{R_h}^{R} P2\pi\rho r dr$, has been neglected.

The swirl number, S is:

$$S = \frac{G_\omega}{G_x R} = \frac{\frac{2}{3}\pi\rho u_0^2 tan\alpha(R^3 - R_h^3)}{u_0^2\pi(R^2 - R_h^2)R} = \frac{2}{3}tan\alpha\frac{1-r^3}{1-r^2} \tag{4.3}$$

where r is the ratio of hub radius to nozzle outlet radius $\frac{R_h}{R}$.

To achieve reasonable blade overlap, 8 vanes made of 8 flat blades could be be used. These would be held on a hub which must be big enough to both accommodate the rope injecting tube ($\approx$ 5 mm diameter) and provide a range for varying the radial position of the injected rope. A hub diameter of $D_h = 50.8mm$ was used, with a test section size $D = 101mm$ gives a radius ratio, r = $\frac{0.0254}{0.0508} = 0.5$.

For ease of manufacturing, these vanes were approximated by helical blades cut along the hub (giving a tangent vector of constant angle α) [113]. By varying this angle α (determines the pitch of the resulting screw) blades capable of producing the different swirl levels required could be made. Four of these were made at angles 15°, 30°, 45° and 60°. See figure 4.2.

Table 4.1: Theoretical Swirl Numbers

Vane Angle	15	30	45	60
Swirl No.	0.21	0.45	0.78	1.35

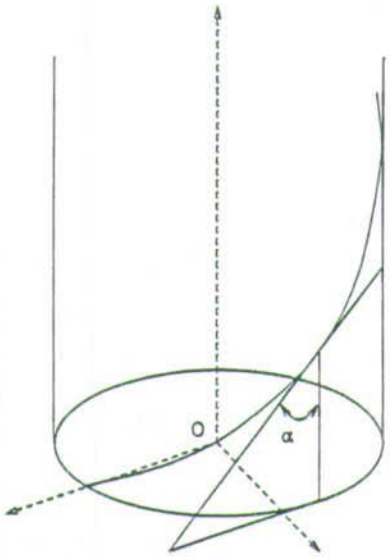

Figure 4.2: Sketch Of Helix Vane

4.1.1 Swirl Generator Pressure Drop

The friction loss for flow through a swirl generator with axial vanes, i.e. 0° vane angle, may be given by:

$$h_{f1} = k_1 \frac{\rho u_o^2}{2g} \tag{4.4}$$

For vanes at an angle α, an additional pressure head is required to increase the velocity from u_o to $u_o/cos\alpha$, this additional pressure head is:

$$h_{f2} = k_2 \frac{\rho u_o^2}{2g}\left(\frac{u_o^2}{cos^2\alpha} - u_o^2\right) = k_2 \frac{\rho u_o^2 tan^2\alpha}{2g} \tag{4.5}$$

k_1 and k_2 depends on surface roughness, wetted area, and the obstruction due to

the thickness of the vanes.

Thus the total friction loss (in mbar) is:

$$\Delta P_{swirl} = \frac{\rho u_o^2}{2}(k_1 + k_2 tan^2\alpha) \tag{4.6}$$

k_1 is negligible for $\alpha < 45°$, and k_2 is approximately unity. Empirical values for k_1 and k_2 quoted are larger than theoretical ones, therefore empirical pressure drops will be higher than theoretical ones. Empirical pressure drop data is tabulated in table 4.2.

Table 4.2: Swirl Generator Pressure Drop

Vane Angle	k_1 Ref [82]	k_2 Ref [82]	ΔP_s Eqn[4.6] mbar
15	0.83	1.3	8.9
30	0.83	2.9	17.2
45	0.83	3.4	40.6
60	0.83	3.9	120.3

4.2 Flow Straighteners

Flow straighteners and the wind tunnel section were installed upstream of the swirl generator in order to reduce inlet turbulence levels. They also ensured that any swirl levels induced by the swirl generator would be generated from the same background turbulence level.

Two flow straighteners, one before the wind tunnel type expansion and the other before the wind tunnel type contraction sections were used. The wind tunnel expansion and contraction sections profiles (see figure 4.3) were designed according to the following formula [42]:

$$r = \frac{r_0}{\sqrt{1 - [1 - (\frac{r_0}{r_1})^2]\frac{(1 - 3x^2/a^2)^2}{(1 + 3x^2/a^2)^3}}} \tag{4.7}$$

Where x is the position along the wind tunnel axial axis, a is the radius varying from 0 to r, $r_0 = 0.5d_0$ and $r_1 = 0.5d_1$ (see figure 4.3). Usually parameter a is taken to be $4r_0$. Also when $x = a/\sqrt{3}$, $r = r_0$. The length L_1 is recommended to be 1.5 to 2.5 times the inlet diameter of the contraction section (d_1). The section designed was of the following dimensions ($r_0 = 50.8$mm; $r_1 = 76.20$mm; $L_1 = 530$mm; $L_2 = 245$mm).

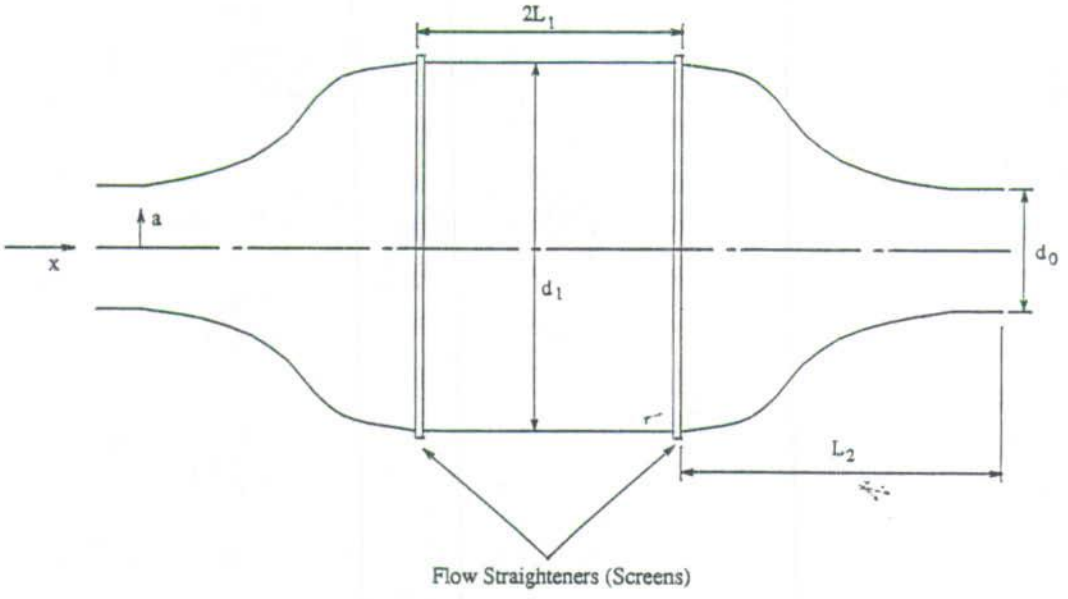

Figure 4.3: Flow Straighteners' Positions

4.3 Fan

This is for providing primary and secondary air to the test/measuring section. The fan must be capable of overcoming the pressure drop in the cyclone and duct work (screens, valves, bends etc.).

The pressure drop along the duct is mainly due to the friction loss along the duct length and velocity head loss at bends. These losses can be estimated from (see [19, pages 201 - 202] for friction loss guidelines), see also figure 4.4:

- Four 90° bend, total resistance coefficient $\approx 0.9 \times 4 = 3.6$
- One standard tee piece: total resistance coefficient ≈ 1.8
- One enlargement, diameter ratio = 0.667, total resistance coefficient ≈ 0.3
- Contraction, diameter ratio = 0.667, total resistance coefficient ≈ 0.22
- Sharp exit, projecting pipe, total resistance coefficient ≈ 1.0
- Sharp edge entrance, total resistance coefficient ≈ 0.5
- Sharp exit, projecting pipe, total resistance coefficient ≈ 1.0
- Sharp edge entrance, total resistance coefficient ≈ 0.5

Total resistance coefficients, k = 8.92. Thus pipe bends pressure drop, Δh_{bends} is:

$\Delta h_{bends} = \frac{U^2 k}{2g} = \frac{40^2 \times 8.92}{2 \times 9.81} = 727.4$ m of air (ΔP_{bends} =85.6 mbar).

The pipe pressure drop due to friction can be calculated from (see [21, page 44-50]

4.3 Fan

This is for providing primary and secondary air to the test/measuring section. The fan must be capable of overcoming the pressure drop in the cyclone and duct work (screens, valves, bends etc.).

The pressure drop along the duct is mainly due to the friction loss along the duct length and velocity head loss at bends. These losses can be estimated from (see [19, pages 201 - 202] for friction loss guidelines), see also figure 4.4:

- Four 90° bend, total resistance coefficient $\approx 0.9 \times 4 = 3.6$
- One standard tee piece: total resistance coefficient ≈ 1.8
- One enlargement, diameter ratio = 0.667, total resistance coefficient ≈ 0.3
- Contraction, diameter ratio = 0.667, total resistance coefficient ≈ 0.22
- Sharp exit, projecting pipe, total resistance coefficient ≈ 1.0
- Sharp edge entrance, total resistance coefficient ≈ 0.5
- Sharp exit, projecting pipe, total resistance coefficient ≈ 1.0
- Sharp edge entrance, total resistance coefficient ≈ 0.5

Total resistance coefficients, k = 8.92. Thus pipe bends pressure drop, Δh_{bends} is:

$\Delta h_{bends} = \frac{U^2 k}{2g} = \frac{40^2 \times 8.92}{2 \times 9.81} = 727.4$ m of air (ΔP_{bends} =85.6 mbar).

The pipe pressure drop due to friction can be calculated from (see [21, page 44-50]

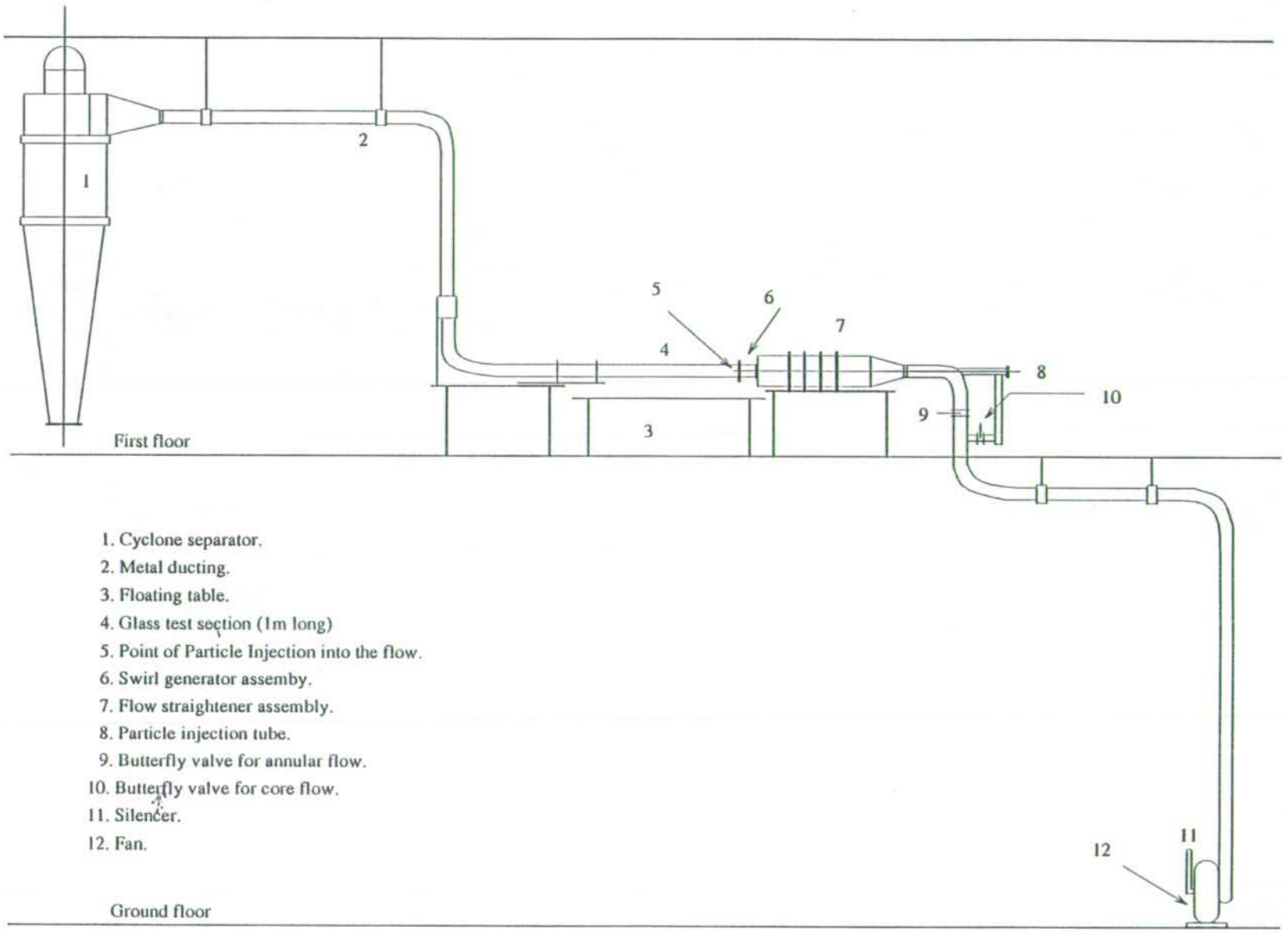

Figure 4.4: Experimental Rig Layout

$$\Delta h_f = -\frac{\Delta P_f}{\rho g} = 8(\frac{R}{\rho U^2})(\frac{l}{d})(\frac{\rho U^2}{2g}) \tag{4.10}$$

Where R is the resistance to flow per unit area of pipe surface. Taking, the pipe roughness, $\varepsilon = 0.046\ mm$ (as that of commercial steel [21, page 44], then with:

The pipe diameter,D	=	101.6 mm (4")
Pipe length, l	=	8m
Air density, ρ	=	1.2 kg/m^3
Air viscosity, μ	=	0.018cP

The Reynolds' number, Re = $\frac{DU\rho}{\mu} = 0.1016 \times 40 \times 1.2 \div 0.018.10^{-3} \approx 2.71 \times 10^5$; with the relative Pipe roughness, $\varepsilon/D = 0.046/101.6 = 0.00045$; figure 4.5 gives $\frac{R}{\rho U^2} \approx 0.002$

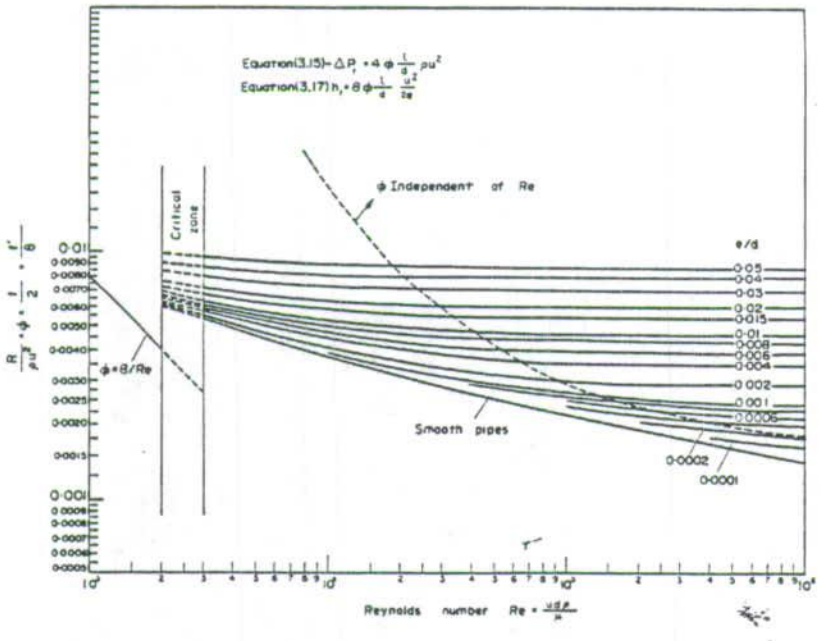

Figure 4.5: Pipe Friction Chart ϕ Versus Re (Reproduced from [21, page 41]

Therefore:

$$
\begin{aligned}
-\Delta P_f/\rho g &= 8 \times 0.002 \times (8/0.1016) \times (40^2 \times 1.2) \\
&= 102.7\ m\ of\ air(12.1mbar)
\end{aligned}
$$

Thus total pressure drop ΔP_{total} is:

$$
\begin{aligned}
\Delta P_{total} &= \Delta P_{cyclone} + \Delta P_{swirl} + \Delta P_{straightner} \\
&\quad + \Delta P_{bends} + \Delta P_f \\
i.e.\ \Delta P_{total} &= 11.4 + 120.3 + 38.0 + 85.6 + 12.1 = 267.4
\end{aligned}
$$

Thus the required fan duty is:

Volumetric flow rate, Q	$\approx$	1520 m^3/h.
Maximum pressure drop	$\approx$	267 mbar.
Required fan differential pressure	$\approx$	300 mbar.

4.4 General Ducting

Linlab metal ducting, was used, purely for ease of assembly. They are however more liable to leak along seems and joints. In order to minimize the risk of electrostatic electricity, metal ducting had to be used. These were additionally earthed. The glass test section was enclosed in plastic wire mesh and only the region under investigation was left uncovered. Two 8 inch butterfly valves were installed for varying the core and annular flow. The air intake into the fan was via a silencer to minimise noise. The fan itself was enclosed in wooded box filled with sound absorbing composite material.

4.5 Cyclone Performance

The performance of the designed cyclone was then calculated using the scaling factor, β, in relation to the Stairmand's standard cyclone, see in figure 10.46a of [38, page 356]. The scaling factor is given by:

$$\begin{aligned}\beta &= \left[(\frac{D_2}{D_1})^3 \times \frac{Q_1}{Q_2} \times \frac{\triangle\rho_1}{\triangle\rho_2} \times \frac{\mu_2}{\mu_1}\right]^{0.5} \\ &= \left[(\frac{0.480}{0.203})^3 \times \frac{223}{1517.7} \times \frac{2000}{2458.8} \times \frac{0.018}{0.018}\right]^{0.5} \approx 1.257\end{aligned}$$

The calculated performance is tabulated in table 4.3.

Table 4.3: Cyclone Performance at Design Conditions

1	2	3	4	5	6	7
Particle Size μm	% in Range	Mean Size μm	Scaled Size μm	Scaled Size Efficiency μm	Collected At Exit	% at Exit %
		$\frac{(2)\times Mean(1)}{100}$	$Mean(1) \times \beta$	Ref [111]	$\frac{(2)\times(5)}{100}$	$\frac{[(2)-(6)]\times 100}{\Sigma[(2)-(6)]}$
75	2.0	1.50	94.2	100.0	2.0	0.0
53-75	9.0	5.76	80.4	100.0	9.0	0.0
38-53	33.3	15.15	57.2	100.0	33.3	0.0
27-38	33.4	10.86	40.8	100.0	33.4	0.0
19-27	15.0	3.45	28.9	97.7	14.7	49.3
13-19	3.6	0.58	20.1	96.0	3.5	20.5
9.4-13	2.0	0.22	14.1	94.4	1.9	16.1
0-9.4	0.7	0.03	5.9	85.9	0.6	14.1
		Σ37.55			Σ96.3	Σ100

Thus, the expected cyclone collection efficiency at design condition is 96.2% and is acceptable.

The general performance of the cyclone under different experimental flow conditions (velocity and particle density) was checked and is tabulated in table 4.4.

Table 4.4: Calculated Cyclone Performance at Different Experimental Conditions

Test Section Velocity	Cyclone Velocity		Cyclone ΔP	$\rho = 1300\, kg/m^3$		$\rho = 2460\, kg/m^3$	
	Inlet	Exit		Scale β	Collected At Exit	Scale β	Collected At Exit
m/s	m/s	m/s	mbar	-	%	-	%
5	1.8	0.9	0.1	5.57	99.0	4.05	99.0
10	3.5	1.8	0.4	3.94	99.0	2.87	98.9
15	5.3	2.7	0.9	3.22	99.0	2.34	98.9
20	7.0	3.6	1.7	2.79	98.9	2.03	98.8
25	8.8	4.5	2.6	2.49	98.9	1.82	98.7
30	10.6	5.4	3.8	2.28	98.9	1.65	98.6
35	12.3	6.3	5.1	2.11	98.9	1.53	98.5
40	14.1	7.2	6.7	1.97	98.8	1.43	98.4

Thus overall, general performance of the cyclone and pressure drop under different experimental flows is acceptable.

Experiments were also done to check the performance of the designed cyclone. The port for collecting particles was carefully cleaned using a vacuum machine and weighed. Similarly the feed hopper and feed was cleaned and charged with a known weight (12 kg) of 75μm particles which were the injected into the air delivery system. The collected particles were then weighed. A collection efficiency of 96% was obtained.

Chapter 5

Experimental Rig Testing & LDA Experiments

After the experimental rig assembly was ready, the rig had to be tested:

- Checks for air leaks, particularly in duct sections carrying particles that are in areas where the laser light is in use, this is for safety reasons, it is undesirable to have laser light randomly scattered in the laboratory.
- Verify the installed fan throughput and establish the velocity range in the core and annular pipe sections using Pitot-static tubes.

This was then followed by carrying out the actual velocity measurement experiments using both laser Doppler velocimetry, LDA and Particle Image Velocimetry, PIV. LDA experiments are reported later in this chapter, while PIV experiments are covered in chapter six.

5.1 Experimental Rig Testing

Linlab ducting (galvanised tubes with male and female ends), though easy to install, were found to be more prone to leaks, and constant leak monitoring had

to be adopted.

5.2 Pitot-Static Velocity Measurements

Pitot-static tubes, of 2mm diameter aperture were used to measure the velocity in the core and annular sections of the air feed sections. These were located at the centre of the respective pipe cross-sections. The relationship between the recorded pressure drop, in height of air (flowing fluid) and velocity, for a simple Pitot-static tube is given by equation 5.1 see also [59, page 5-8]):

$$U = C\sqrt{2g\triangle h\frac{\rho_l}{\rho_g}} \tag{5.1}$$

where ρ_l is the density of the manometer liquid and ρ_g is that of the gas flowing gas.

The value of the coefficient of discharge, C for simple Pitot-static tubes is between 0.98 and 1.0 [59, page 5-8], a value of 1.0 was used.

In order to be able to get reasonably accurate velocity measurements using a Pitot-static tube, a straight calming (away from bend or obstruction) section of length equal to about 50 pipe diameters upstream and downstream of the measurement point is required [22, page 104], [59, page 5-8]. Due to space constraints, see figure 5.1, the Pitot-static tubes were installed just after the butterfly valves and in the vicinity of bends, with maximum straight lengths of 7 pipe diameters (360mm) only. Therefore the pressure drop readings, especially at low valve openings are likely to have appreciable errors, which will also be

reflected in the calculated velocity. As the levels of disturbance caused by the valves were so high, it was not possible to measure the velocity at valve openings lower than the third valve slot (approximately 30% open).

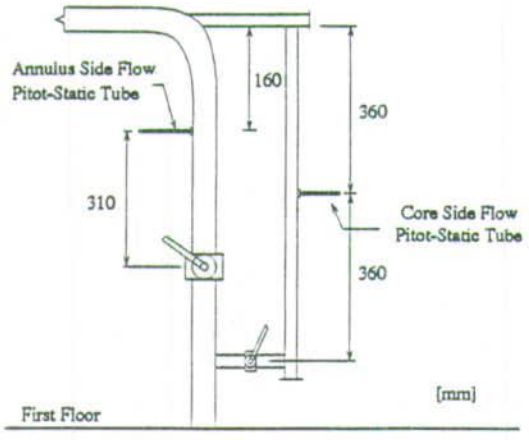

Figure 5.1: Pitot-Static Tubes' Locations

Results of the Pitot-static measurements are shown in figures 5.2 to 5.6. In the 2 inch pipe (core), 11.2 m/s velocity was measured when both valves (core and annular) were only 30% open, and 28.3 m/s, when both valves are fully open. In the annular, 4 inch pipe, the measured velocity was 6.1 m/s when both the core and annular valves were 30% open, and 70.3% when both valves fully open. Thus in order to get a wide range of velocity ratio in future experimental work, better measurement and refined flow control would be required.

The maximum total volumetric flow rate, at maximum pressure drop (60° swirl generator installed), calculated from the measured velocity, both core and annular valves fully open) was 1100.5 m^3/h which compares well with the design specification of 1517.7 m^3/h see page 89

Velocity measurements were also made with different swirl generators installed

and the results are summarised in table 5.1

Table 5.1: Summary of Velocity Measured by Pitot-Static Tubes

Core Pipe Section Velocity [m/s]						
Valve %Open		Installed Swirl Generator				
		None	15°	30°	45°	60°
30	30	11.19	21.23	22.10	22.93	22.93
30	100	16.97	13.71	18.39	23.21	22.38
100	30	29.18	47.08	46.82	47.74	48.65
100	100	28.31	32.43	40.19	45.46	49.67
Annular Pipe Section Velocity [m/s]						
Valve %Open		Installed Swirl Generator				
		None	15°	30°	45°	60°
30	30	6.13	8.67	10.01	10.01	7.08
30	100	73.39	57.61	56.84	40.81	23.74
100	30	5.0	10.01	10.62	10.01	5.0
100	100	70.25	54.25	55.84	41.55	25.27
Core Valve	Annular Valve					

After establishing the fan throughput and the maximum velocity ranges expected both in the core and annulus regions, Laser Doppler Anemometry, LDA, measurements were carried out in the test section.

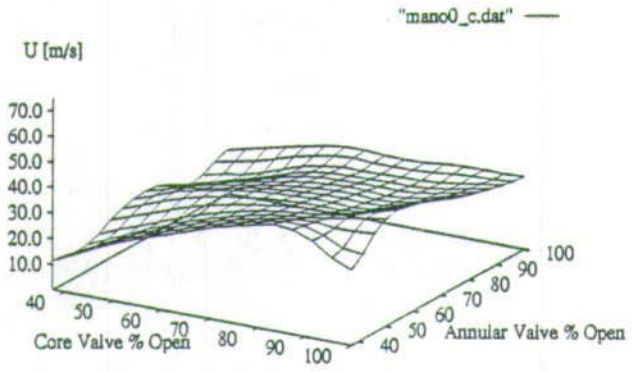

(a) Core Velocity

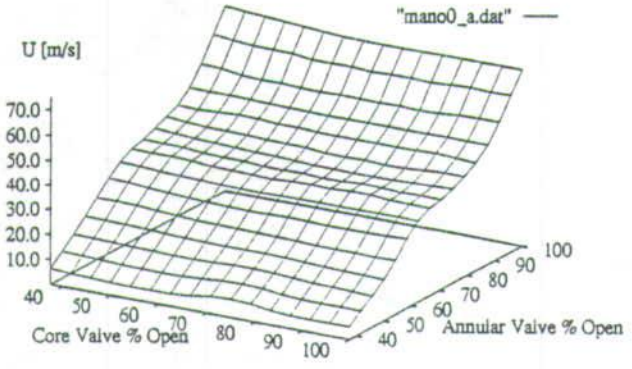

(b) Annular Velocity

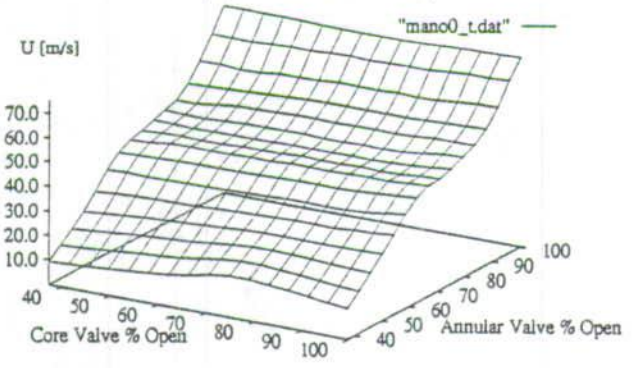

(c) Total Velocity

Figure 5.2: Pitot-tube Measurements (Without Swirl Generator)

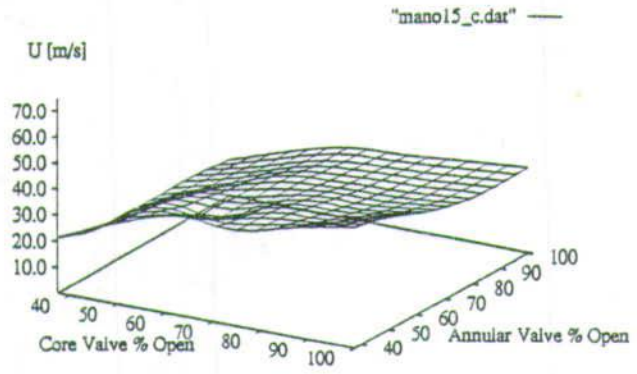

(a) Core Velocity

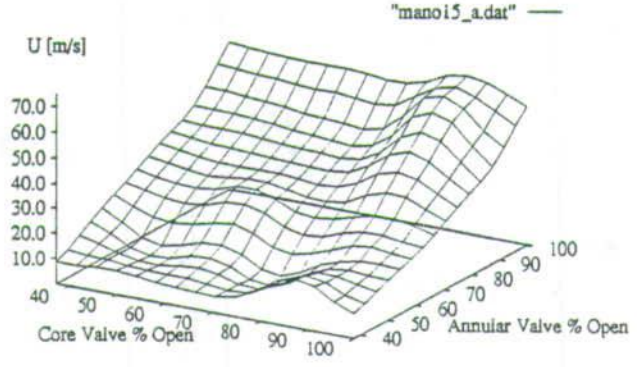

(b) Annular Velocity

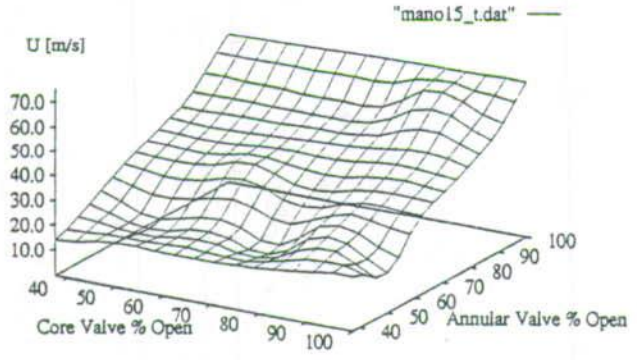

(c) Total Velocity

Figure 5.3: Pitot-tube Measurements With 15° Swirl Generator

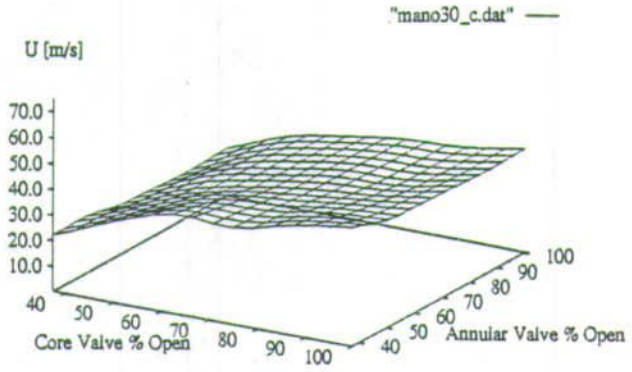

(a) Core Velocity

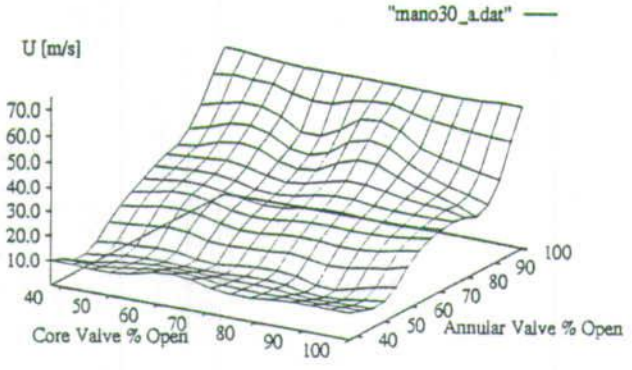

(b) Annular Velocity

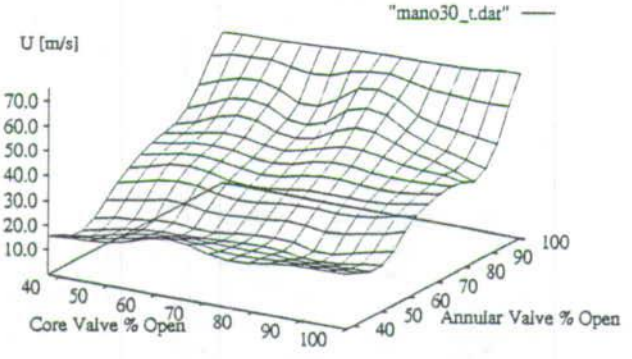

(c) Total Velocity

Figure 5.4: Pitot-tube Measurements With 30° Swirl Generator

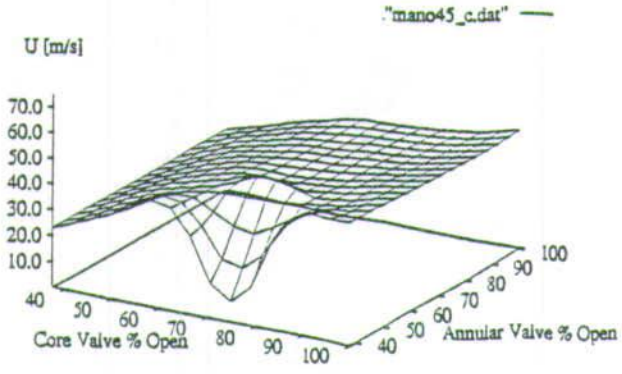

(a) Core Velocity

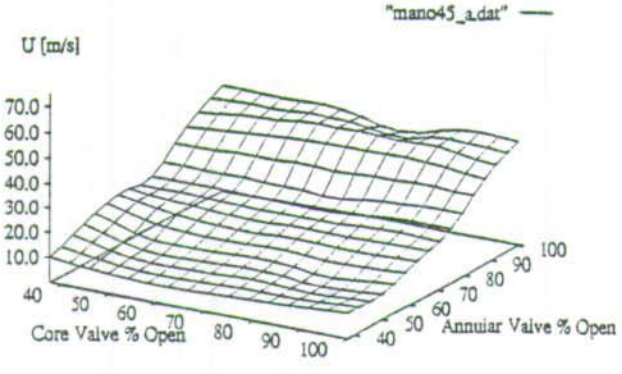

(b) Annular Velocity

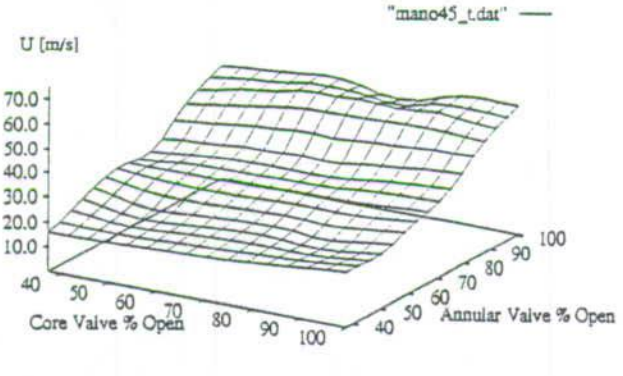

(c) Total Velocity

Figure 5.5: Pitot-tube Measurements With 45° Swirl Generator

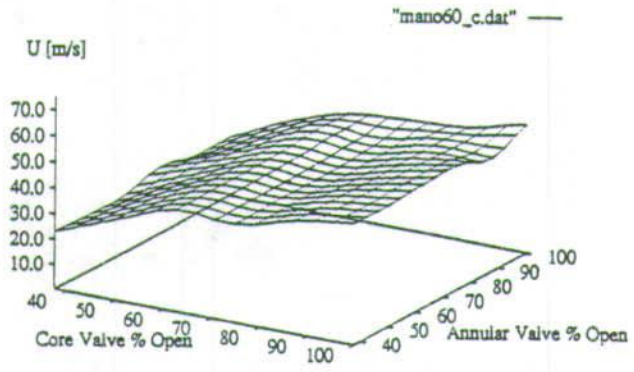

(a) Core Velocity

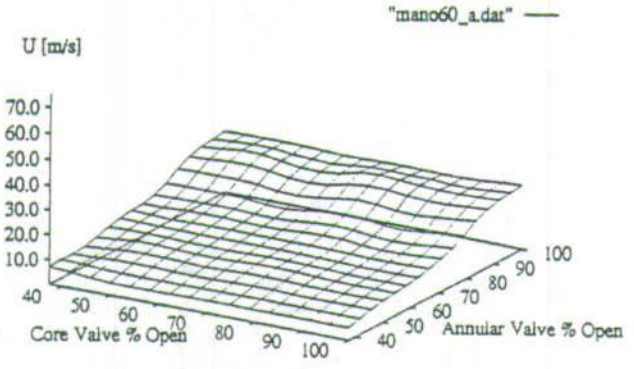

(b) Annular Velocity

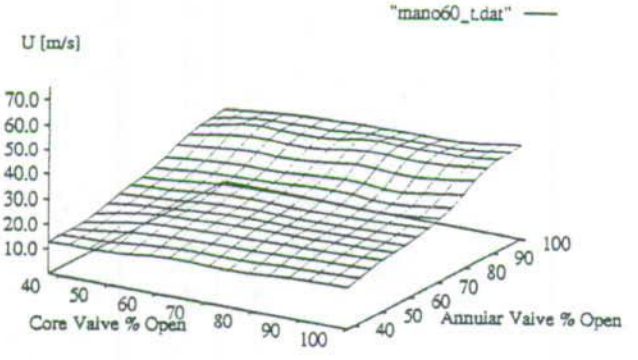

(c) Total Velocity

Figure 5.6: Pitot-tube Measurements With 60° Swirl Generator

5.3 Discusion of Rig Testing Results

The experiments confirmed that the facility was capable of delivering a flow rate of 100 m^3/h at maximum pressure drop (60° swirl generator installed and both the core and annular valves fully open). The maximum design flow rate was 1518 m^3/h.

The results however show poor variation of velocity with the core valve opening (for any given annular valve opening) see figures 5.2 to 5.6. Thus better flow regulation methodologies would have to be adopted in future experiments. Some of the possibilities include installing better control valves, a by-pass line or some form of flow restrictor in the core line.

The dip in figure 5(a) at 80% core valve opening can not be explained. It sort of suggests some form of air stagnation which could be induced by among other things high back pressure from the annular line. The annular velocity however, at this valve setting is not significantly higher. The probability of experimental errors can not be ruled out.

All Pitot-static tube velocity measurements have errors due to reading of the liquid column approximated to be ± 0.5 mm which translates from equation 5.1:

$$\begin{aligned} U &= \pm\sqrt{2 \times 9.81 \times 0.5.10^{-3} \times \frac{760}{1.2}} \\ &= \pm 2.5 m/s. \end{aligned}$$

In general the rig's functionality was sound. Particularly the glass test section assembly. This unit could be easily deassembled, cleaned and reassembled. There is still room for improving the rig functionality especially in the following

areas:

- The lindep metal ducting used for ease of assembly proved to be more susceptible to leaks especially along the weld seams. Leaks pose serious safety hazards in light scattering and dust.Drawn out metal pipes should be seriously considered.

- The valve system for regulating both the primary and secondary air streams was not working adequately firstly because of their proximity to bends, and secondly, because of their make - (butterfly valves). See figure 5.1 on their arrangements. One possibility would be to move the secondary air branching further upstream on the lower floor and also installing better control valves, installing bypass line/stream or adopting both measures on both the primary and secondary lines.

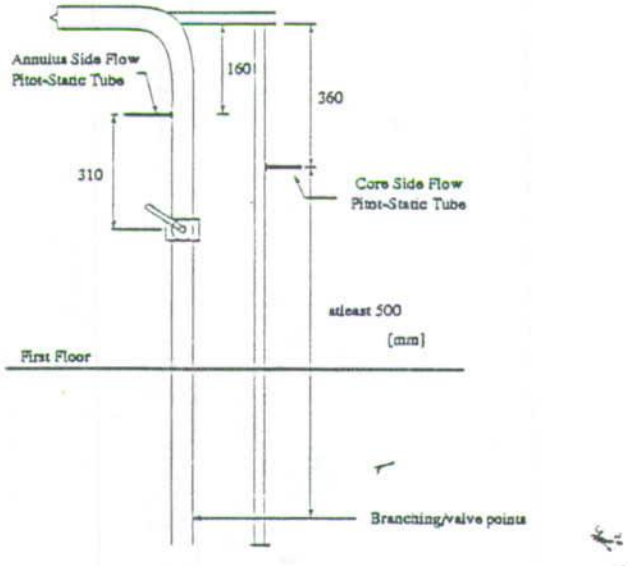

Figure 5.7: New/Proposed Branching/Valve Locations

- The rig would also require, at a later stage, a mechanism for seeding the

primary air phase so that the real two phase experiments could be done (be able to measure both the particle and air velocity). A smoke or mist generating system is one of the possibility.

- It could be feasible to replace the pitot-static tube with an orifice plate, this could be connected to a pressure transducer so that the flow measurement could be logged in directly by computer during the experiment offering improved accuracy of the reference velocity.

5.4 Laser Doppler Anemometry, LDA Measurements

The Laser Doppler anemometry technique is a well documented and proved one and is still undergoing further refinements to make it suitable for even more applications, e.g. particle dispersion measurements [58] and [17]. By virtue of its being a point measuring technique, LDA is more suitable for steady rather than fluctuating flows.

LDA velocity measuring technique relies on the formation of a set of fringes caused by the interference of two overlapping coherent beams. In transmission mode, a particle crossing these fringes will block off much of the light in the bright fringes and only a little light in a dark fringe. The fringe visibility varies from 0 to 1.0 (dark fringes are completely black) for the case of equal light intensity in both the interfering beams. The particles can be seeding particles or actual dispersed particles making up the second phase. Seeding particles are usually small enough faithfully to follow the fluid flow fluctuations.

High fringe visibilities can be achieved by ensuring that correct particle size to

The ratio of the amplitude of the Doppler signal to the amplitude of the pedestal, i.e. the ratio of high to low frequency components is referred to as the visibility and depends on the laser power, ratio of particle size to fringe spacing, relative intensities of the two light beams and alignment of the optics and the light collecting system. High visibilities (Large signal-to-noise ratios) generally allow signal processing equipment which is less complicated and less expensive.

In principle, the mean velocity components, the Reynolds stress, the velocity fluctuations and other correlations quantities can be evaluated from their relationship with the measured mean signal frequency, f. Frequency analysis (frequency tracking) or counting procedures can be used in this evaluation. Instantaneous velocity or energy spectra can only be obtained with devices which follow the signal in real time (e.g. frequency tracking demodulators). If the frequency oscillation information is recorded in real time, counting procedures can also be used to evaluate instantaneous velocity components, the Reynolds stress and other velocity fluctuations correlations quantities.

When spherical particles are used, particle size information can also be obtained from the intensity of the scattered light, as this is dependent on the viewing angle and the particle diameter. This effect is employed in the phase-Doppler LDA configuration where three detectors observe the scattered light at different angles. Commercial LDA systems are available and one was used in this experiment.

To enable correct interpretation of the intensity distribution and discrimination of the 180 degree velocity direction ambiguity, frequency shift is normally required. Frequency shift, (normally applied to one of the light beams) increases or decreases the measured frequency, a frequency shift of double the magnitude

The ratio of the amplitude of the Doppler signal to the amplitude of the pedestal, i.e. the ratio of high to low frequency components is referred to as the visibility and depends on the laser power, ratio of particle size to fringe spacing, relative intensities of the two light beams and alignment of the optics and the light collecting system. High visibilities (Large signal-to-noise ratios) generally allow signal processing equipment which is less complicated and less expensive.

In principle, the mean velocity components, the Reynolds stress, the velocity fluctuations and other correlations quantities can be evaluated from their relationship with the measured mean signal frequency, f. Frequency analysis (frequency tracking) or counting procedures can be used in this evaluation. Instantaneous velocity or energy spectra can only be obtained with devices which follow the signal in real time (e.g. frequency tracking demodulators). If the frequency oscillation information is recorded in real time, counting procedures can also be used to evaluate instantaneous velocity components, the Reynolds stress and other velocity fluctuations correlations quantities.

When spherical particles are used, particle size information can also be obtained from the intensity of the scattered light, as this is dependent on the viewing angle and the particle diameter. This effect is employed in the phase-Doppler LDA configuration where three detectors observe the scattered light at different angles. Commercial LDA systems are available and one was used in this experiment.

To enable correct interpretation of the intensity distribution and discrimination of the 180 degree velocity direction ambiguity, frequency shift is normally required. Frequency shift, (normally applied to one of the light beams) increases or decreases the measured frequency, a frequency shift of double the magnitude

of the measured frequency will leave the magnitude of the frequency being measured unchanged.

There are different ways of effecting frequency shifting, e.g. by the use of rotating gratings, Bragg cells, solid state, electric-optic cells effects in crystals and water-filled acoustic-cells, etc. Rotating grating offer the cheapest and simplest way of inducing frequency shifts in excess of 1 MHz but, for reasons of efficiency and stability, are normally used for shifts of less than 3 MHz. Acoustic-optic cells when operated in the Bragg mode (yield one beam with a frequency and direction different from the incident beam), These so called Bragg cells, generally generate much higher frequency shifts than those of rotating grating (largest 40 MHz, lowest 3.5 MHz). Small frequency differences can be obtained at higher efficiency by using two cells of slightly different frequency either operating in series (shifting in opposite direction) or in parallel (shifting in the same direction). A frequency shift of around 9 MHz with appropriate filters and electronic arrangements to process the resulting high-frequency signals is normally considered adequate for flow measurement in turbulent and recirculation zones.

In this experiment, a commercial 10mW He-Ne laser supplied by Spectra-Physics was used. This produced a single laser beam which was firstly split into two beams. The first beam is circularly polarized. The second beam was first passed through a Brag cell (frequency shifting, helps to discriminate direction) and then split into two beams whose polarisation is normal to each other. Then all three beams are converged by a lens onto a point in the flow region to produce horizontal and vertical fringes oriented at 90° to each other of 3mm by 1mm diameter.

An aerosol generator (bubble air in oil container with a nozzle outlet) generating 1μ corn oil droplets was used to seed the flow. The same tube for injecting particles was used. The scattered light was detected by the photo-multiplier which was focused onto the point of convergence of the three beams. This detected the intensity and frequency of the light scattered. The front optics of the photo-multiplier separated the vertical and horizontal velocity components of the flow by a means of a polarisation filter.

Each velocity component was detected and amplified by the photomultiplier before being processed by a DISA 55L90a commercial counter processor unit. This analyses individual Doppler bursts to validate genuine bursts (ignore noise). The DISA (now DANTEC) counter processor was interfaced to a IBM 386 compatible PC that was used to make the statistical analysis of the reported frequency and calculate the velocity. As only one counter processor was available, only one velocity component was measured.

The optics were mounted on a traversing mechanism to allow probing of the flow region along the length, across the diameter of the tube and vertically, see figure 5.8

5.4.1 LDA Experiments Results

LDA velocity measurements were carried out at several positions in the axial and radial directions and the results are shown in figure 5.10 to 5.21. These LDA results, although were within the expected velocity range (basing on the initial Pitot-static measurements), but they are far from being equal to it for

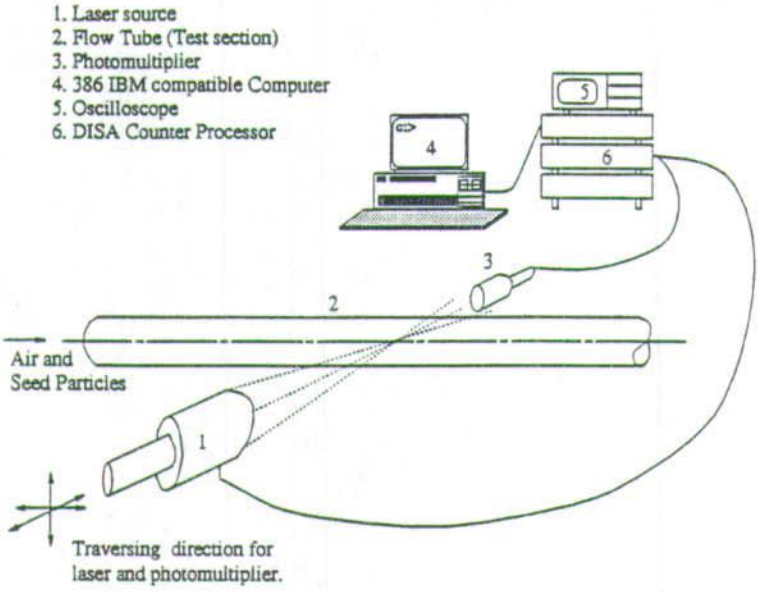

Figure 5.8: Sketch of LDA Experiment Layout

two reasons:

- The point of measurement of the LDA and Pitot-tube were different (location and cross section area).
- The LDA measurement position would be accounting for more or less total flow (although the two stream might not yet be completely mixed) while the Pitot-tube measurement only measures a single section (see figure 5.9 and compare with figure 5.8)
- The LDA measurement volume was about 1mm diameter, the injection tube diameter was 10 mm while the flow/test section diameter was 100mm in diameter

In the graphs, the pitot-tube readings are given purely for reference purposes (core and annular valve setting).

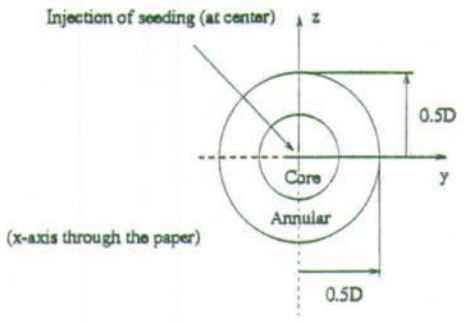

Figure 5.9: LDA Seeding Position

At radial distances beyond 21mm from the center of the test section tube, the LDA signal became intolerably weak, and no measurements beyond this radial position were made.

This poor quality of the signal is likely to have been caused by two reasons, first and foremost the fact that spread/dispersion of the jet did not go beyond this radial position in the axial range of 450mm in which the measurements were being carried and, secondly, the glass test section was about 3mm thick, and might significantly affect the laser beam path by refraction.

5.4.2 Discussion of LDA Measurements

In all experimental results, the center line velocity (position y=0;z=0) can be found to be fairly uniform (less fluctuations) figures 5.10 to 5.21. Also the mixing of the two air stream (core and annular) is evedent in the sense the two curves do converge downstream.

It can be seen that although the velocity measured was within the core region, in experiments done where the annular velocity is higher than the core velocity,

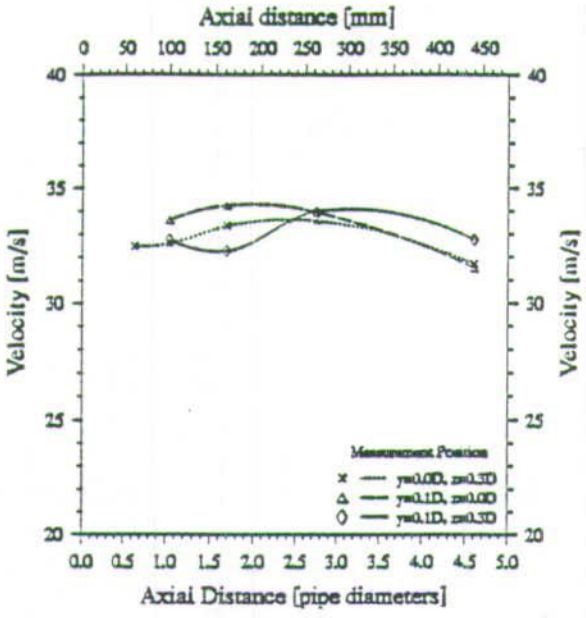

(Pitot-tube: Core 34.49 m/s; Annular 18.05 m/s)

Figure 5.10: LDA Velocity Measurement: Velocity Ratio 0.5

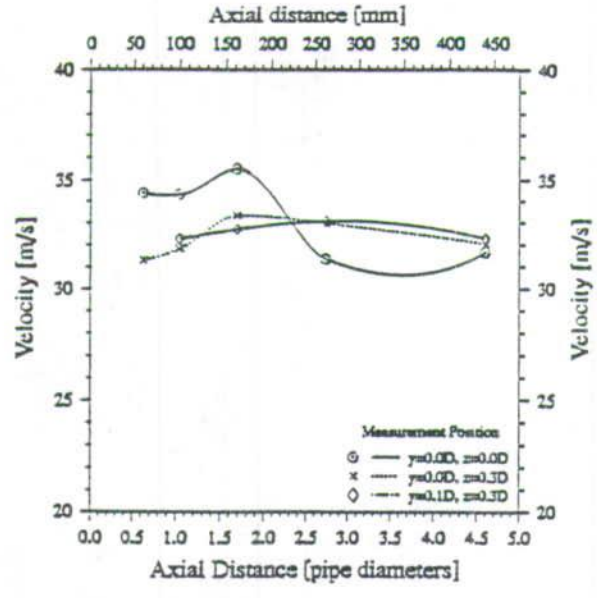

(Pitot-tube: Core 29 m/s; Annular 18 m/s)

Figure 5.11: LDA Velocity Measurement: Velocity Ratio 0.6

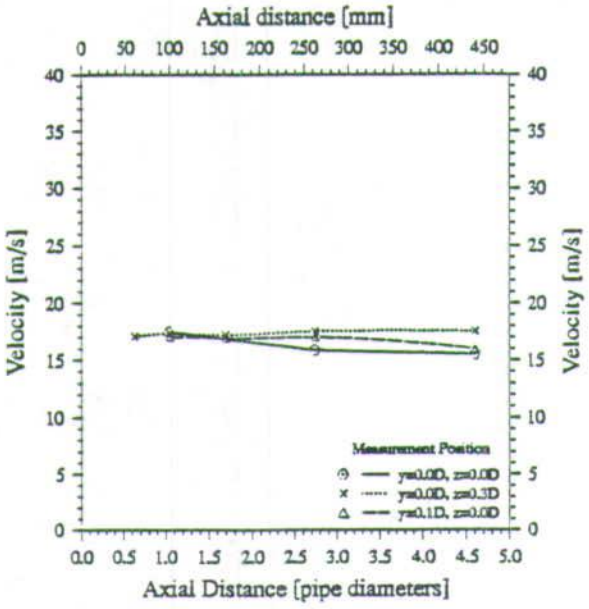

(Pitot-tube: Core 20.33 m/s; Annular 19.06 m/s)

Figure 5.12: LDA Velocity Measurement: Velocity Ratio 0.9

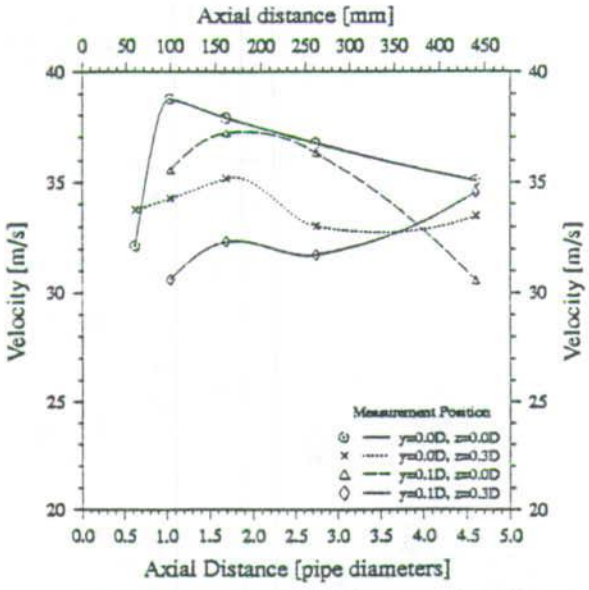

(Pitot-tube: Core 32 m/s; Annular 32 m/s)

Figure 5.13: LDA Velocity Measurement: Velocity Ratio 1

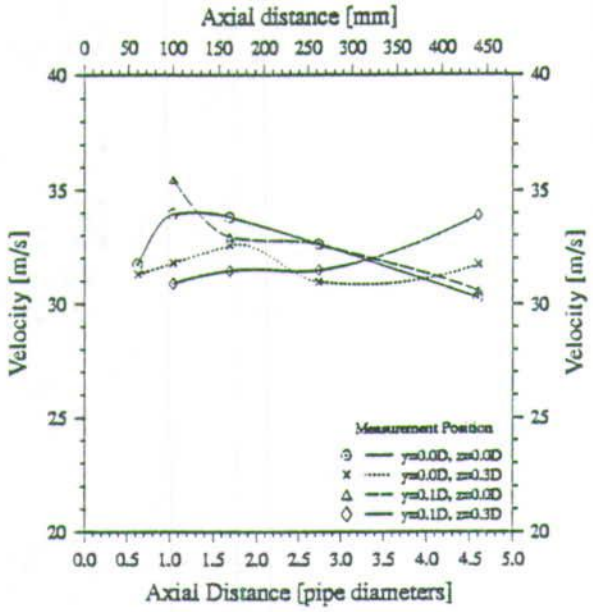

(Pitot-tube: Core 29.61 m/s; Annular 32.05 m/s)

Figure 5.14: LDA Velocity Measurement: Velocity Ratio 1.1

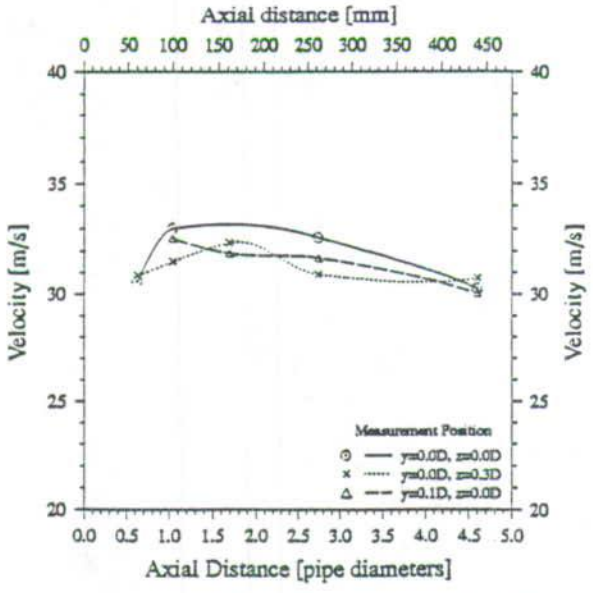

(Pitot-tube: Core 25 m/s; Annular 33 m/s)

Figure 5.15: LDA Velocity Measurement: Velocity Ratio 1.3

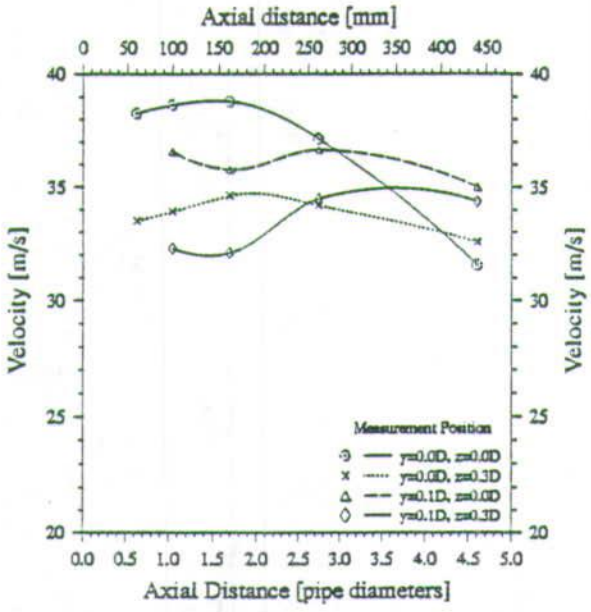

(Pitot-tube: Core 28.97 m/s; Annular 37.12 m/s)

Figure 5.16: LDA Velocity Measurement: Velocity Ratio 1.3

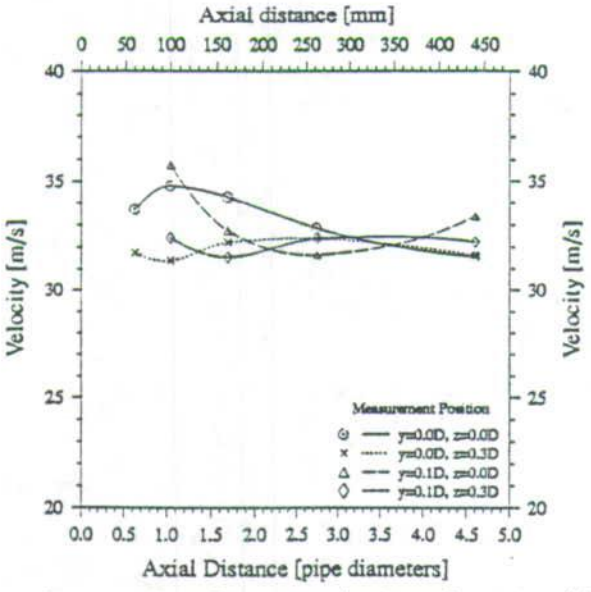

(Pitot-tube: Core 27 m/s; Annular 38 m/s)

Figure 5.17: LDA Velocity Measurement: Velocity Ratio 1.4

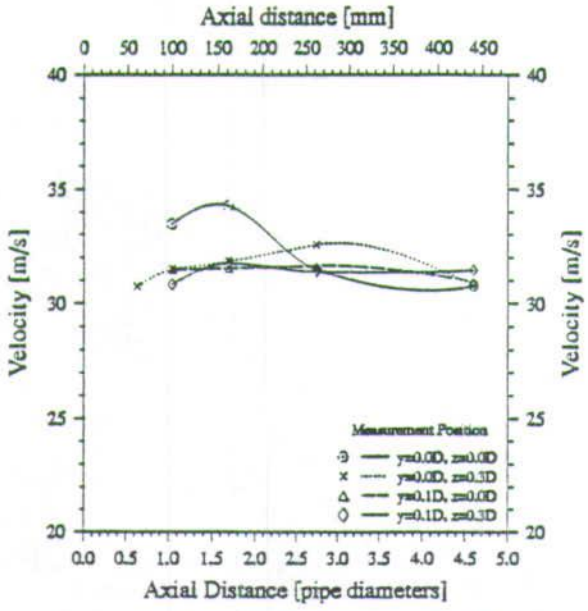

(Pitot-tube: Core 22.38 m/s Annular 38.77 m/s)

Figure 5.18: LDA Velocity Measurement: Velocity Ratio 1.7

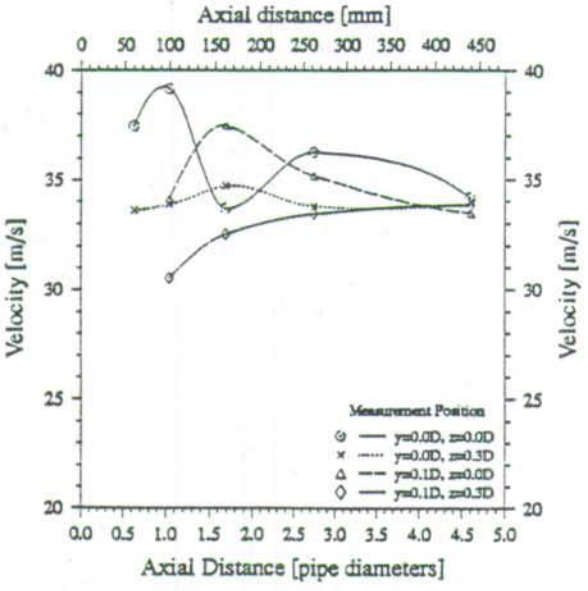

(Pitot-tube: Core 26 m/s; Annular 48 m/s)

Figure 5.19: LDA Velocity Measurement: Velocity Ratio 1.8

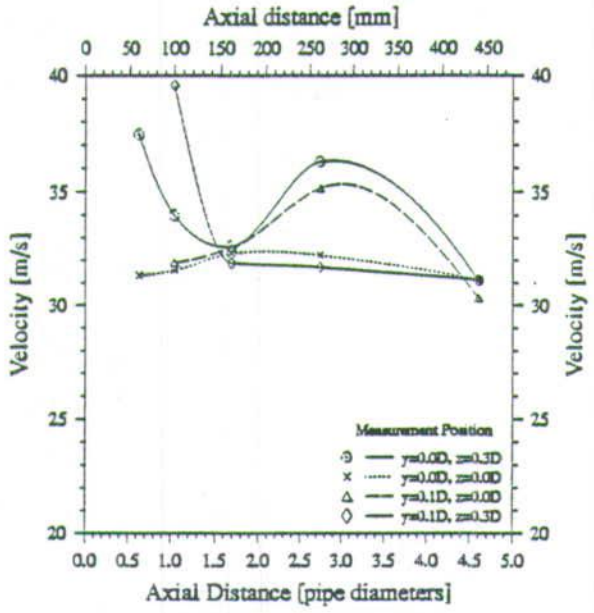

(Pitot-tube: Core 24.52 m/s; Annular 47.80 m/s)

Figure 5.20: LDA Velocity Measurement: Velocity Ratio 1.9

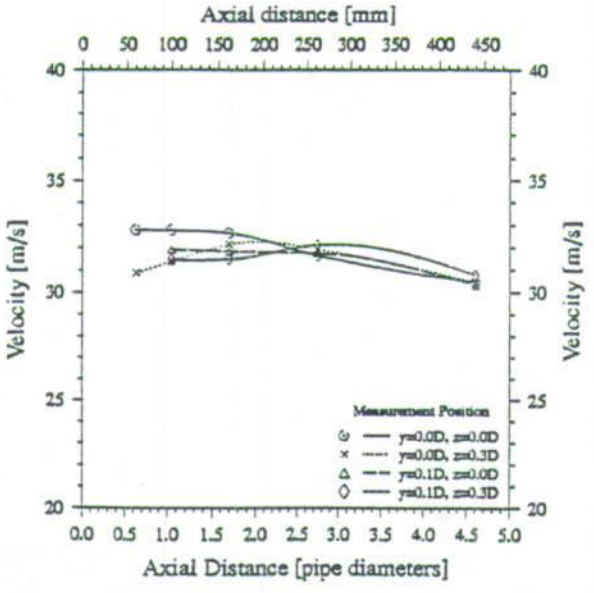

(Pitot-tube: Core 18 m/s; Annular 48 m/s)

Figure 5.21: LDA Velocity Measurement: Velocity Ratio 2.7

the core velocity measured seem to be higher than the set core velocity. This suggests that the core air mass (small in flow volume) is accelerated by the mass of the air in the annular region figure 5.16 to 5.21.

The high peaks upstream in some figures e.g. figure 5.20 where the velocity seems to suddenly increase might have been caused by the occassional uneven delivery of the seeding (e.g. when there is a sudden increase in the compressed air supply).

5.5 Use of LDA in Particle Dispersion Measurements

In this experiment, when the injected particles travel axially downstream, they are radially displaced by the jet turbulence. It is possible to use LDA methods to measure this migration from the jet axis. It is important to note that the extent to which the particles are displaced (along the centre line) depends mainly on the ratio of the time scale (Stokes number) of particle-inertia to that of the turbulence (settling down due to gravity).

As mentioned above, see page 107, the DISA counter processor validates each Doppler bursts. In a conventional LDA experiment, a number of frequency readings of such validated bursts are recorded and used to make any statistical analysis such as calculation of the mean velocity. If say n such readings are required, then the time it takes to record these n validated bursts is inversely proportional to the number density (concentration) of particles crossing this measurement point. If the particle number density (concentration) is high, then it will take only a short time to record the required number of validated Doppler burst signals. Thus, by recording both the frequency and time it takes to record

such n frequency readings, both the velocity and the corresponding particle number density at the measurement point can be established, see also [58] and [17] where this principle was used to actually count droplets.

5.5.1 Particle Dispersion Experiment Results

The results of the dispersion experiments (at particle feed rate 0.8g/s) are shown in figure 5.23 to 5.28.

As the time required to record n (1000, in the experiments) validated Doppler bursts is inversely proportional to the number of particles crossing the measurement point, for this uncalibrated system, this time has been normalised by the value of the time at initial axial measurement point, (at 60mm axial position for all radial positions).

Within the core, the initial number of particles crossing any of the measurement points is reasonably high, and as the particles move axially, more particles disperse, and the required time to record the same number of Doppler signal bursts increases, and thus the normalised particle number density decreases, see figures 5.22(b) to 5.28(b).

Although no dispersion measurements were made outside the core, for similar reasons as those mentioned above in section 5.4.1, it is possible to comment that, outside the core, the number of the particles crossing the initial axial measurement point would be low, but is likely to become higher downstream as more particles disperse. Thus, the normalised particle number density, for this region, would be expected to increase axially.

The particle velocity, seems to increase axially, figures 5.22(a) to 5.28(a), It is however believed that the particles were not accelerating but that, as the annular velocity, in almost all cases, was higher than the core velocity, and the two streams were mixing, the core stream velocity would be expected to increase (and the annular one decreases) until the whole stream velocity becomes uniform at some point down stream. The particles would also be expected to assume the velocity of the surrounding core fluid, which would initially be increasing.

It is also possible, that before the particle velocity settles down to the main stream velocity from the injecting velocity, they would seem to be accelerating. It is thus difficult, to apportion the accelerating phenomena to only one cause.

In the experiments, measurements were done only in one half of the pipe diameter on the assumption that the flow was symmetrical. It would, probably have been better to confirm this experimentally.

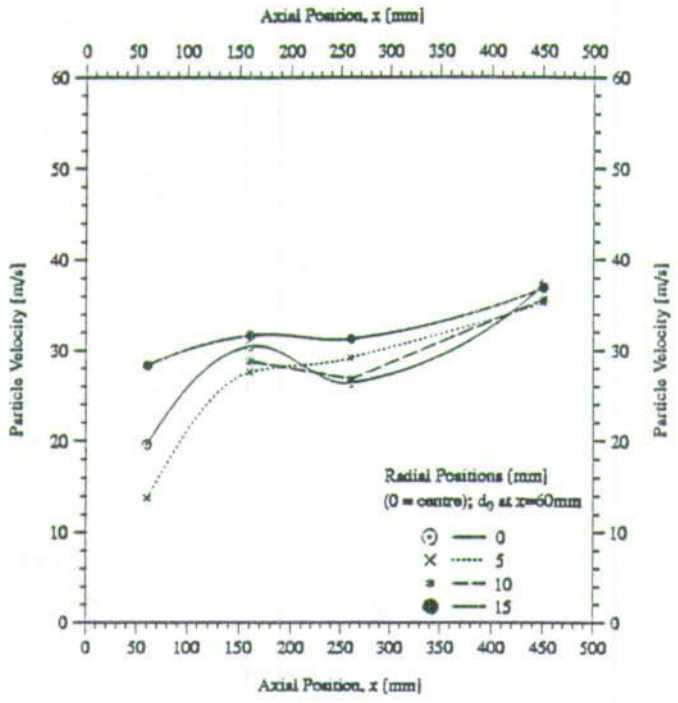

(a) Particle Velocity

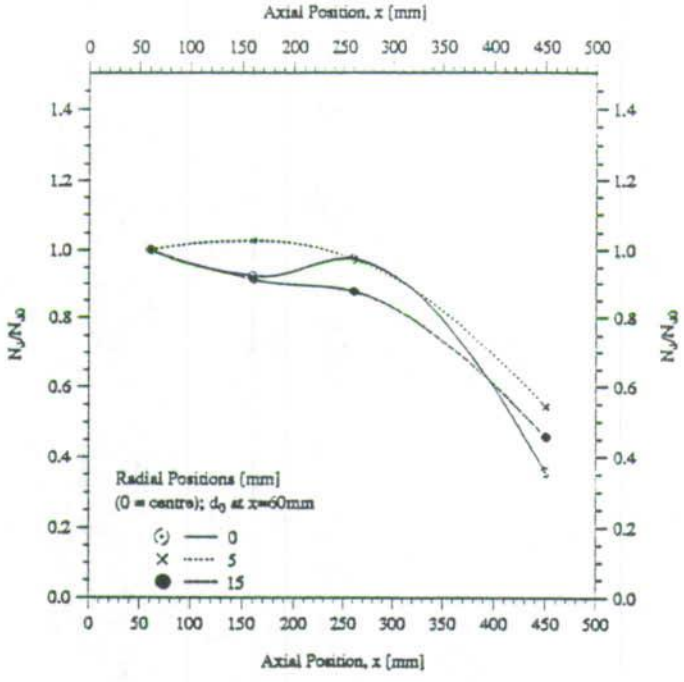

(Pitot-tube: Core 37 m/s; Annular 17 m/s)

(b) Particle Number Density (Dispersion)

Figure 5.22: LDA Particle Dispersion Measurement: Velocity Ratio = 0.45

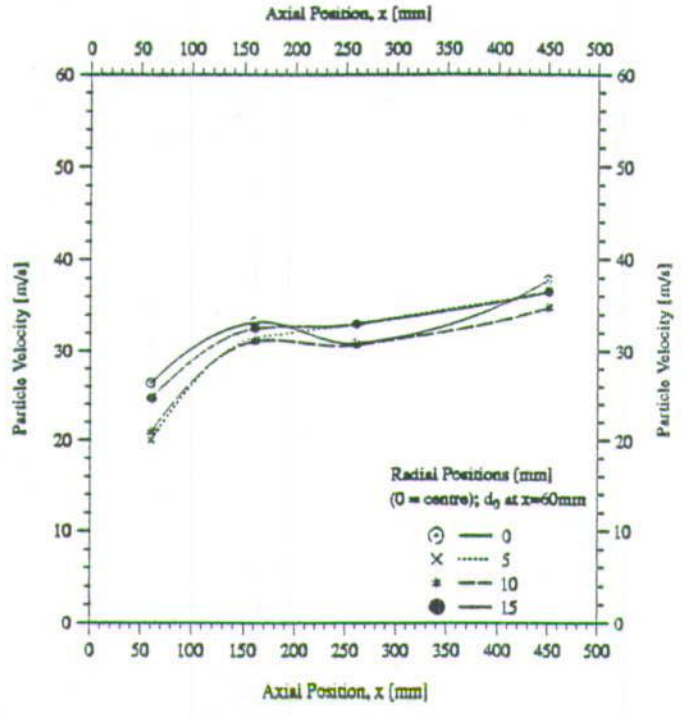

(a) Particle Velocity

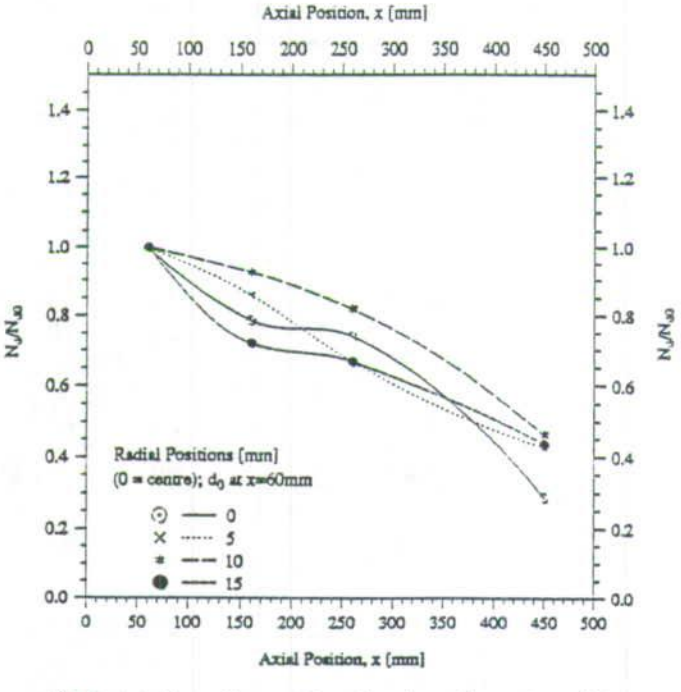

(Pitot-tube: Core 29 m/s; Annular 18 m/s)

(b) Particle Number Density (Dispersion)

Figure 5.23: LDA Particle Dispersion Measurement: Velocity Ratio = 0.6

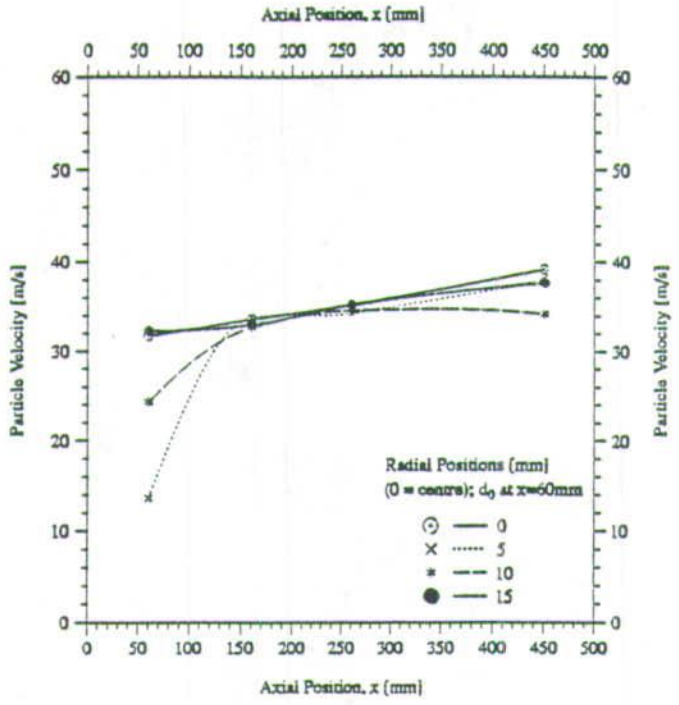

(a) Particle Velocity

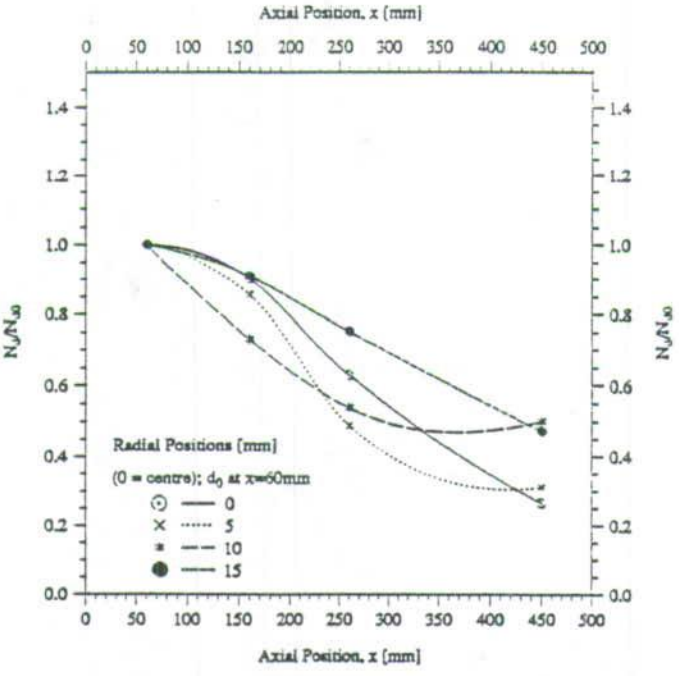

(Pitot-tube: Core 20 m/s; Annular 19 m/s)

(b) Particle Number Density (Dispersion)

Figure 5.24: LDA Particle Dispersion Measurement: Velocity Ratio = 0.9

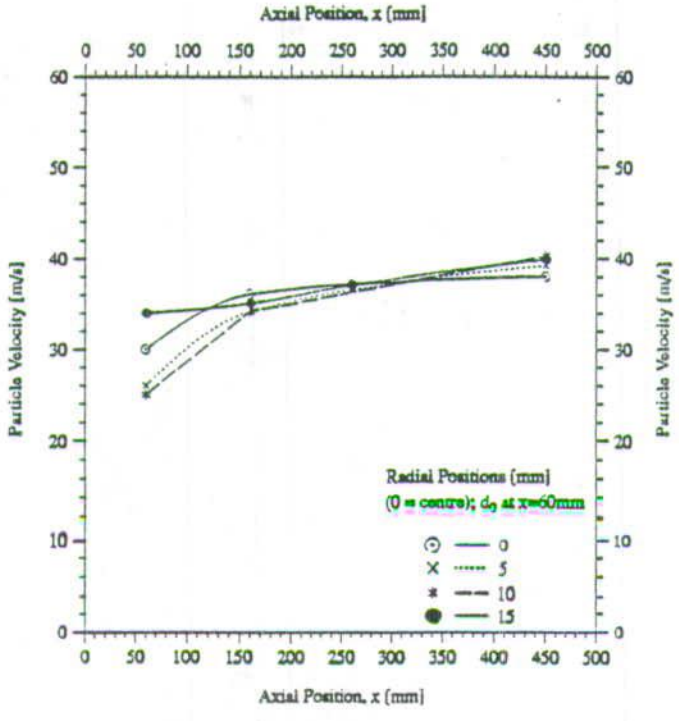

(a) Particle Velocity

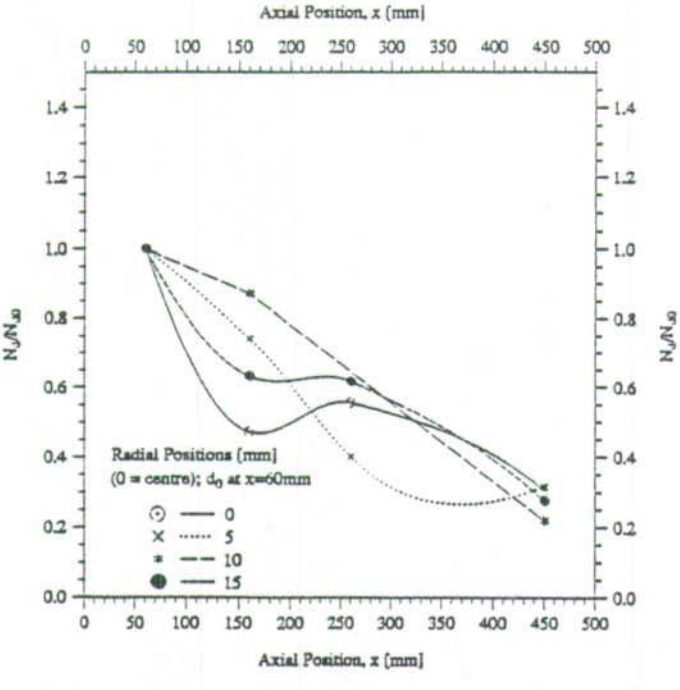

(Pitot-tube: Core 29 m/s; Annular 37 m/s)

(b) Particle Number Density (Dispersion)

Figure 5.25: LDA Particle Dispersion Measurement: Velocity Ratio = 1.3

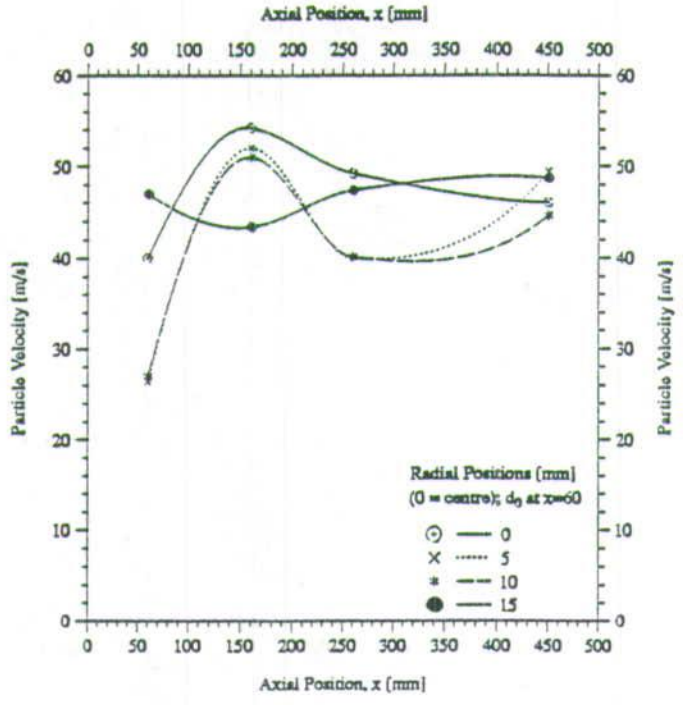

(a) Particle Velocity

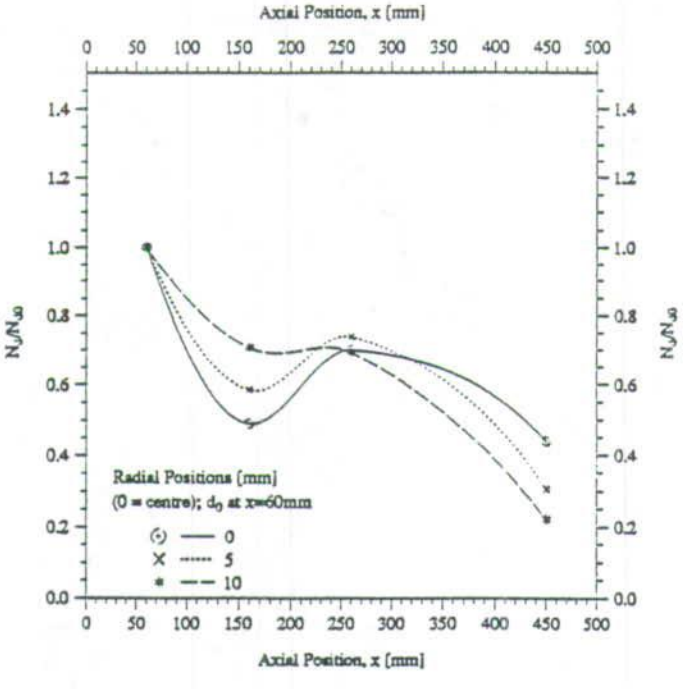

(Pitot-tube: Core 28 m/s; Annular 70 m/s)

(b) Particle Number Density (Dispersion)

Figure 5.26: LDA Particle Dispersion Measurement: Velocity Ratio = 2.5

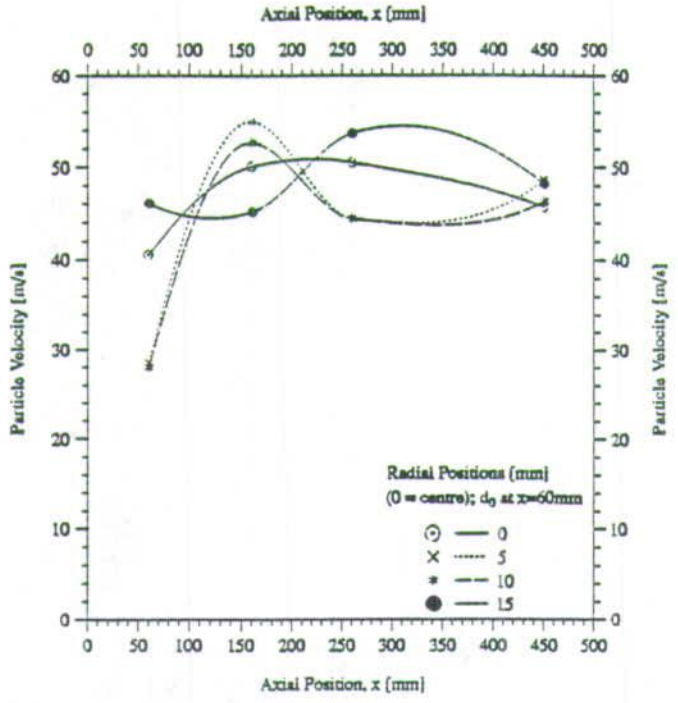

(a) Particle Velocity

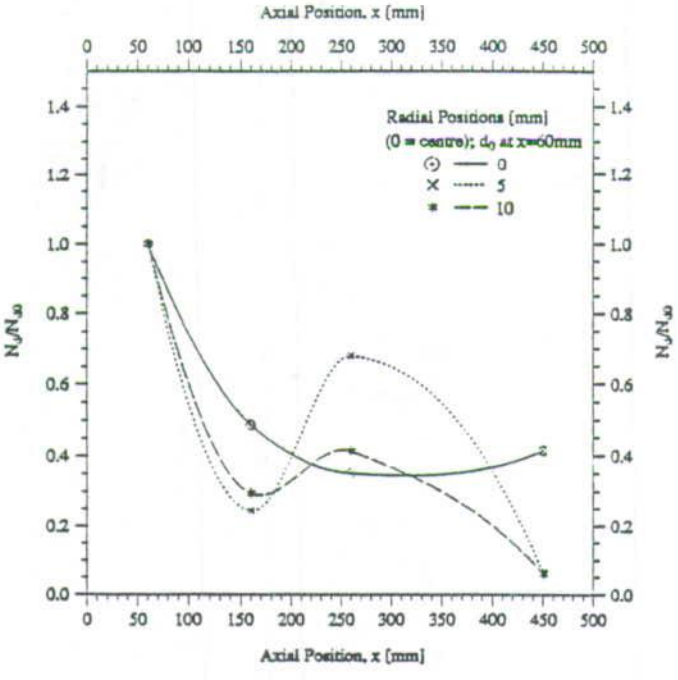

(Pitot-tube: Core 27 m/s; Annular 70 m/s)

(b) Particle Number Density (Dispersion)

Figure 5.27: LDA Particle Dispersion Measurement: Velocity Ratio = 2.6

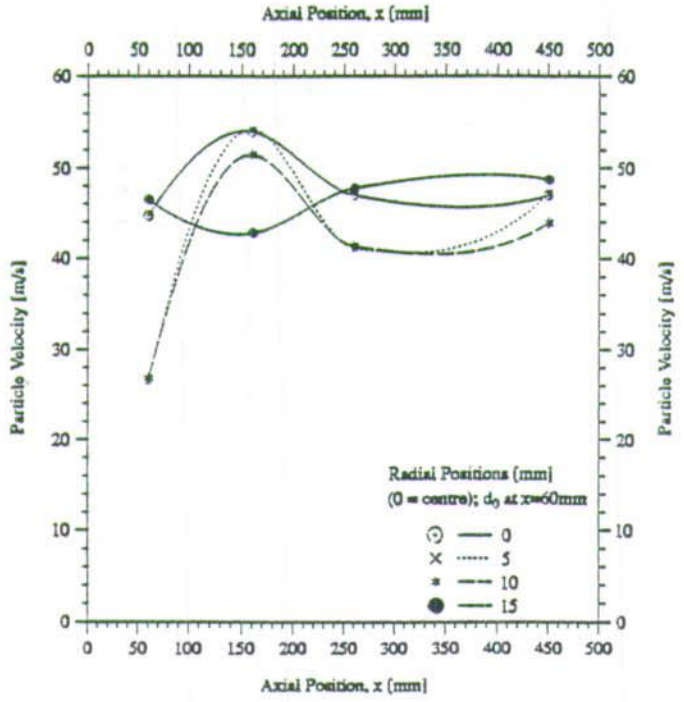

(a) Particle Velocity

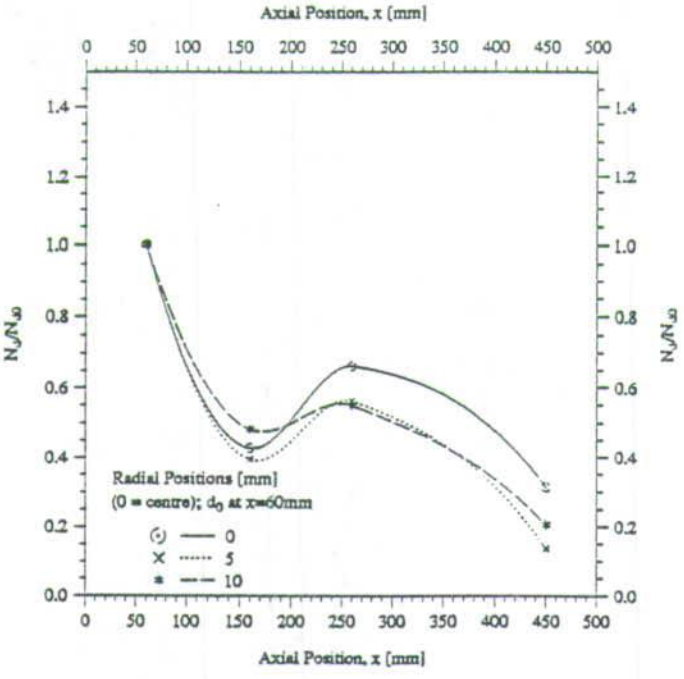

(Pitot-tube: Core 26 m/s; Annular 70 m/s)

(b) Particle Number Density (Dispersion)

Figure 5.28: LDA Particle Dispersion Measurement: Velocity Ratio = 2.7

Chapter 6

Particle Image Velocimetry

PIV is a velocity measuring technique which can "instantaneously" record velocity over a whole flow field. The technique relies on photographing small particles contained in and faithfully following the flow under investigation. Light from a laser source is normally expanded into a two-dimensional sheet and projected into the flow field. The laser beam is then pulsed (either by Q-switch or by a spinning mirror) so that successive images can be recorded on the film plane of a camera placed at right angles to the expanded sheet of laser light [52], [28], [116], [11], [29], [8] and [25]. Figure 6.1 shows the configuration for PIV recording.

There is a large volume of literature on PIV and this is still growing. Particular reference is made to [29], [8], [25], [31], [112], [91], [73], [23], [9], [101] and [89] which cover the basic principles, early developments and application of the PIV technique and [116] and [11] which discuss the equipment. The influence of recording media (film) and comparison with holographic methods is discussed in [110], [6] and [4]. [114] discusses the scattering power of seeding particles. Methods of analysis of multi-exposed PIV negatives have been covered well in [110], [6] and [4]. The image shifting technique to resolve velocity direction ambiguity is discussed in [78], [33], [47], [127] and [34] while [62], [27], [56], [98],

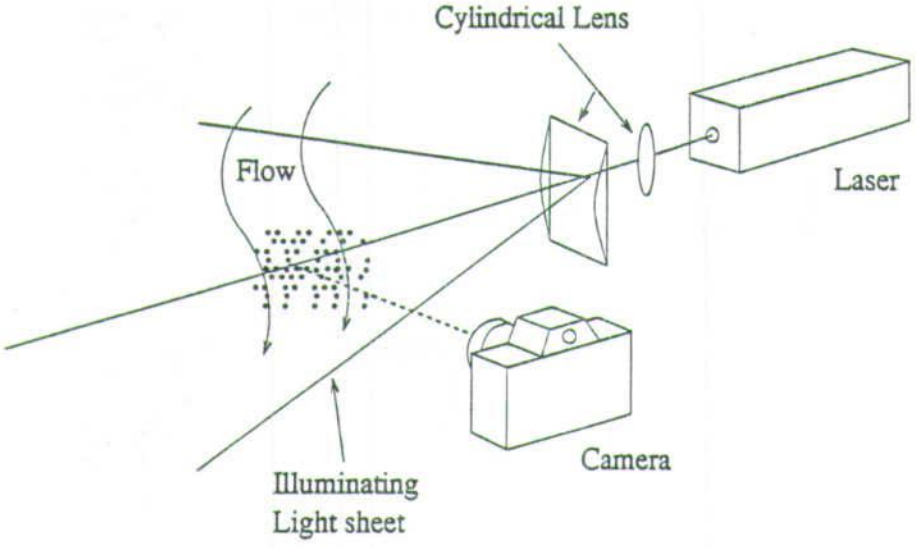

Figure 6.1: PIV Recording

[88], [64], [63], [46], [121], [122], [120] and [54] comment on data reduction and PIV data confidence criteria.

The PIV technique has been employed in diverse research fields such as measurement of strain and planar velocity in engines [82], in particle rope studies [83], measurement of velocity distributions [44], [32], [96], [128], [94], [60] and [123], measurement under water waves [75],[38] and [10], the measurement of surface displacement and tilt in metereology [45] etc. There also has been extensive numerical work and computer simulation related to PIV; some of this work is dealt with in [13], [126], [35], [99], [57], [100], [53], [20] and [125].

6.1 Retrieval of Flow Field Data

The velocity information on the film can be recovered by ascertaining the separation of the particle images. This can be done by either observing the film

directly using a microscope or, more commonly, by interrogating each point on the film using a low powered laser beam (optical interrogation) or by digitising the whole doubly exposed image and storing the digital image in the computer memory for subsequent analysis.

Within a small local region of the negative, over which the fluid velocity is approximately constant, the recorded flow will consist of two similar but displaced random patterns of resolved particle images. The spacing and orientation of successive particle images in the area of the interrogation are directly determined from the two-dimensional position of the signal peaks in the autocorrelation plane, The position of the centroid of the signal peak is directly correlated to the inter-particle image spacing on the negative: normally a micro computer is employed to find the location of these peaks. There are three techniques of producing the correlation function:

i) Fully Optical method: An optical processor is used to generate a two-dimensional squared autocorrelation function, which is later analyzed by computer.

ii) Optical-Digital method: Digitalisation applied after an optical generation of the power spectrum, again numerical analysis completes the analysis.

iii) Fully digital method: Digitalization of the photograph, followed by numerical analysis based on an autocorrelation technique.

6.1.1 Optical Method

Some of the processors used in optical processing include: non linear optical media, Electrically Addressed Spatial Light Modulators (EASLM) and Optically addressed Spatial Light Modulators (OASLM) [43], these perform at the speed of light, and thus provide inherently fast, parallel processing. As the amount of data associated with PIV images is always large, this method has a fundamental advantage over the the other two. For example generating a squared autocorrelation function takes only 10ms (plus 20-40ms for exposing the video) compared to around 1s by the digital method [76]. The system however still needs to digitise the autocorrelation to perform the peak finding. Another disadvantage is that it requires a monochromatic and coherent light source to power the processor. It also has limited resolution [43], see Figure 6.2.

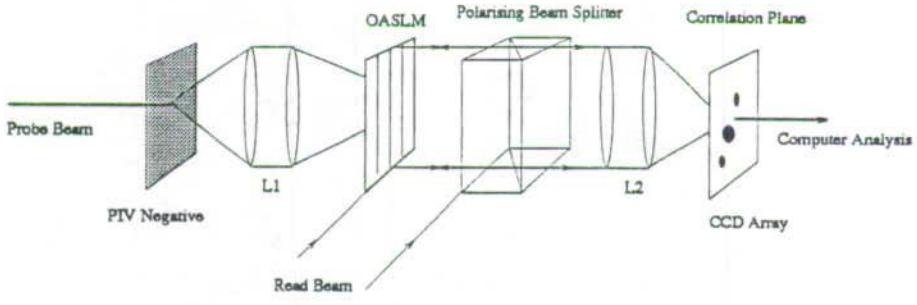

Figure 6.2: PIV Interrogation: Optical Method

6.1.2 Optical-Digital Interrogation (Young's Fringe Method)

This is the traditional method. A doubly exposed photograph is optically Fourier transformed by a lens to form Young's fringes on the CCD camera located in the focal plane of the lens.

The resulting Young's fringes power spectrum is captured by CCD camera, and the information is sent to a microcomputer via a frame store. In the processing, the digitised signal from the CCD is Fourier transformed again by a microcomputer to form the autocorrelation plane (see figure 6.3).

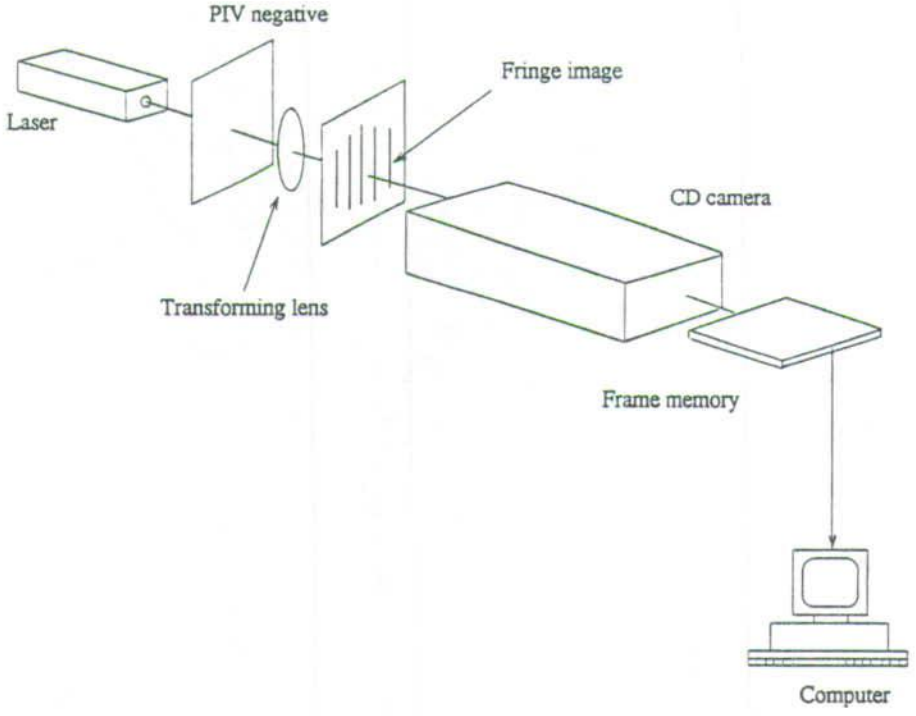

Figure 6.3: PIV Interrogation: Young's fringes Method

The Young's fringe method is particularly suitable for high density seeding.

6.1.3 Digital Interrogation

In this alternative method, the whole, doubly exposed image is digitised making it available in the memory of the computer.

The advantage of the digital method is that it allows for adaptive variation of the interrogation area to optimize spatial resolution and to achieve a wide dynamic range. It can also potentially select particle images from a given intensity range within the whole digitised image so as to analyze certain ranges of particles without interference between signals (suitable in two-phase flows) [50].

Other advantages of full digital processing include:

- Does not require the use of a coherent light source,
- Flexibility and capability of carrying out extra processing such as:
  - corrections for lens distortion or other perspective distortion,
  - Particle counting,
  - Detection of flow boundaries,
  - Subtraction of background images,
  - Aligning of successive frames etc.

Digital processing however is fundamentally many orders of magnitude slower than optical processing.

6.2 PIV Measurement of Dispersion of a Particle Jet

Based on the simplified approach which led to a decision to study the mixing, stability and dispersion of the particle jet/rope using the PIV technique, it was hoped was that some of the basic physical parameters which affect the stability and dispersion characteristics of particle "ropes" could be established.

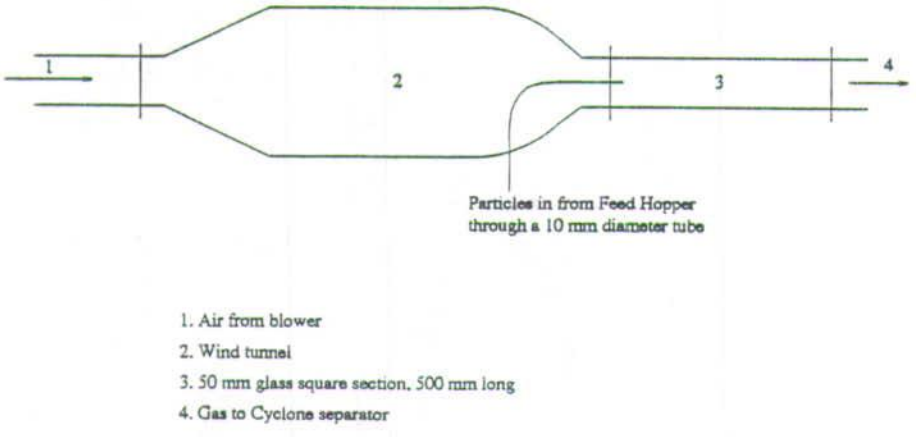

Figure 6.4: Small Wind Tunnel Arrangement

The experiments were done by varying the velocity of the primary air from the blower (stream 1 in figure 6.4) and the velocity of the air picking up the particles. The particle loading (particles to air ratio) was also varied by varying the speed of the hopper feed screw and the velocity of the air transporting the particles. The feed hopper motor was a variable speed one. The main limitation of the rig set up was that the velocity range that gave a stable jet was very narrow and it was thus not possible to explore a wider range of both velocity and particle loadings. In this study, particle loadings of 95 kg/m_3 to 198 kg/m_3 were used compared to 4 kg/m_3 to 40 kg/m_3 used in previous work [83].

The jet was the exposed to a 15W Argon-Iron laser beam. The beam was

expanded to 1 mm thick sheet using an 18 facet spinning mirror whose frequency of spin could be varied from 0 to 450Hz.

The choice up of the frequency of the spinning mirror was based on getting a particle image separation being between 1 mm and 2 mm, so that the negatives could be reliably analysed to get the velocity vectors. The camera exposure time (the time the shutter remained open), T_{exp}, was set such that the physical length of the track of particle images on the negative, $MV_{max}T_{exp}$, was within the minimum separation range i.e. $1\ mm \leq MV_{max}T_{exp} \leq 2\ mm$, where M is the magnification factor which was established experimentaly by photographing a graph paper and measuring the length of the scale on the resulting film negative. The time between successive light flashes or time between exposures, T_s was set up so that it was possible to have four exposure during the the camera exposure time. Thus using the 18 facet spinning mirror and for n film exposures, then the spinning mirror frequency is (see also figure 6.5):

$$\frac{1}{18f} = T_s = \frac{T_{exp}}{n-1} \tag{6.1}$$

Thus for four exposures n is equal to four in the above equation.

Results of some of the experiments done are shown in figures 6.6 to 6.16.

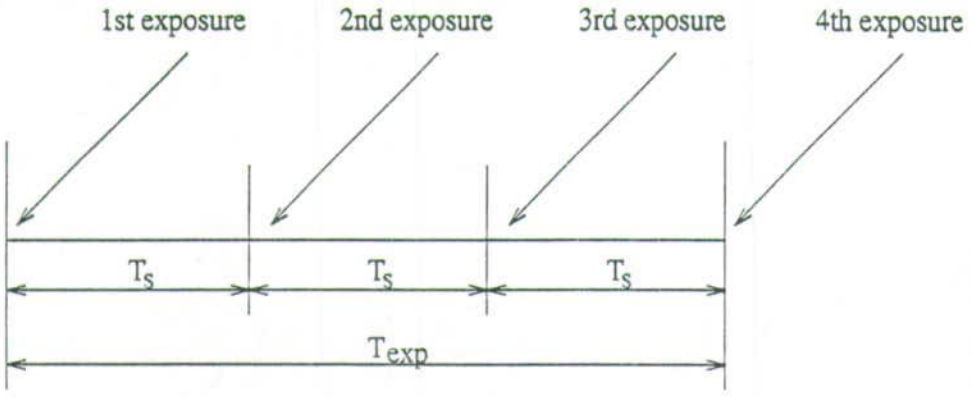

T_s = Time between exposures

T_{exp} = Exposure time

Figure 6.5: Schematic Representation of Time Between Exposures and Exposure Time

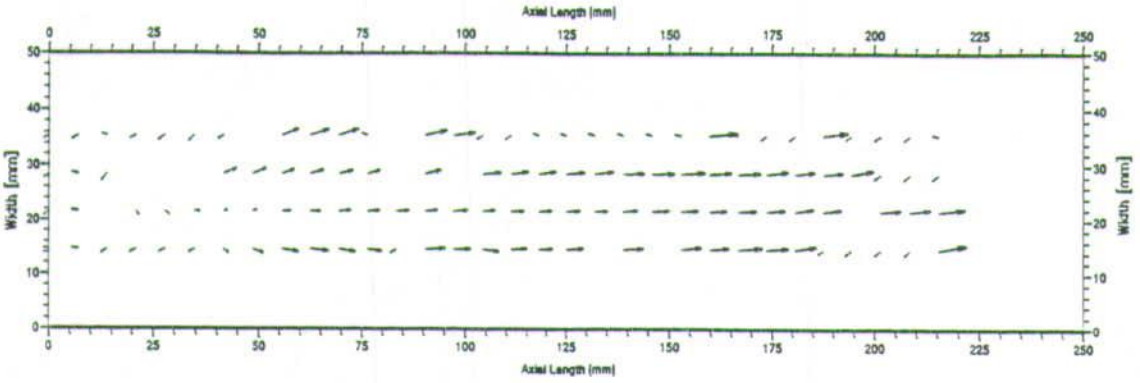

(a) Velocity Vectors (Mean Velocity Subtracted)

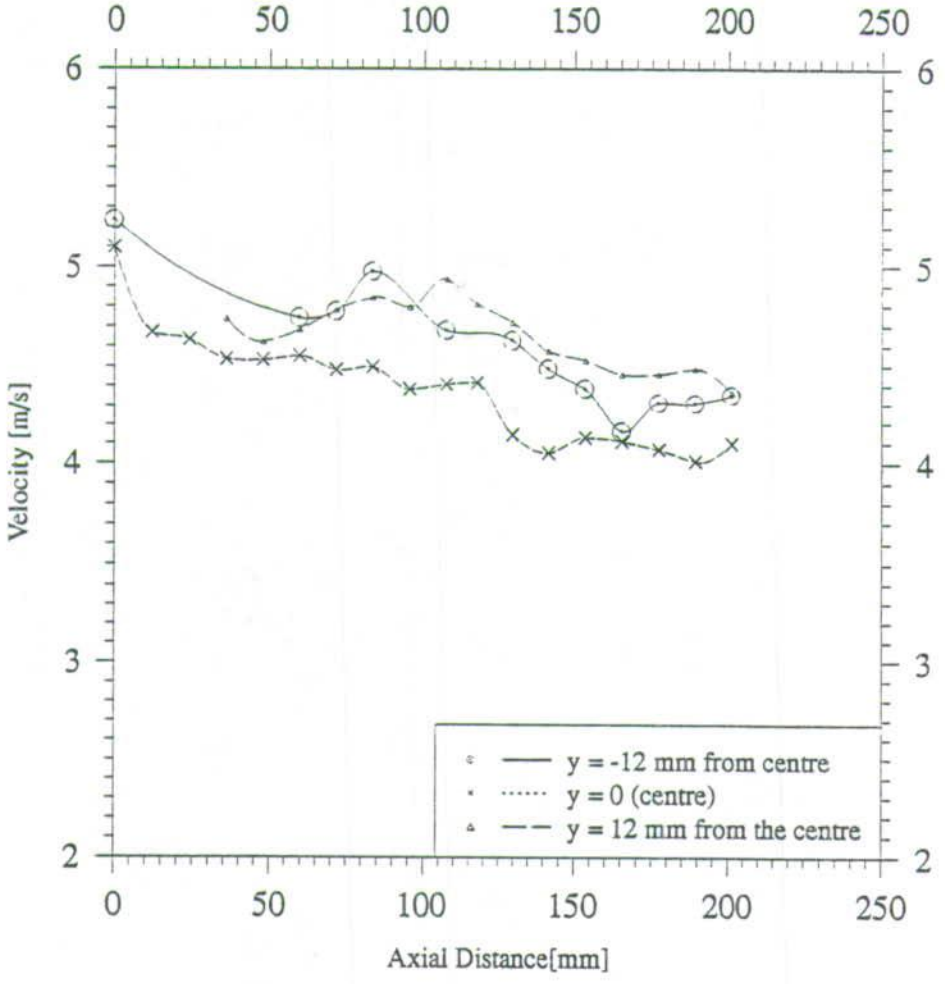

(b) Axial Velocity

Figure 6.6: Primary Air Velocity = 11.4 m/s; Jet Velocity = 9.4 m/s: Particle Jet Density = 190 kgm^{-3}

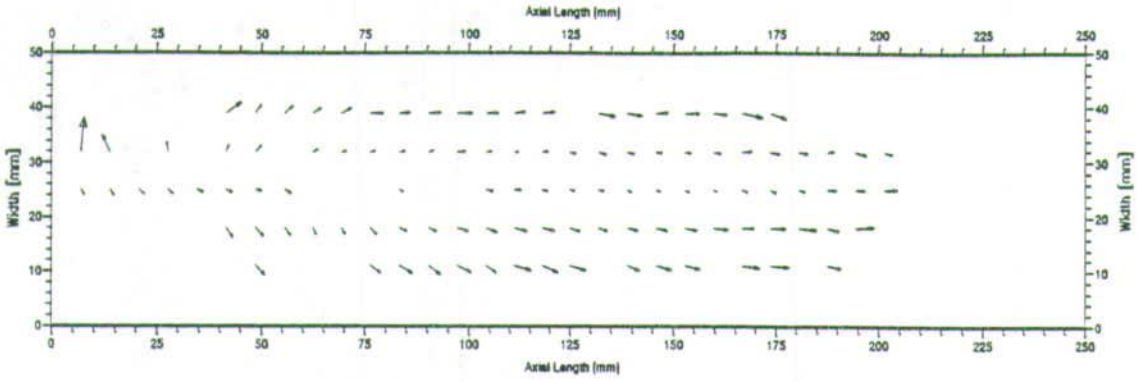

(a) Velocity Vectors (Mean Velocity Subtracted)

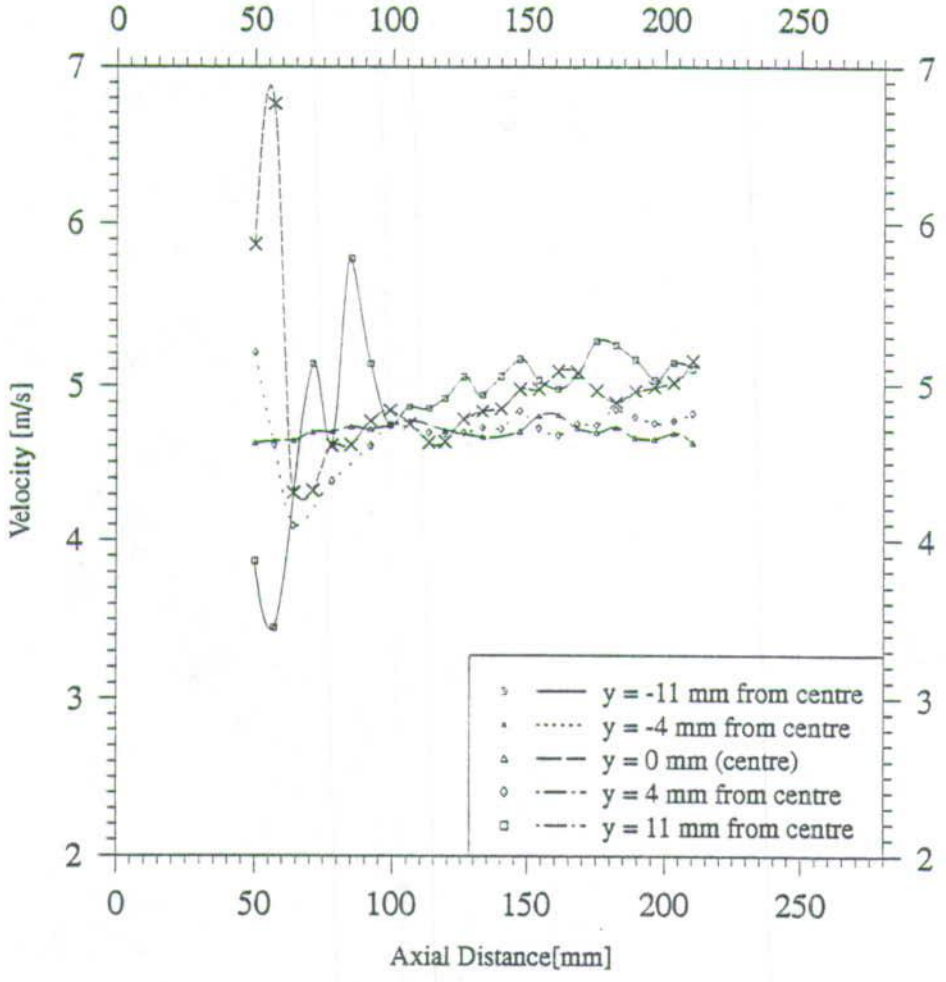

(b) Axial Velocity

Figure 6.7: Primary Air Velocity = 11.4 m/s; Jet Velocity = 9.4 m/s; Particle Jet Density = 169 kgm^{-3}

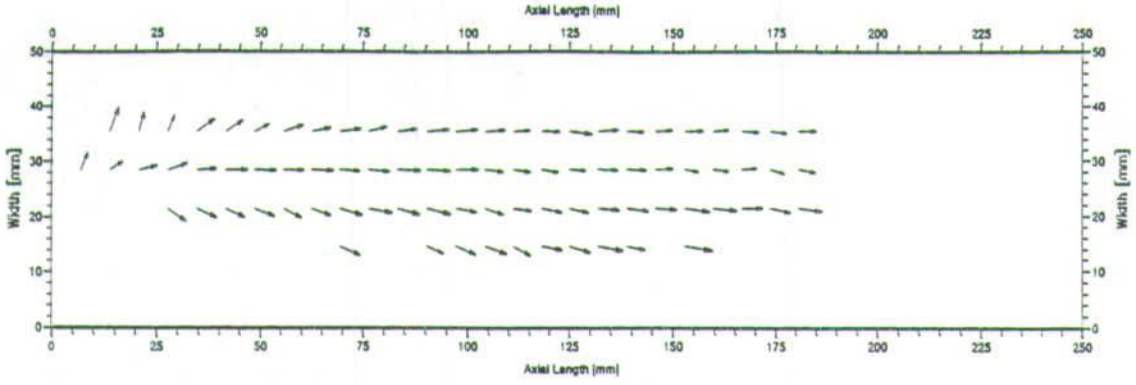

(a) Velocity Vectors (Mean Velocity Subtracted)

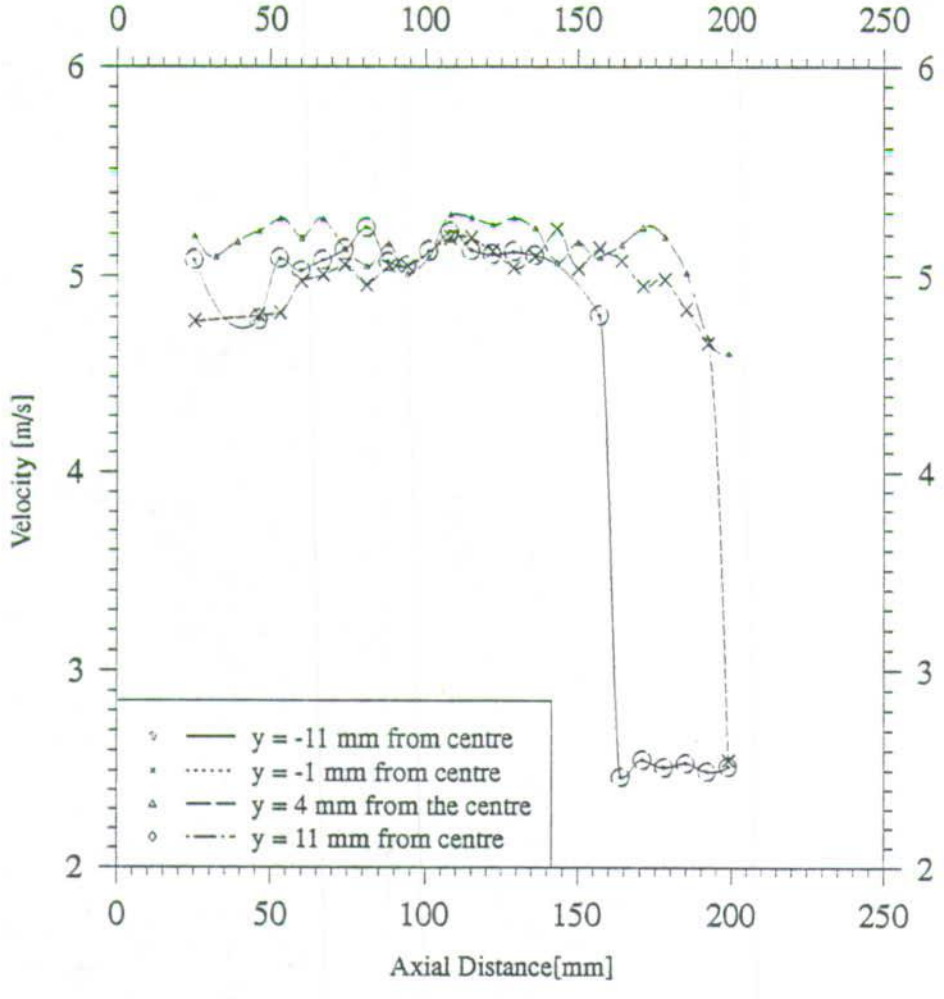

(b) Axial Velocity

Figure 6.8: Primary Air Velocity = 11.4 m/s; Jet Velocity = 9.4 m/s; Particle Jet Density = 135 kgm^{-3}

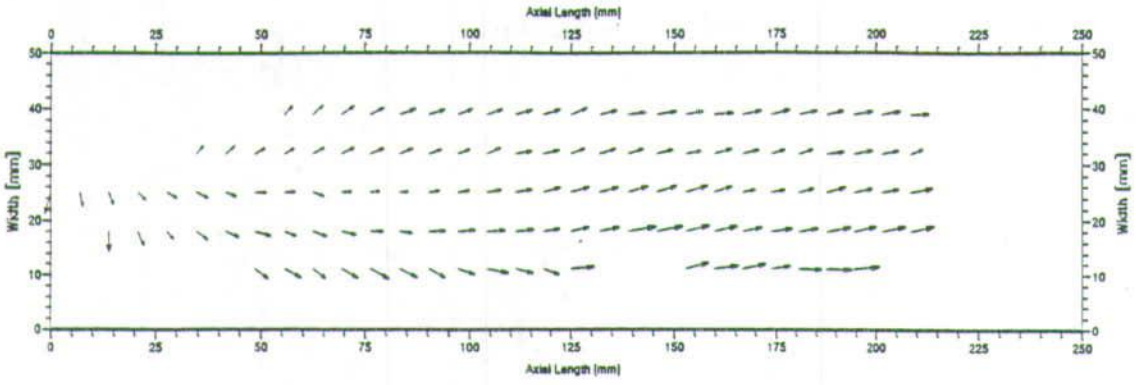

(a) Velocity Vectors (Mean Velocity Subtracted)

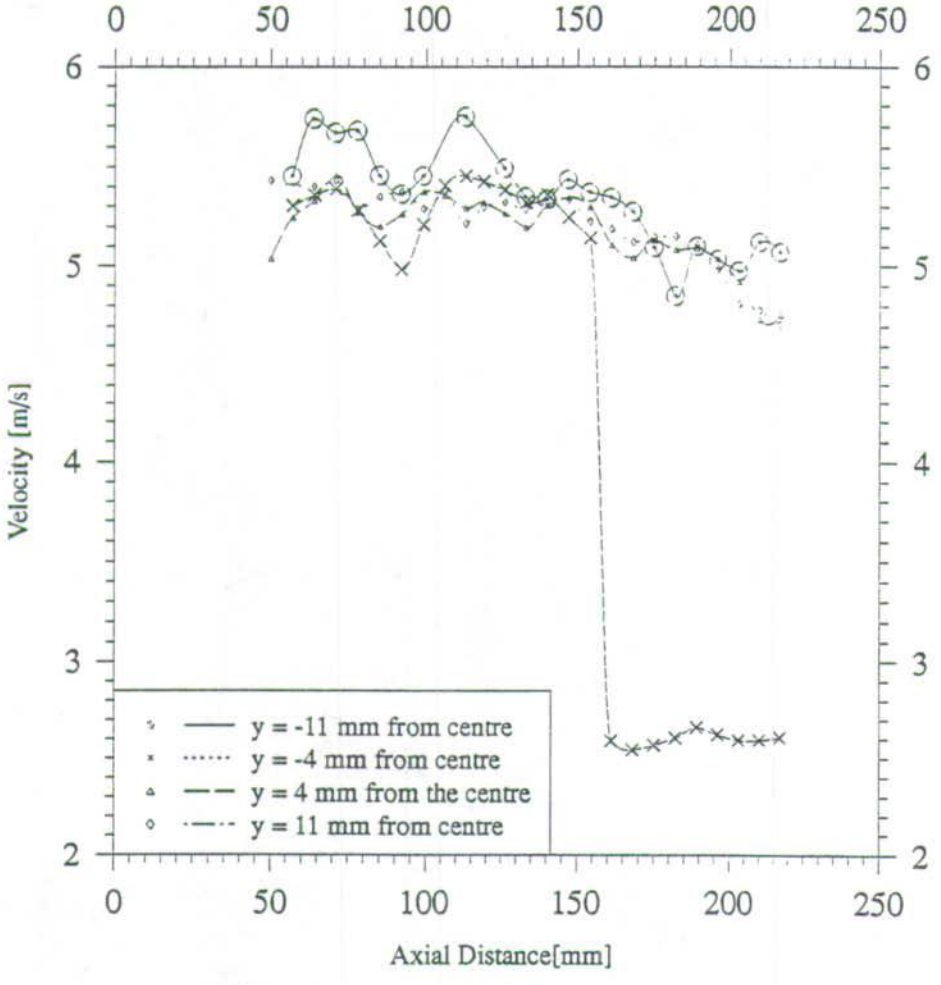

(b) Axial Velocity

Figure 6.9: Primary Air Velocity = 11.4 m/s; Jet Velocity = 9.4 m/s; Particle Jet Density = 95 kgm^{-3}

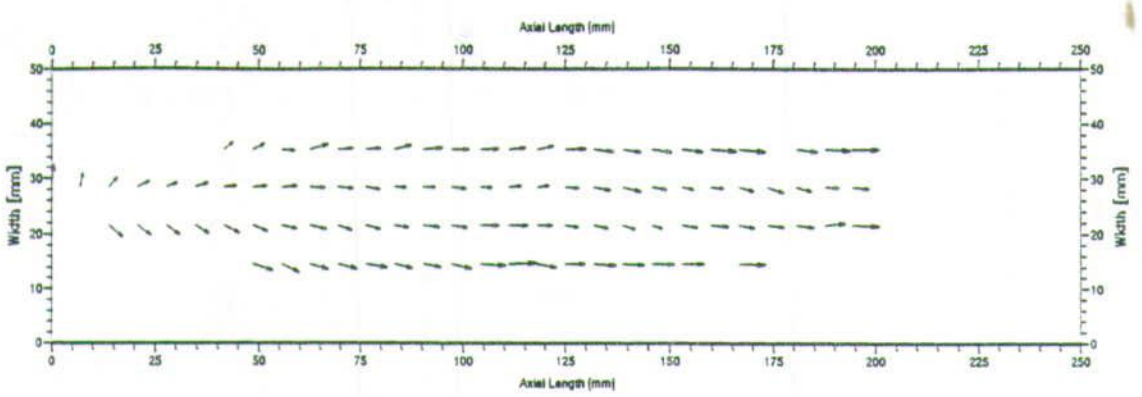

(a) Velocity Vectors (Mean Velocity Subtracted)

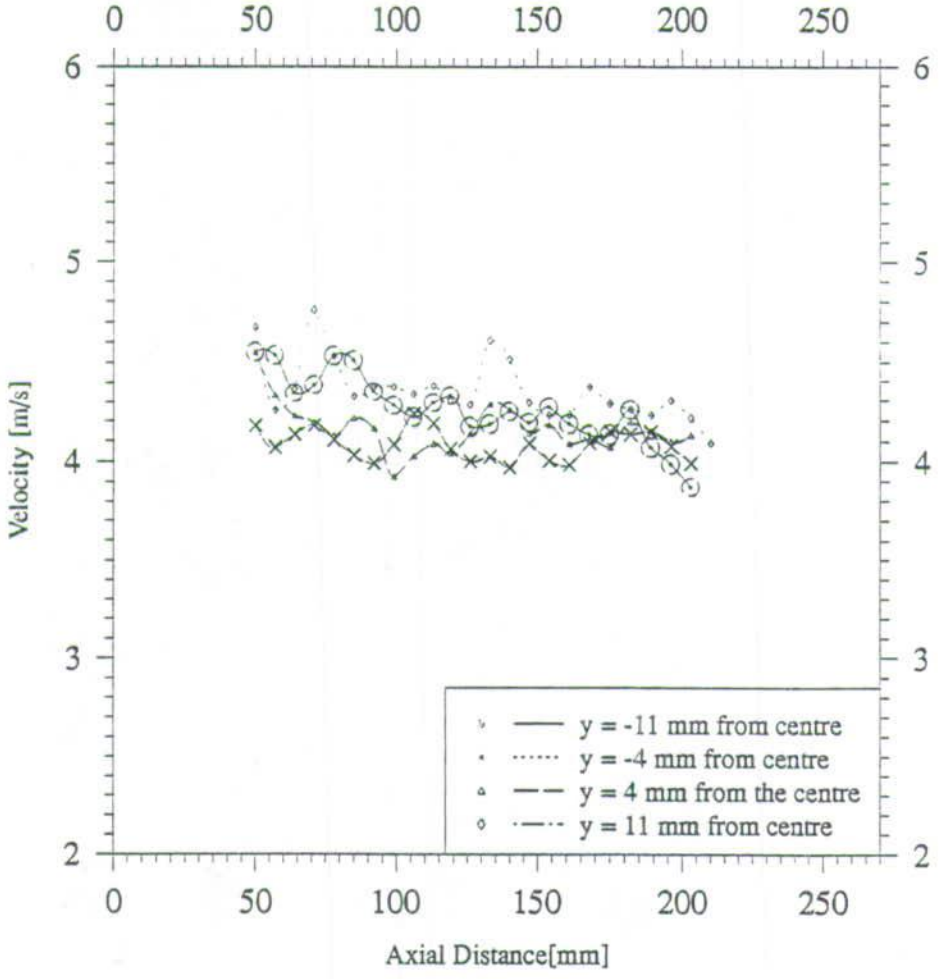

(b) Axial Velocity

Figure 6.10: Primary Air Velocity = 9.1 m/s; Jet Velocity = 9.4 m/s; Particle Jet Density = 189 kgm^{-3}

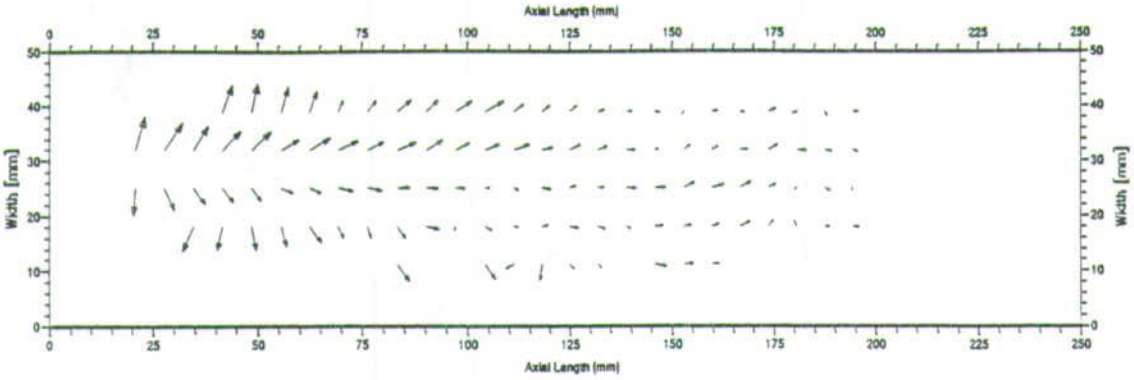

(a) Velocity Vectors (Mean Velocity Subtracted)

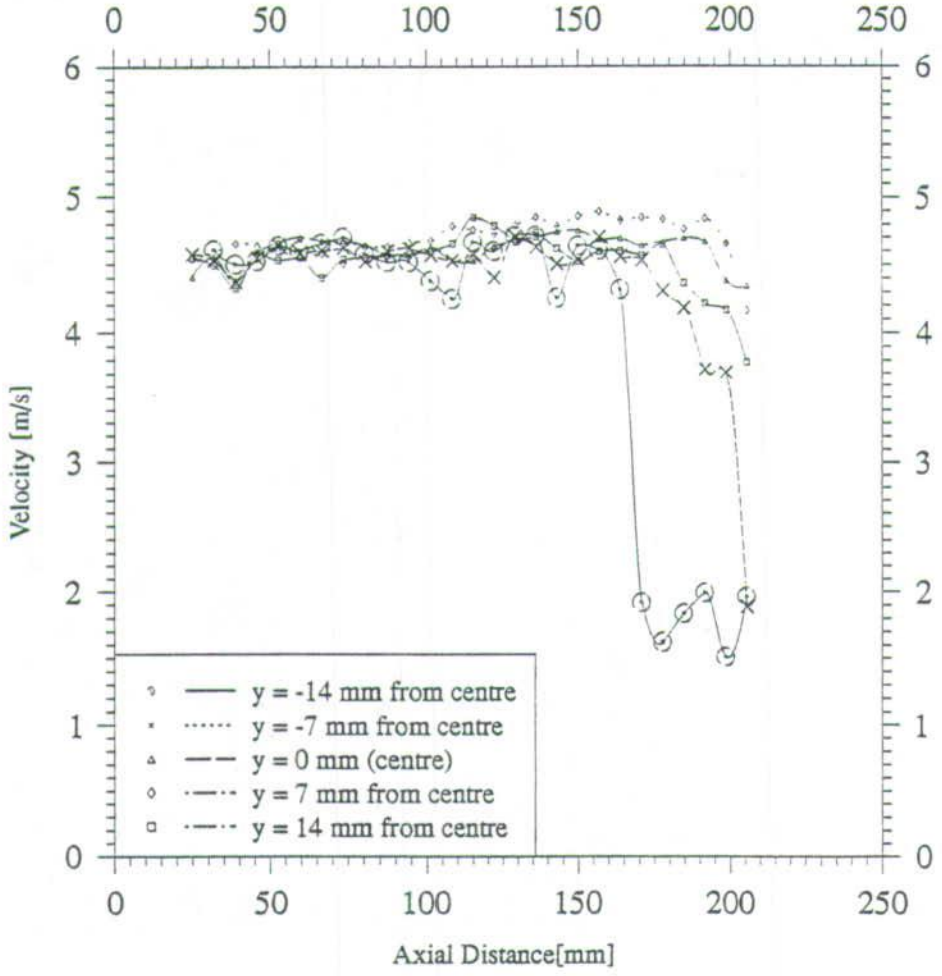

(b) Axial Velocity

Figure 6.11: Primary Air Velocity = 9.1 m/s; Jet Velocity = 9.4 m/s; Particle Jet Density = 135 kgm^{-3}

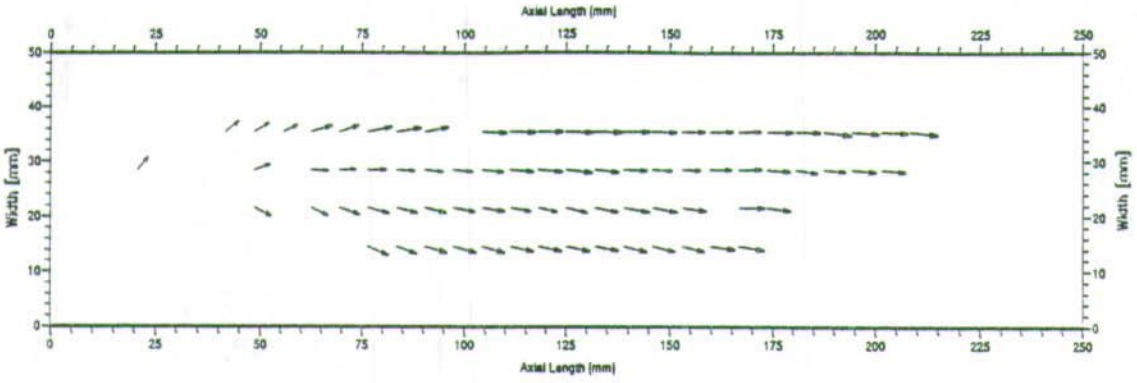

(a) Velocity Vectors (Mean Velocity Subtracted)

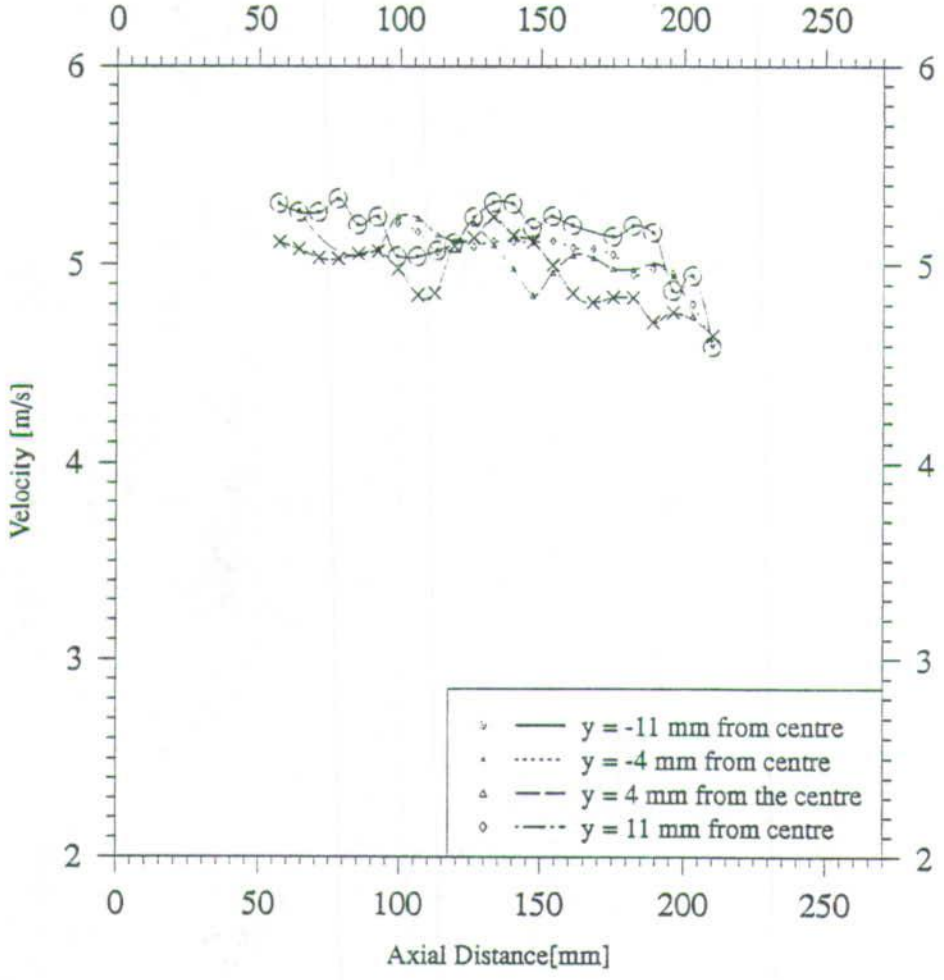

(b) Axial Velocity

Figure 6.12: Primary Air Velocity = 11.4 m/s; Jet Velocity = 10.4 m/s; Particle Jet Density = 171 kgm^{-3}

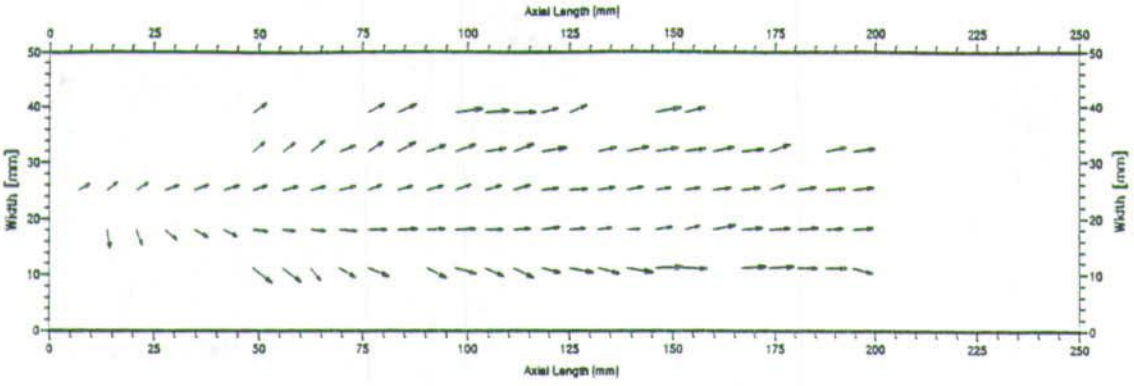

(a) Velocity Vectors (Mean Velocity Subtracted)

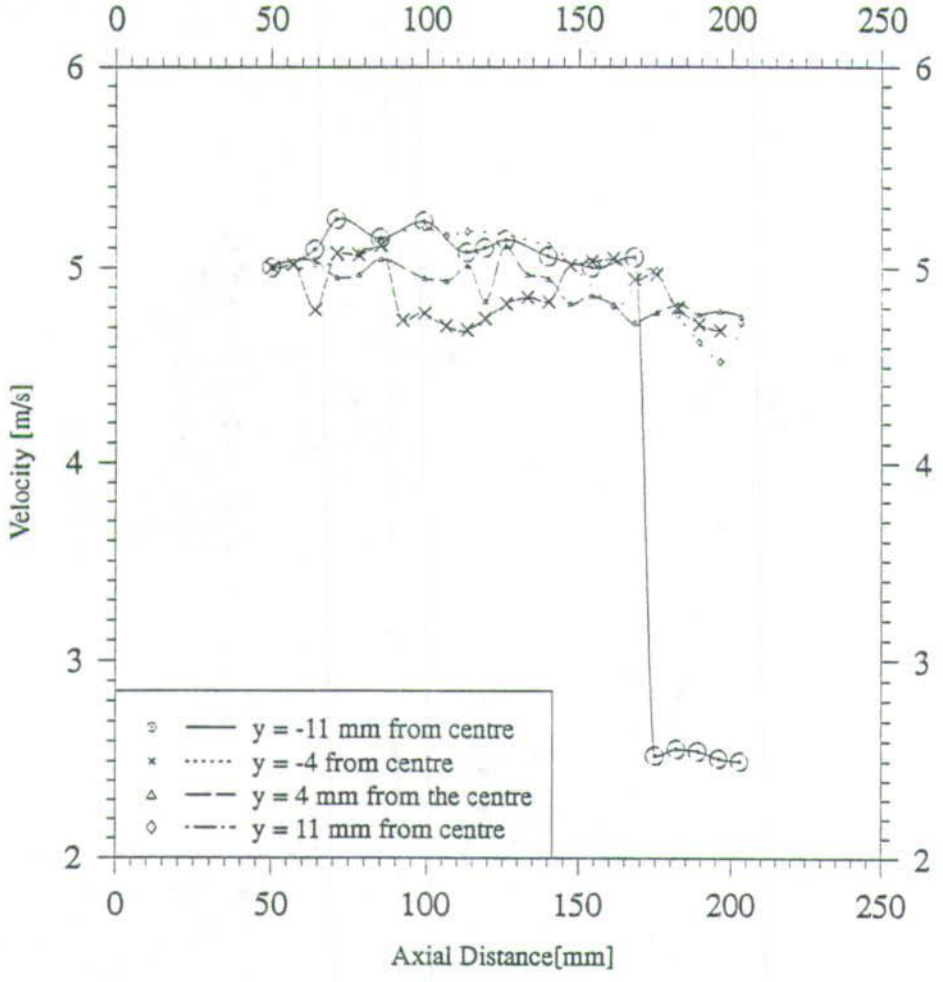

(b) Axial Velocity

Figure 6.13: Primary Air Velocity = 11.4 m/s; Jet Velocity = 10.4 m/s; Particle Jet Density = 147 kgm^{-3}

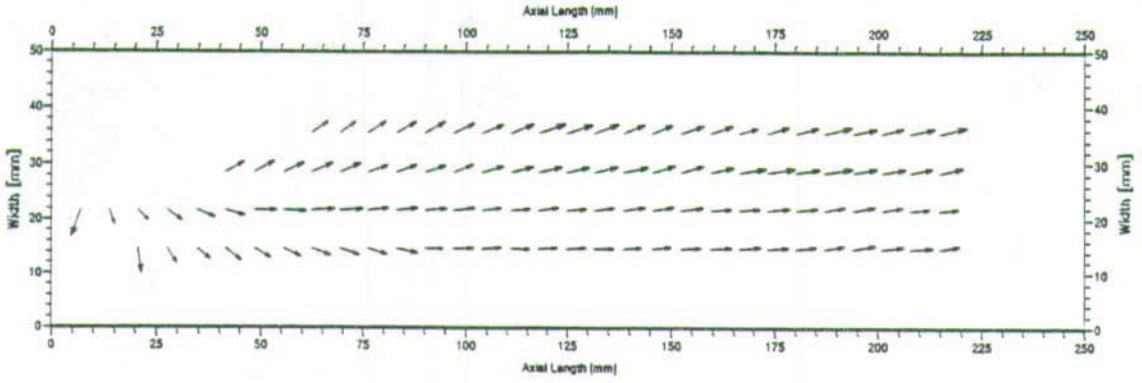

(a) Velocity Vectors (Mean Velocity Subtracted)

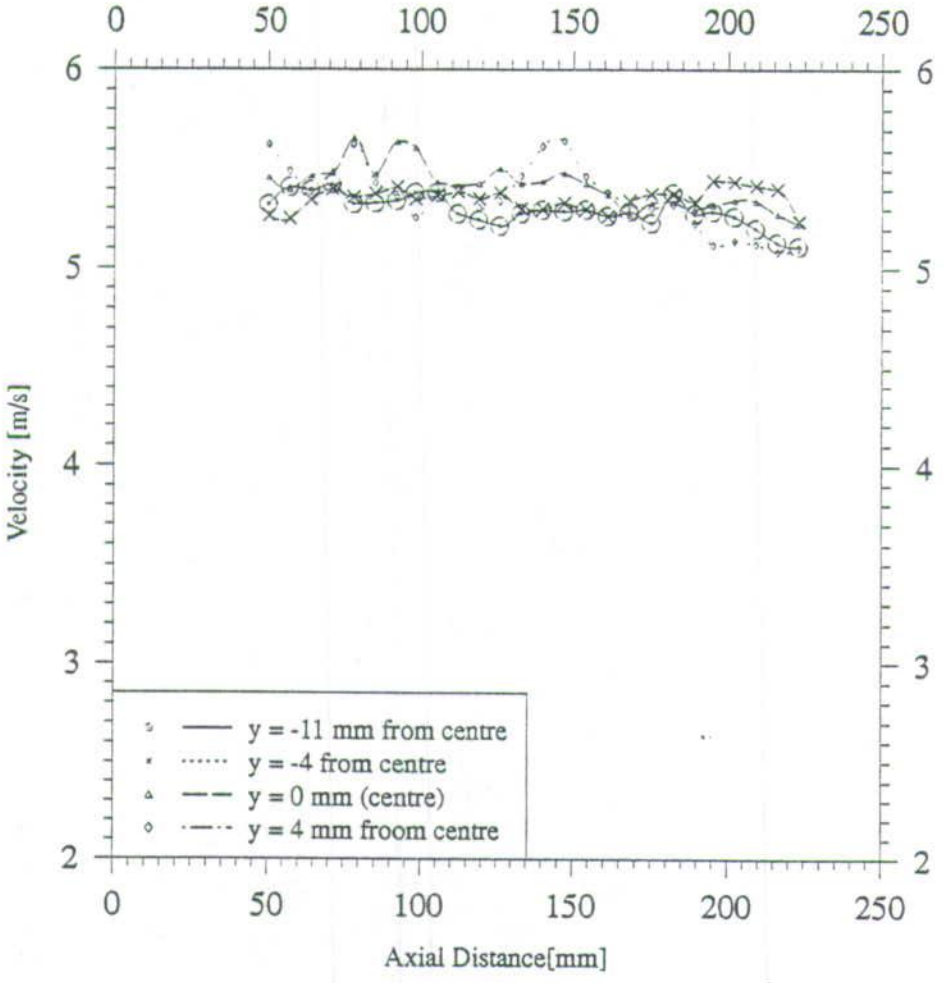

(b) Axial Velocity

Figure 6.14: Primary Air Velocity = 11.4 m/s; Jet Velocity = 10.4 m/s; Particle Jet Density = 110 kgm^{-3}

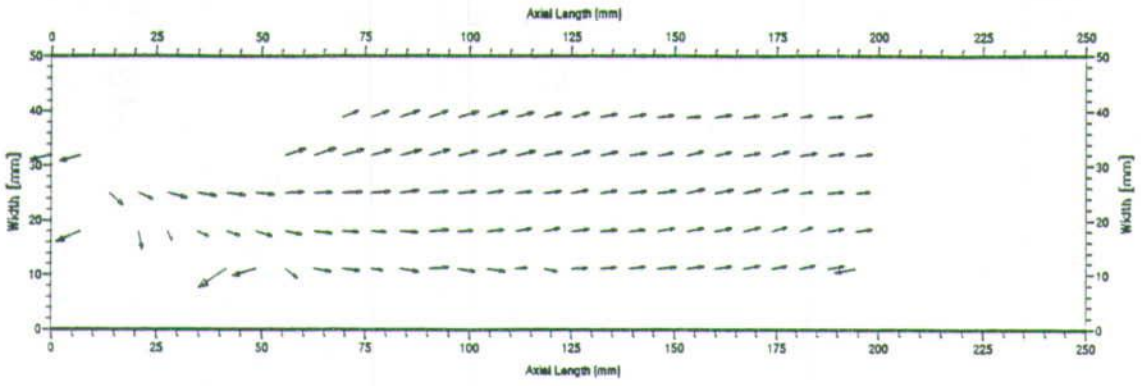

(a) Velocity Vectors (Mean Velocity Subtracted)

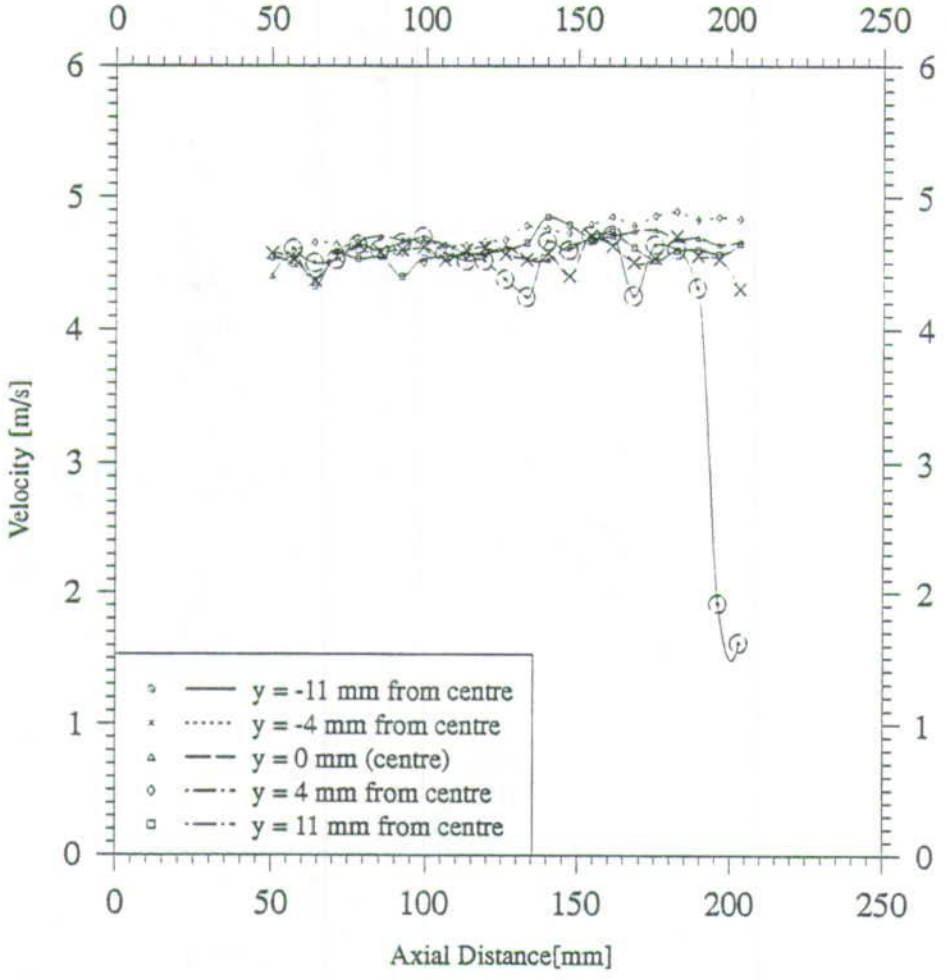

(b) Axial Velocity

Figure 6.15: Primary Air Velocity = 10.4 m/s; Jet Velocity = 9.4 m/s; Particle Jet Density = 95 kgm^{-3}

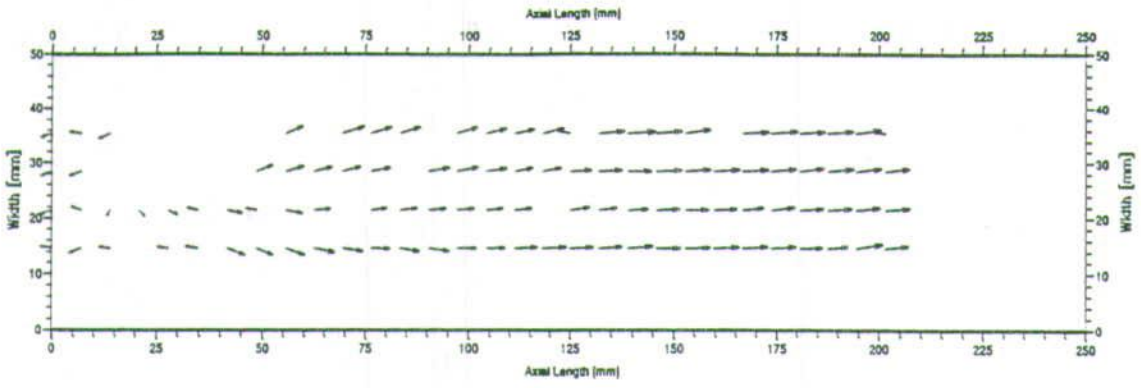

(a) Velocity Vectors (Mean Velocity Subtracted)

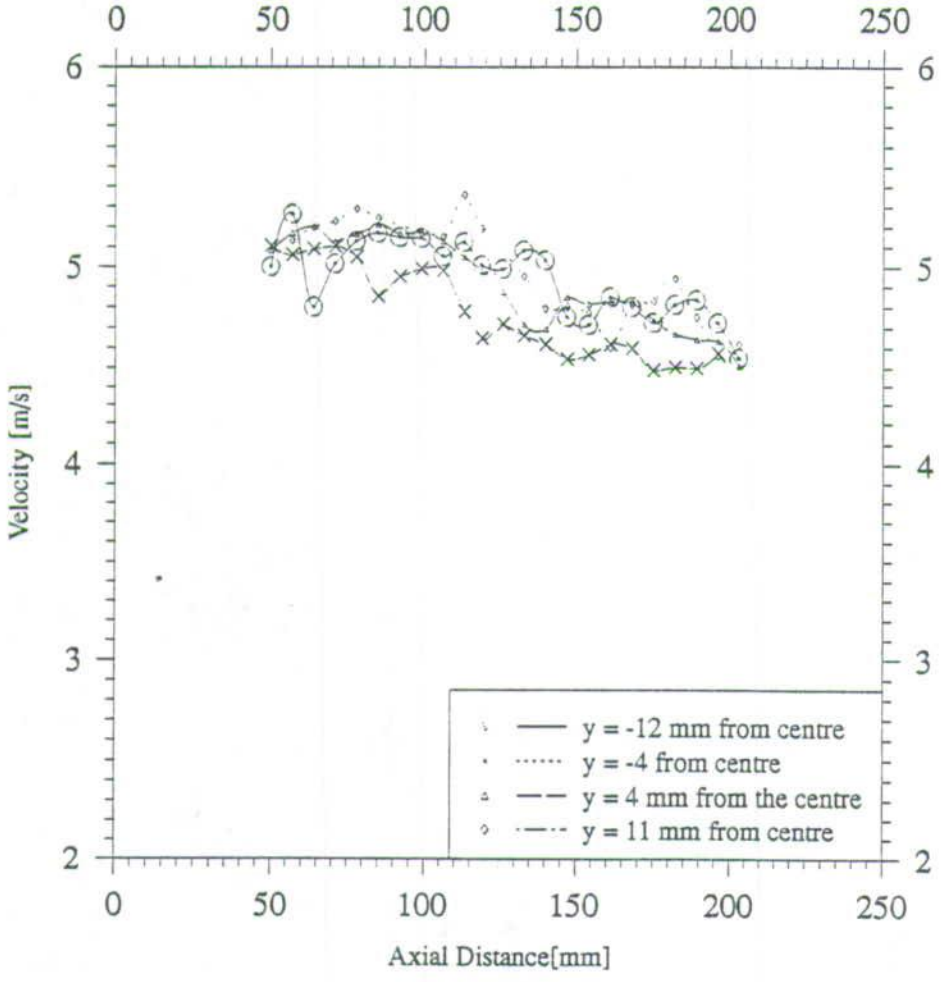

(b) Axial Velocity

Figure 6.16: Primary Air Velocity = 11.4 m/s; Jet Velocity = 9 m/s; Particle Jet Density = 198 kgm^{-3}

6.3 Discussion of PIV Results, Conclusions and Recommendations

The velocity vector plots are that of the particle velocity with the mean axial velocity having been subtracted. The vectors are principally uni-directional confirming the absence of any significant reverse flow or swirling flow except for figure 6.15(a). The vectors can actually be considered as representing instantaneous velocities.

The velocity vector plots 6.6(a) to 6.16(a) do not show any significant difference, this might be due to the fact the velocity range achieved was very narrow. It would be expected that the jet would disperse more quickly when velocity (both the jet and the primary air) was higher or indeed when one of the two streams was at higher velocity. Velocity differentials in this work are in fact all fairly low.

The velocity vectors shows that the jet spreads (particles therefore dispersing). It would be seen that the less dense jet disperses more than the dense jet. This can be judged from the downstream jet width in figures 6.6(a), 6.7(a), 6.8(a) and 6.16(a).

There is however no noticeable inference that can be drawn on the effect of the velocity ratio, again this might be due to the narrow velocity range achieved.

Like in LDA experiments (see page 5.4.2, the velocity fluctuation at the central axis is minimum, figures 6.6(b) to 6.16(b), these plots show the axial velocity at different position across the width of the flow volume. The velocity magnitudes in the caption refer to values calculated from the Pitot-static measurement at the inlet of the respective streams on the basis of inlet pipe area. When the two

streams are of about equal magnitude, the fluctuations are minimum, figures 6.13(b). The dip towards the end of the plot corresponds to positions where a significant deposit of particles occur, visually particles could be seen sitting on the base of the duct, and had the effect of reducing the air flow, see figure 6.17.

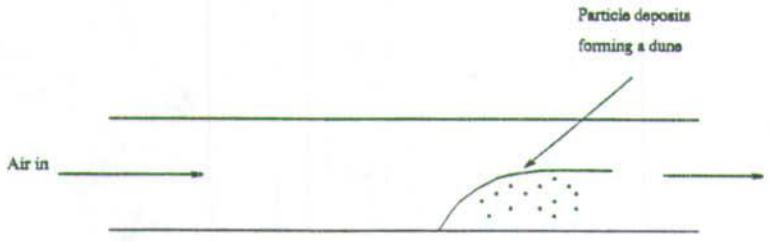

Figure 6.17: Particle Deposition and Dune Formation

The main problem of the experimental set up was that of the particle delivery system. This system had a tendency to deliver an uneven supply of particles which produced an unstable jet of uneven density. Also the velocity range achievable that gave a stable jet was also very narrow. This was due to the fact that the blower delivering air for picking up the particles was not powerful enough.

Additional modification of the particle delivery mechanism might improve the delivery. In the experimental setup, the length of the pipe from the end of the feed screw to the particle pickup point was both too short and had a sharp 90° bend, it was at this point that the pipe tended to get blocked when too much of the particles fell into the pickup column (see figure 6.18). A better mechanism employing an inclined and curved bend of reasonable length might offer smooth flow of the pumped particles (figure 6.19). The curved bend would allow the air to flow more or less straight around the bend picking up the particles. A

powerful blower would still be required.

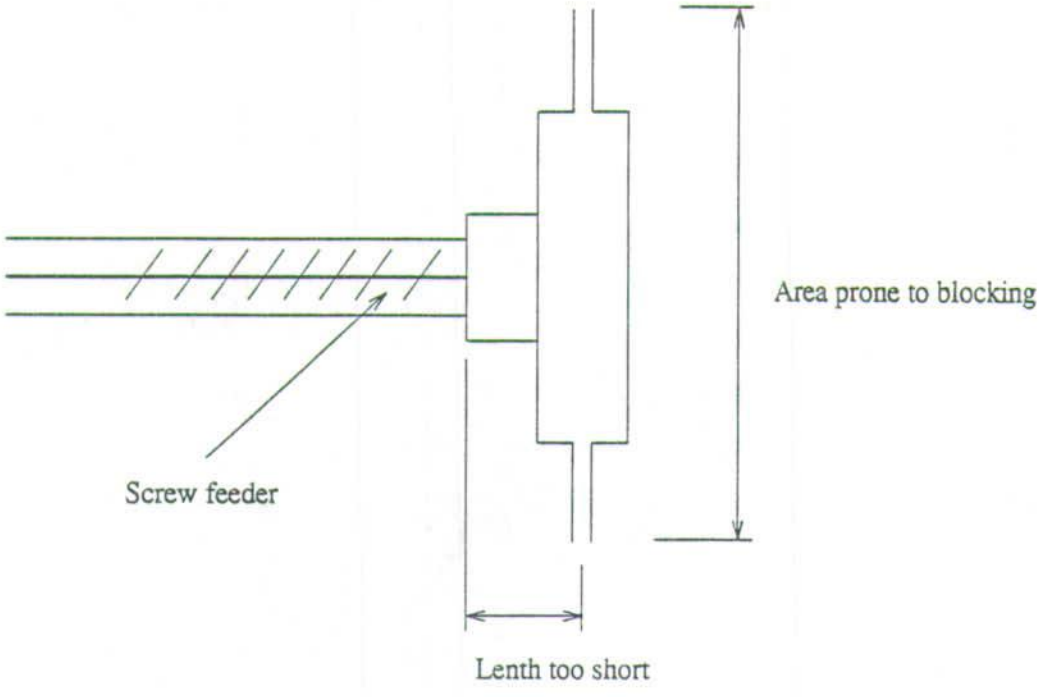

Figure 6.18: Old Particle Feed Mechanism

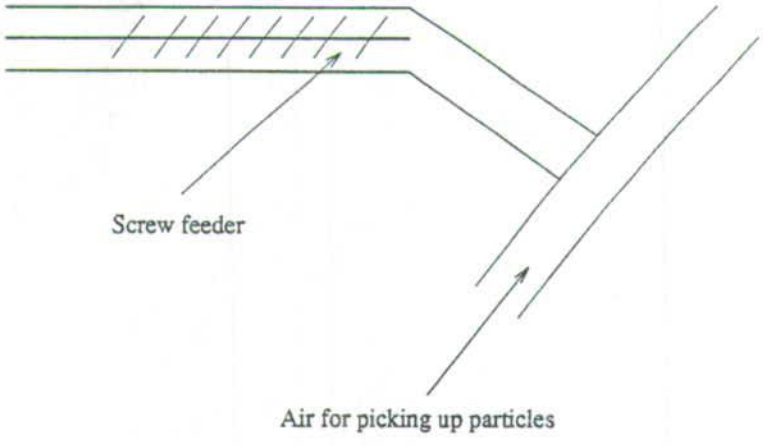

Figure 6.19: Proposed New Particle Feed Mechanism

In conclusion it can be said that the PIV measurement results are consistent with earlier work by McCluskey [83] in which she found that leaner particle jets

dispersed more than the denser ones. Also in agreement is the fact that at high relative velocity with the a high background velocity, there was less dispersion of the particle jet. McCluskey work was based on a much higher differential velocity up 6 times (6 m/s to 40 m/s) but with a low particle jet density of 4 kg/m_3 to 40 kg/m_3. Furthermore, the velocity fluctuations revealed are in agreement with the initial LDA experimental results and simulation results.

The narrow velocity range achieved make it difficult to establish concrete jet dispersion characteristics and more work would need to be done where a wider velocity range will be explored. The rig's particle delivery system will need significant redesign to make sure that a steady stream of particles was delivered to the point where the particles are picked up by the air. This might entail acquiring a new powerful blower.

Chapter 7

Conclusions, Critique & Recommendations

The main objective of the project was to make a fundamental investigation of the basic physical parameters which affect the stability and dispersion characteristics of particle "ropes" and particularly to explore conditions relevant to the design and operation of Low NO_x burners and other similar equipment of industrial interest. The project, though far from being complete, has made reasonable advances in meeting the desired objectives, particularly in:

1. Design and fabrication of the main experimental rig (test facility). This has been completed and is operational. And although there were often conflicting interests regarding the access to the completed facility, I still believe this unit will be an invaluable asset in future research work into two-phase flows. In fact, it has not been sitting idle, but has been in constant use by numerous research workers (from both inside and outside this university).

2. As most flows of practical relevance are always turbulent, the voluminous literature on the subject of turbulence was consulted. The $k-\varepsilon$ model in its many varied forms is the most commonly used and well tested model in modelling single phase fluid flow. This model, when used with proper

boundary conditions to model single-phase flows, normally produces reasonable results. Modelling two-phase flow is more difficult, mainly due to difficulties in selecting a suitable theory. Traditionally, the simulation is done statistically by computing the particle trajectories with the aid of the equations of motion (tracking method). The major draw back of this method is the oversimplification of the equations of motion used.

3. A commercial computational fluids dynamics package called *FLUENT* was used in flow simulation. Single phase flow simulation results were reasonable. However, for two phase simulation (particle injection), the simulation results were not consistent. This might be due to the fact that it is practically difficult to address all the interaction between the complex mechanisms that modify turbulence due to the presence of particles. This includes the reduction of turbulence due to particle acceleration and enhancement of turbulence due to velocity disturbance. There are also, due to some simplifications like neglecting the added mass and volume of particles. *FLUENT* is none the less a useful tool for exploring the flow patterns but sufficient care and experience might be required to interpret the results. The package could be more useful if it could handle polar coordinates as well as it does rectangular ones.

4. Experimental work covered included:

   - Testing/commissioning the experimental rig. Experiments confirmed that the facility was capable of delivering a flow rate of 1100.5 m^3/h at maximum pressure drop (60° swirl generator installed, and both core and annular valves fully open) which is in the same range as the required design flow of 1517.7 m^3/h (see page 89)

- Results from Laser Doppler Anemometer, LDA measurements carried out at several positions across the test section showed that the magnitude of the measured velocity was within the expected velocity range (based on the initial Pitot-static measurements).
- Exploratory measurements of the particle dispersion using the LDA method were made. This method could potentially be improved and can offer a means of making point concentration measurements. The systems needs proper calibration, and a refined timing method, for most personal compters the number of ticks/second offered by the system clock is not normally high enough to offer the high resolution timing required.
- Lastly, the Particle Image Velocimetry (PIV) measurement technique was used to study the dispersion of particle jets of varying density. The results obtained on particle jet dispersion were in good agreement with previous work by McCluskey [83]. Also in agreement was the finding that the center line velocity showed less fluctuation and that jets that are less dense disperse more than the more dense ones. Although he velocity range explored was too narrow to be able to draw more conclusions, the particle jet density explored has been expanded from that of 4 kg/m_{-3} to 40 kg/m_{-3} covered by McCluskey [83] to 95 kg/m_{-3} to 198 kg/m_{-3}.

This preliminary works gives sound background to the basic configuration of Low-NO_x burners, turbulence (both theory and modeling/simulation asppects). The LDA and PIV work are preliminary investigation towards understanding the fluid mechanics of particle "ropes" and the physical reasons for their persistence and eventual breakup.

Appendix A

Table A.1: Some Commonly Available Continuous Wave Lasers

Type	Pumping System	Medium	Principal Wavelength nm	Typical Light Output Power mw
Argon Ion	Electrical discharge	Gas	351.1	50-300
			528.7	100-1000
			488.0	500-5000
Helium-Neon	Electrical discharge	Gas mixture	632.8	1-50
			1152.3	1-10
			3391.2	1-10
Helium-Cadmium	Electrical discharge	Gas-Vapour mixture	325.0	1-10
			441.6	5-40
Tunable Dye	Argon or Krypton Ion laser	Solution of fluorescent dye and	530-590	1000
		Rhodaminedyes	570-650	1000
Neodymium-YAG	Optical with Tungsten halogen or arc lamps	Crystal of Yttrium Aluminium garnet doped with Neodymium	1064	1000-10000

Appendix B

Gas Cyclone Design

This unit was required for recovering the solid particles. The cyclone was designed according to Stairmand's method [24, pages 354 - 360] - see also figure B.1. The performance of the designed cyclone at different flow velocities, recovering particles of different particle sizes and density (was checked and) is summarized in table 4.4. Experiments were also carried out to establish the actual cyclone collection efficiency and are reported under section 4.5

The designed cyclone is shown in figure B.2.

B.1 Cyclone Physical Size and Pressure Drop

The design was based on the cyclone being capable of recovering particles whose mean size is 37.9 μm, density of 2460 kg/m^3 and size distribution given in table B.1, see [10] and [38]. Note that larger particles will settle more quickly than smaller ones.

Stairmand's basic cyclone design data other design data is tabulated table B.2:

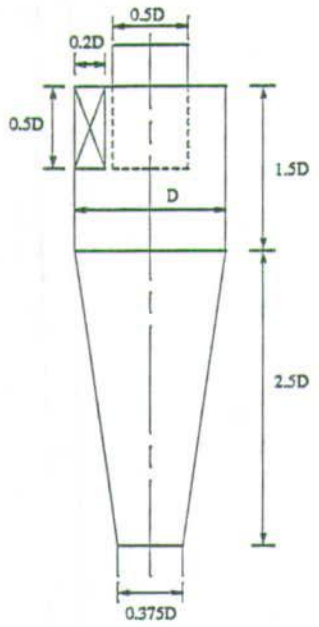

Figure B.1: Sketch of Stairmand High Efficiency Cyclone

The maximum velocity required in a test/measurement section of 101.6 mm diameter was 40 m/s, thus, the design volumetric flow rate, Q_D, scaled up by say 30%, is:

$$Q_D = 40 \times 0.1016^2 \times \frac{\pi}{4} \times 1.3 \times 3600 = 1517.7\, m^3/h$$

Table B.1: Feed Particle Size Distribution (Source Ballotini Ltd. (1990 and Gillispie (1990)

Particle Size μm	106	75	53	38	27	19	13	9.4	6.6	4.7	3.3
% Passing	100	98	89	55.7	21.3	6.3	2.7	0.7	0.1	0.01	0.0

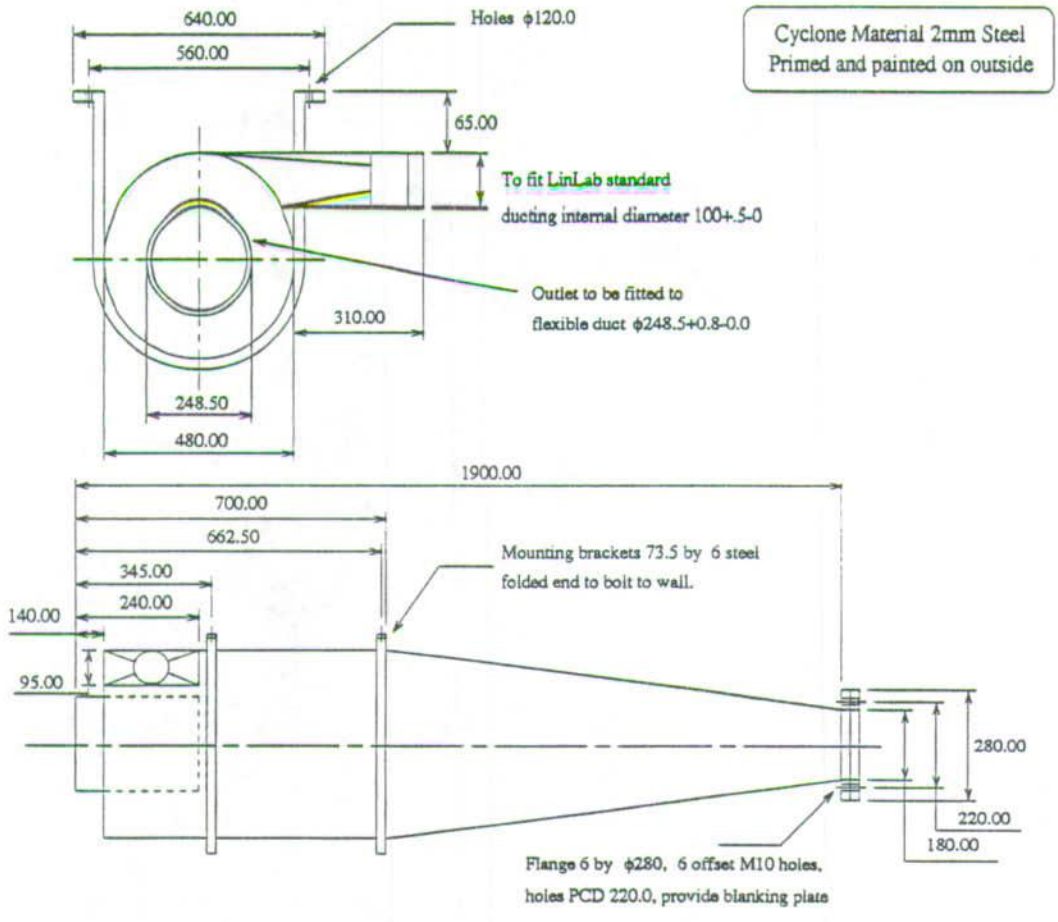

Figure B.2: Designed/Manufactured Cyclone

Table B.2: Basic Cyclone Design Data

	Stairmand's Cyclone	Cyclone Under Design
Cyclone diameter [m]	0.203	D
Volumetric flow rate $[m^3/h]$	223.0	1517.7
Air viscosity [cP]	0.018	0.018
Density Difference $\rho_s - \rho_a\ [kg/m^3]$	2000.0	2458.8

In the Stairmand design method, the recommended gas inlet velocity is between 9 and 27 m/s. Taking the mean (18 m/s) as the design gas inlet velocity into the cyclone, then for the volumetric flow rate of 1517.7 m^3/s, the cyclone inlet area A_1 is:

$$A_1 = 0.5D_c \times 0.2D_c = (1517.7/3600) \div 18 = 0.023\,m^2$$

Thus, the cyclone diameter, $D = \sqrt{0.023/0.1} = 0.48\,m$.

The cyclone exit duct area, A_2 is:

$$A_2 = \frac{\pi}{4}\left(\frac{D}{2}\right)^2 = \frac{\pi}{4} \times \left(\frac{0.48}{2}\right)^2 \approx 0.045m^2$$

The cyclone surface area, A_s is:

$$A_s = \pi D_c(1.5D_c + 2.5D_c) = \pi \times 0.480^2 \times 4 \approx 2.895m^2$$

The cyclone pressure drop factor, ψ, is given by:

$$\psi = f_c \frac{A_s}{A_1}$$

Taking the friction factor, f_c for air, to be 0.005, gives a cyclone pressure drop factor of:

$$\psi = f_c \frac{A_s}{A_1} = 0.005 \times \frac{2.895}{0.023} \approx 0.629$$

and the radius ratio, $\frac{r_t}{r_e} = \frac{D - \frac{0.2 \times D}{2}}{0.5D} = 1.8$.

From figure B.4, for $\frac{r_t}{r_e} = 1.8$ and a cyclone pressure factor, $\psi = 0.629$ gives factor, ϕ in figure B.3 $\approx$ 0.9. With the cyclone inlet velocity = (1517.7/3600) $\div$ 0.023 = 18.3 m/s and the cyclone exit velocity = (1517.7/3600) $\div$ 0.045 = 9.4 m/s, then the cyclone pressure drop, ΔP_c, is:

$$\Delta P_c = \frac{\rho_a}{203}\left[u_1^2(1 + 2\phi^2(2\frac{r_t}{r_e} - 1)) + 2u_2^2\right]$$

i.e. $\Delta P_c = \frac{1.2}{203}\left[18.3^2(1 + 2 \times 0.9^2(2 \times 1.8 - 1)) + 2 \times 9.4^2\right] \approx 11.4$ mbar.

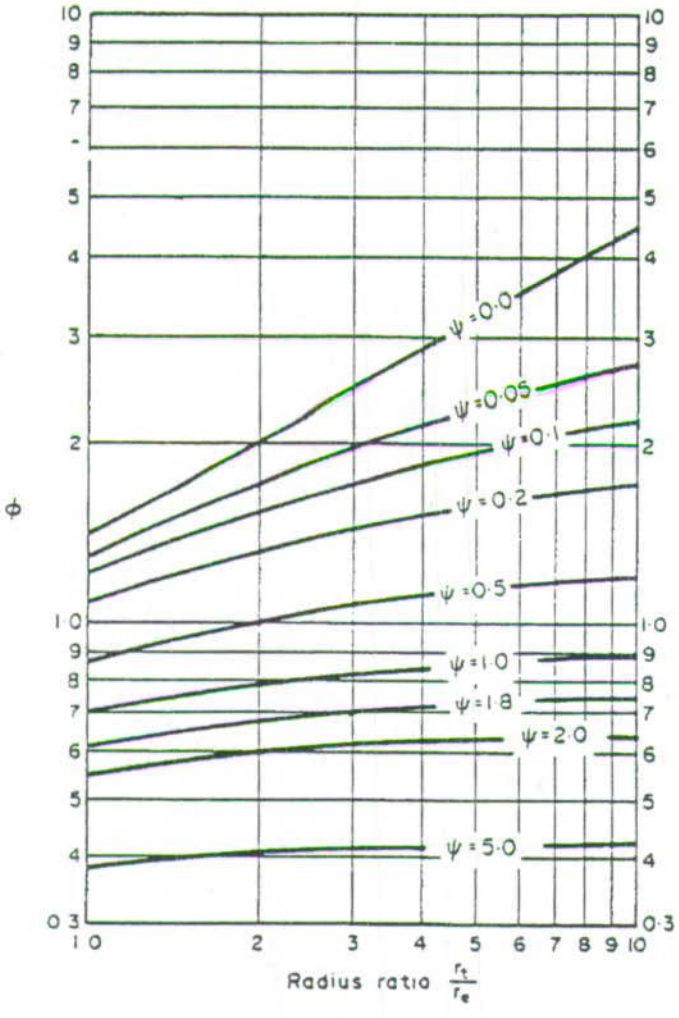

Figure B.3: Cyclone Pressure Drop Factor Factor (Reproduced from figure 10.48 [24, page 357])

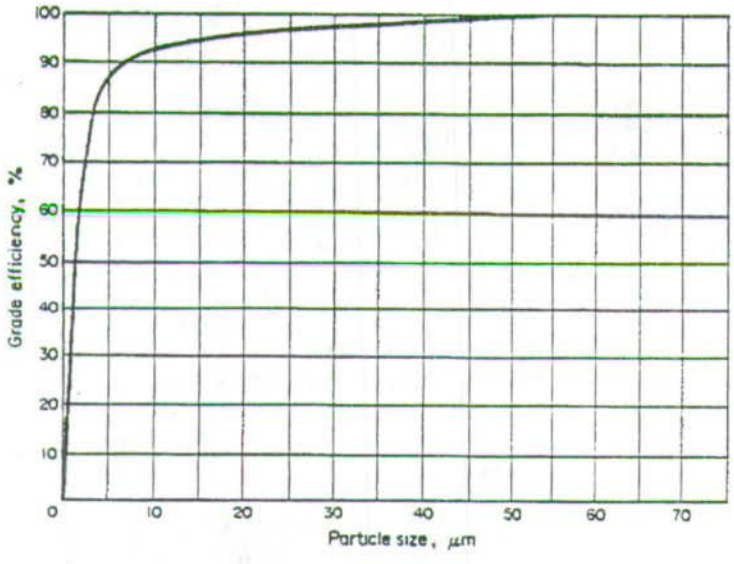

Figure B.4: Stairmand's High Efficiency Cyclone (Reproduced from figure 10.46 [24, page 357])

Bibliography

[1] D. G. Lilley A. K. Gupta and N. Syred. *Swirl Flows.* Abacus Press, 1974.

[2] A. Berlemont A. Picart and G. Gouesbet. Modelling and Predicting Turbulence Fields and the Dispersion of Discrete Particles Transported by Turbulent Flows. *International Journal of Multiphase Flow*, 12(2):237–261, 1986.

[3] G. N. Abramovich. *The Theory Of Turbulent Jets.* The M.I.T. Press, 1963.

[4] R. J. Adrian. Multi-point Optical Measurement of Simultaneous Vectors in Unsteady Flow - A Review. *International Journal of Heat and Fluid Flow*, 7(2):127–145, June 1986.

[5] R. J. Adrian and Yao. Application of Pulsed Laser Technique to Liquid and Gaseous Flows and Scattering Power of Seed Materials. In *Second Symposium on Application of Laser Anemometry to Fluid Mechanics*, Lisbon, Portugal., 1984.

[6] Ronald J. Adrian. Image Shifting Technique to Resolve Directional Ambiguity in Double-Pulsed Velocimetry. *Applied Optics*, 25(21):3855–3858, November 1986.

[7] D. Albagli and Y. Levy. Two-Phase Flow Measurements in Confined Coaxial Jets. *International Journal of Multiphase Flow*, 16(5):929–932, 1990.

[8] E. Archibold and E. Ennos. Displacement Measurement From Double-Exposure Laser Photographs. *Optica Acta*, 19(4):253–271, 1972.

[9] Christopher J. D. Pickering Atsushi Kirita and Neil A. Halliwell. Particle Image Velocimetry: Automatic fringe Analysis by Cross Correlation. *Optical Engineering*, 27(3):188–192, March 1988.

[10] Potter Ballotini(Ltd.). Uncoated Soda Lime Glass (Spheriglass 3000 CP00). Manufacturer's data sheet, Potter Ballotini Ltd., 1990.

[11] D. Barker and M. E. Fourney. Measuring Fluid Velocities with Speckle Patterns. *Optics Letters*, 1(4):135–137, October 1977.

[12] J. M. Beér and N. A. Chigier. *Combustion Aerodynamics*, chapter 2 and 5. Applied Science Publishers Ltd., 1972.

[13] R. J. Adrian C. C. Landreth and C. S. Yao. Double Pulsed Particle Image Velocimeter with Directional Resolution for Complex Flows. *Experiments in Fluids*, 6:119–128, 1988.

[14] D. Skyner C. Gray and C. A. Greated. The Measurement of Breaking Waves Using particle Image Velocimetry. *ICALEO*, 67:166–177, 1987.

[15] J. P. Sharpe C. Gray and C. A. Greated. Fringe Analysis For PIV Measurements In Acoustic Streaming. In *Fringe Analysis 89*, Fringe Analysis, Loughborough, U.K., 1989.

[16] W. J. Easson C. Gray, C. A. Greated and M. G. Fancey. The Application of PIV to the Measurement Under Water Waves. In 2^{nd} *International Conference On Laser Anemometry*, International Conference On Laser Anemometry, Strathclyde, Scotland, 1987.

[17] C. J. Call and I. M. Kennedy. Measurements and Simulations of Particle Dispersion in a Turbulent Flow. *International Journal of Multiphase Flow*, 18(6):811–903, 1992.

[18] J. N. Chung and T. R. Troutt. Simulation of Particle Dispersion in an Axisymmetric Jet. *Journal of Fluid Mechanics*, 186:199–222, 1988.

[19] L. Clarke and R. L. Davidson. *Manual For Chemical Engineering Calculations.* McGraw-Hill Book Company, inc., second edition, 1962.

[20] Steven H. Collicott and Lambertus Hesselink. Anamorphic Optical Processing of Multiple-Exposure Speckle Photography. *Optics Letters*, 11(7):410–412, July 1986.

[21] J. M. Coulson and J. F. Richardson. *Chemical Engineering*, volume 1 of *Chemical Engineering.* Pergamon Press, 3^{rd} edition, 1977.

[22] J. M. Coulson and J. F. Richardson. *Chemical Engineering*, volume One. Pergamon Press, third edition, 1977.

[23] Jeremy M. Coupland and Christopher J. D. Pickering. Particle Image Velocimetry: The Ambiguity Problem. *Optical Engineering*, 27(23):193–196, March 1988.

[24] S. C. Hunter D. J. Mormile, S. E. Kerho and P. E. Coffey. No_x Inventory and Retrofit Assessment. In *Symposium on Stationary Combustion NO_x Control CS-4360*, EPRI, 1985.

[25] J. B. Chen D. W. Li and F. P. Chiang. Statistical Analysis of One Beam Subjective Laser-Speckle Interferometry. *Journal of Optical Society of America*, 2(5):657–666, May 1985.

[26] Ezzat D. Doss. Analysis and Application of Solid-Gas Flow Inside a Venturi With Particle Interaction. *International Journal of Multiphase Flow*, 11(4):445–458, 1985.

[27] D. Dudderar and P. G. Simpkins. Laser Speckle Photography in Fluid Medium. *Nature*, 270:45–47, November 1977.

[28] T. S. Durani and C. Greated. Statistical Analysis of Velocity Measuring Systems Employing the Photon. *IEEE Transaction on Aerospace and Electronic Systems*, AES-10(1):17–24, January 1974.

[29] J. M. Burch E. Archibold and E. Ennos. Recording of In-plane Surface Displacement by Double Exposure Speckle Photography. *Optica Acta*, 17(12):883–898, 1970.

[30] J. W. Elsner and S. Drobniak. Turbulence Structure in Swirling Jet. In *Structure of Complex Turbulent Shear Flow Symposium*, IUTAM, pages 219–228, Marseille, France, 1982. Springer Bérlin Heilderberg.

[31] A. E. Ennos. Speckle Interferometry. *E. Wolf Progress in Optics*, xvi:234–287, 1978.

[32] R Erbeck and W. Merzkirch. Speckle Photographic Measurement of Turbulence in an Air Stream with Fluctuating Temperature. *Experiments in Fluids*, 6:89–93, 1988.

[33] David M. W. Evans. A Second Improved Digit-Reversal Permutation Algorithm for Fast Transforms. *IEEE Transactions on Acoustics, Speech, and Signal Processing*, 37(8):1288–1291, August 1989.

[34] B. C. R. Ewan. Particle Velocity Distribution by Holography. *Applied Optics*, 18(18):3156–3160, September 1979.

[35] M Short G. A. Reynolds and M. C. Whiffen. Automated Reduction of Instantaneous Flow Fields. *Optical Engineering*, 24(3):475–479, May/June 1985.

[36] Y. Kwan G. England and R. Payne. Development and Field-Demonstration of a Low-NO_x Burner For TOER Steamers. In *Symposium on Stationary Combustion NO_x Control CS-4360*, EPRI, 1985.

[37] P. R. Garabedian. *Partial Differential Equations.* John Wiley & Sons, Inc., 1964.

[38] J. Gillispie. Spheriglass 3000 CP00 Size Distribution. Babcock enginering ltd. internal experimental results, Babcock Enginering Ltd., Glasgow, Scotland, March 1990.

[39] S. Goldstein. *Modern Developments In Fluid Dynamics*, volume 1. Dover Publications, Inc., 1965.

[40] S. Goldstein. *Modern Developments In Fluid Dynamics*, volume 2. Dover Publications, Inc., 1965.

[41] R. A. Gore and C. T. Crowe. Effect of Particle Size on Modulating Turbulent Intensity. *International Journal of Multiphase Flow*, 15:279–285, 1989.

[42] S. M. Gorlin and I. I. Slesinger. *Wind Tunnels and Their Instrumentaion.* Israel Program for Scientific Translations, 1966.

[43] C. Gray. The evolution of particle image velocimetry. In *Optical Methods and Data Processing in Heat and Fluid Flow*, IMechE Symposium, London, UK, 1992.

[44] C Gray and C. Greated. The Application of Particle Image Velocimetry to the Study of Water Waves. *Optics and Lasers in Engineering*, 9:265–276, 1988.

[45] Callum Gray. PIV. Second year phd report, Edinburgh University, June 1988.

[46] C. Greated. Measurement of Turbulent Statistics With a Laser Velocimeter. *Journal of Physics E: Scientific Instruments*, 3:158–160, 1970.

[47] C. Greated. Resolution and Back Scattering Optical Geometry by Laser Doppler System. *Journal of Physics E: Scientific Instruments*, 4:585–588, 1971.

[48] Johan Groth and Arne V. Johansson. Turbulence Reduction by Screens. *Journal of Fluid Mechanics*, 197:139–155, 000.

[49] D. G. Lilley A. K. Gupta and N. Syred. *Swirl Flows.* Abacus Press, 1974.

[50] A. K. Hind and J. R. E. Christy. Digital PIV Applied toFlows Around Artificial Heart Valves: Analysis by Autocorrelation. In *Proceeding of Euromech Colloquim 279*. Kluwer Academic Publishers, The Netherlands, 1992.

[51] J. O. Hinze. *Turbulence*. McGrawhill Book Company Inc, 1959.

[52] G. J. Hokenson and J. A. Schetz. Free Turbulent Mixing in Axial Pressure Gradients. *Journal of Applied Mechanics*, pages 375–380, June 1973.

[53] J. M. Huntley. An Image Processing System for the Analysis of Speckle Photographs. *Journal of Physics E: Scientific Instruments*, 19:43–39, 1986.

[54] J. M. Huntley. Speckle Photography Fringe Analysis by the Walsh Transform. *Applied Optics*, 25(3):382–386, February 1986.

[55] Creare Incorporated. *FLUENT* User Manual. Technical report, Creare Incorporated., 1987.

[56] S. A Isacson and Guillermo H. Kaufmann. Two Dimensional Digital Processing of Speckle Photography Fringes. 1: Diffraction Halo Influence for Noise-free Case. *Applied Optics*, 24(2):189–192, January 1985.

[57] Saul A. Isacson and Guillermo H. Kaufmann. Two Dimensional Digital Processing of speckle Photography Fringes. 2: Diffraction Halo Influence for the Noisy Case. *Applied Optics*, 24(10):1444–1447, May 1985.

[58] K. Itishida, A. Ando, and M. Maeda. Experiments on Particle Dispesrsion in a Turbulent Mixibg Layer. *International Journal of Multiphase Flow*, 18(2):181–194, 1992.

[59] T. W. Lester J. C. Kramlich and J. O. Wendt. Mechanisms of Nitrogen Reduction In Pulverised Coal Flames. In *Symposium on Stationary Combustion NO_x Control CS-4360*, EPRI, 1985.

[60] E. Jakeman. Speckle Statistics with a Small Number of Scatterers. *Optical Engineering*, 23(4):483–461, July 1984.

[61] D. D. Joseph and T. S. Lundgren. Ensemble Averaged and Mixture Theory Equations for Incompressible Fluid-Particle Suspension. *International Journal of Multiphase Flow*, 16(1):35–42, 1990.

[62] T. Hakoshima K. Iwata and R. Nagata. Measurement of Flow Velocity Distribution by Multiple Exposure Speckle Photography. *Optics Communications*, 25(3):311–314, June 1978.

[63] G. H. Kaufmann. On the Numerical Processing of Speckle Photography Fringes. *Optics and Laser Technology*, pages 207–209, August 1980.

[64] G. H. Kaufmann. Numerical Processing of Speckle Photography Data by Fourier Transform. *Applied Optics*, 20(24):4277–4280, December 1981.

[65] Tsuyoshi Hakoshima Koichi Iwata and Ryo Nagata. Measurement of Flow Velocity Distribution by Means of Double Exposure Holographic Interferometry. *Journal of Optical Society of America*, 67(8):1117–1121, August 1977.

[66] S. C. Hill L. D. Smoot and P. J. Smith. NO_x Prediction for Practical Pulverised Coal Reactors. In *Symposium on Stationary Combustion NO_x Control CS-4360*, EPRI, 1985.

[67] M Lance and J. Bataille. Turbulence in the Liquid Phase of a Uniform Bubbly Air-Water Flow. *Journal of Fluid Mechanics*, 222:95–118, 1991.

[68] B. E Launder and D. B. Spalding. *Mathematical Models For Turbulence.* Academic Press, London, 1972.

[69] K. B. Lee and M. K. Chung. Refinement of the Mixing-Length Model for Prediction of Gas-Particle Flow in Pipe. *International Journal of Multiphase Flow*, 13(2):275–282, 1987.

[70] S. Lee. Particle Drag in Dilute Turbulent Two-Phase Suspension Flow. *International Journal of Multiphase Flow*, 13(2):247–256, 1987.

[71] S. Lee and M. A. Wiesler. Theory on Transverse Migration of Particles in a Turbulent Two-Phase Suspension Flow Due to Turbulent Diffusion - I. *International Journal of Multiphase Flow*, 13(1):99–111, 1987.

[72] S. L. Lee. A Unified Theory on Particle Transport in a Turbulent Dilute Two-Phase Suspension Flow - II. *International Journal of Multiphase Flow*, 13(1):137–144, 1987.

[73] J. A. Leendertz. Interferometric Displacement Measurement on Scattering Surfaces utilizing speckle effect. *Journal of Physics E: Scientific Instruments*, 3:214–218, 1970.

[74] C. C. Lin. *Turbulent Flows and Heat Transfer.* Oxford University press, 1959.

[75] L. M. Lorenço and R. Meynart. Guidelines for Choice of the Parameters in a Measurement Using Multiple Exposure Photography. In *Von Karman Lecture Series*, Von Karman Lecture Series, pages 10–46, 1986.

[76] C. A. Greated M. L. Jakobsen, W. J. Hossak and W. J. Easson. PIV Analysis Using an Optically Addressed Spatial Light Modulator. In *Conference of Applied Optics and Opto-Electonics*, Leeds, UK, 1992.

[77] T. J. Hanratty M. M. Lee and R. J. Adrian. The Interpretation of Droplet Deposition Measurement With a Diffusion Model. *International Journal of Multiphase Flow*, 15(3):459–469, 1989.

[78] M. Quintanilla M. P. Arroyo and L. M. Savirón. Three Dimensional Study of Rayleigh-Bénard Convection by Particle Image Velocimetry Measurements. *L.I.A. ICALEO*, 67:187–195, 1988.

[79] H. H. Qui M. Sommerfeld and D. Koubaridis. The Influence of Swirl on the Particle Dispersion. Source uknown.

[80] R. Marinuzzi and A. Pollard. Comparative Study of Turbulence Models in Predicting Turbulent Pipe Flow Part 1: Algebraic Stress and $k - \varepsilon$ models. *AIAA*, 27(1):29–36, 1989.

[81] K. J. Mathews and J. A. Mobsby. NO_x Reduction In Power Station Combustion Systems. In *Symposium on NO_x Generation and Control in Boiler and Furnace Plants*, Southsea, 1988.

[82] M. L. Mathur and N. R. L. Maccullum. Swirling Air Jets Issuing From Vane Swirlers. Part 1: Free Jets. *Journal of Institute of Fuel*, 60:214–225, 1967.

[83] Denise R McCluskey. Study of Roping in Pneumatic Particle Transport with Particular Reference to Coal Fired Boilers. Second year phd report, Edinburgh University, June 1988.

[84] Denise Rebecca McCluskey. *An Optical Investigation of Air-Particle Flows*. PhD thesis, Edinburgh University, 1992.

[85] W. D. McComb and S. M. Salih. Comparison of Some Theoretical Concentration Profiles for Solid Particles in a Turbulent Jet With the Results of Measurements Using Laser-Doppler Anemometer. *Journal of Aerosol Science*, 9:299–313, 1978.

[86] W. D. McComb and S. M. Salih. Measurement of Normalised Radial Concentration Profiles in a Turbulent Aerosol Jet, Using a Laser-Doppler Anemometer. *Journal of Aerosol Science*, 8:171–181, 1978.

[87] Roland Meynart. Equal Velocity Fringes in Rayleigh-Bénard Flow by a Speckle Method. *Applied Optics*, 19(9):1385–1386, September 1980.

[88] Roland Meynart. Digital Image Processing for Speckle Flow Velocimetry. *Rev. Sci. Instrum.*, 53(1):110–111, January 1982.

[89] Roland Meynart. Non-Gaussian Statistics of Speckle Noise of Young's Fringes in Speckle Velocimetry. *Applied Optics*, 24(10):1448–1453, May 1985.

[90] Y. Nagano and M. Tagawa. An Improved k-ε Model for Boundary Layer Flows. *Journal of Fluids Engineering*, 112:33–39, 1990.

[91] G. J. Troup P. L. Barker, F. Ninio and R. Bryant. Velocity Measurement with Speckle and Speckle-like Photographs. Source unknown.

[92] C. J. Park and L. D. Chen. Experimental Investigation of Confined Turbulent Jet: Part II: Particle-Laden Flow Data. *AIAA Journal*, 27(11):1511–1516, 1989.

[93] S. V. Patankar. *Numerical Heat Transfer and Fluid Flow.* Hemisphere Publishing Corp., McGraw-Hill Book Co, 1980.

[94] R. H. Perry and C. H. Chilton. *Chemical Engineering Handbook.* International Student Edition. McGraw-Hill International Book Company, 5^{th} edition, 1974.

[95] Tencer Cebeci Peter Bradshaw and James Whitelaw. *Engineering Calculation Methods for Turbulent Flow.* Academic Press, 1981.

[96] W. H. Peters and W. F. Ranson. Digital Imaging Techniques in Experimental Stress Analysis. *Optical Engineering*, 21(3):427–431, May/June 1982.

[97] W. F. Phillips. The Effect of Froude Number on Entrainment in Two-Dimensional Line Plumes. *Journal of Fluids Engineering*, 103:471–477, 1981.

[98] C. J. D. Pickering and N. A. Halliwell. Particle Image Velocimetry: Fringe Visibility and Pedestal Removal. *Applied Optics*, 24(16):2474–2476, August 1985.

[99] C. J. D. Pickering and N. A. Halliwell. Particle Image Velocimetry: Improving Fringe-to-Noise Ratio with a Two-step Photographic Process. *Journal of Optical Society of America*, 2(4):610–615, April 1985.

[100] C. J. D. Pickering and N. A. Halliwell. Particle Image Velocimetry: Improving Fringe-to-Noise Ratio with a Two-step Photographic Process: Part ii. *Journal of Optical Society of America*, 2(10):1721–1724, October 1985.

[101] Christopher J. D. Pickering and Neil A. Halliwell. Laser Speckle Photography: Preprocessing of Fringe Pattern Data to Improve Dynamic Range. *Journal of Photographic Science*, 33:183–186, 1985.

[102] John Redman. FGD-The Wet Limestone/Gypsum Process. *Chemical Engineering*, (453):29–36, October 1988.

[103] John Redman. Control of NO_x Emissions From Large Combustion Plants. *The Chemical Engineer*, (458):33–39, March 1989.

[104] J. N. Chung Reiyn Chein. Simulation of Particle Dispersion in a Two-Dimensional Mixing Layer. *AIChE Journal*, 34(6):946–954, 1988.

[105] M. A. Rizk and S. E. Elghobashi. A Two-Equation Turbulence Model for Dispersed Dilute Confined Two-Phase Flows. *International Journal of Multiphase Flow*, 15(1):119–133, 1989.

[106] Wolfgang Rodi. *Turbulence Models And Their Application In Hydraulics.* State-of-the-art Paper, 1980.

[107] Thomas L. Saaty. *Modern Nonlinear Equations.* McGraw-Hill Book Company, 1967.

[108] Dr Hermann Schlichting. *Boundary Layer Theory.* London Pergamon Press, 1955.

[109] P. G. Simpkins and T. D. Dudderar. Laser Speckle Measurement of Transient Bénard Convection. *Journal of Applied Mechanics*, 89(4):665–671, 1970.

[110] S. K. Sinha. Improving the Accuracy and Resolution of Particle Image or Laser Speckle Velocimetry. *Experiments in Fluids;*, 6:67–68, 1988.

[111] R. K. Sinnott. *Chemical Engineering*, volume 6 of *Chemical Engineering.* Pergamon Press, 1980.

[112] Karl A. Stetson. The Vulnerability of Speckle Photography to Lens Aberrations. *Journal of Optical Society of America*, 67(11):1587–1590, November 1977.

[113] Dirk J. Struik. *Differential Geometry.* Addison-Wesley Publishing Company, INC., second edition, 1961.

[114] Nobukatsu Takai and Toshimitsu Asakura. Displacement Measurement of Speckle Using a 2-D Level-Crossing Technique. *Applied Optics*, 22(22):3514–3519, November 1983.

[115] N. Takemitsu. An Analytical Study of the Standard k-ε Model. *Transactions of the ASME*, 112:192–198, 1990.

[116] H. J. Tiziani. Application of Speckling for in Plane Vibration Analysis. *Optica Acta*, 18(12):891–902, 1971.

[117] A. A. Townsend. *The Structure Of Turbulent Shear Flow*, chapter 5 to 7. Cambridge University Press, 2nd edition, 1956.

[118] D. J. Tritton. *Physical Fluid Dynamics*. Oxford Science Publications, second edition, 1988.

[119] Y. Tsuji, Y. Morikawa, and H. Shinomi. Ldv Measurement of Air-Solid Two-Phase Flow in a Vertical pipe. *Journal of Fluid Mechanics*, 139:417–434, 1984.

[120] Chandra S. Vikram. Error In Speckle-Photography of Lateral Sinusoidal Vibrations: A Simple Analytical Solution. *Applied Optics*, 21(10):1710–1712, May 1982.

[121] Chandra S. Vikram. Simple Approach to Process Speckle-Photography Data. *Optic Letters*, 7(8):372–273, August 1982.

[122] Chandra S. Vikram and K. Vedam. Complete 3-D Deformation Analysis in the White Light Speckle Method. *Applied Optics*, 22(2):213–214, January 1983.

[123] Klaus D. Hinsch W. Amold and D. Mach. Turbulence Level Measurement by Speckle Velocimetry. *Applied Optics; Volume 25*, 25(3):330–331, February 1986.

[124] Robert C. Weast and Melvin J. Astle (*editor*). *Handbook of Chemistry and Physics*. CRC Press Inc., 62 edition, 1981.

[125] U. Wemekinck and W. Merzkirch. Speckle Photographs of Spatially Extended Refractive-Index Fields. *Applied Optics*, 26(1):31–32, January 1987.

[126] Ichirou Yamagushi. Fringe Formation in Speckle Photography. *Journal of Optical society of America*, 1(1):81–86, January 1984.

[127] Chung-Sheng Yao and Ronald J. Adrian. Orthogonal Compression and 1-D Analysis Technique for Measurement of 2-D Particle Displacement in Pulsed Laser Velocimetry. *Applied Optics*, 23(11):1687–1689, May 1987.

[128] Carlos A. Polmalaza-Raéez Yu-Shan Fong and Xiao-Hua Wang. Comparison Study of Nonlinear Filters in Image Processing Applications. *Optical Engineering*, 28(7):749–760, July 1989.